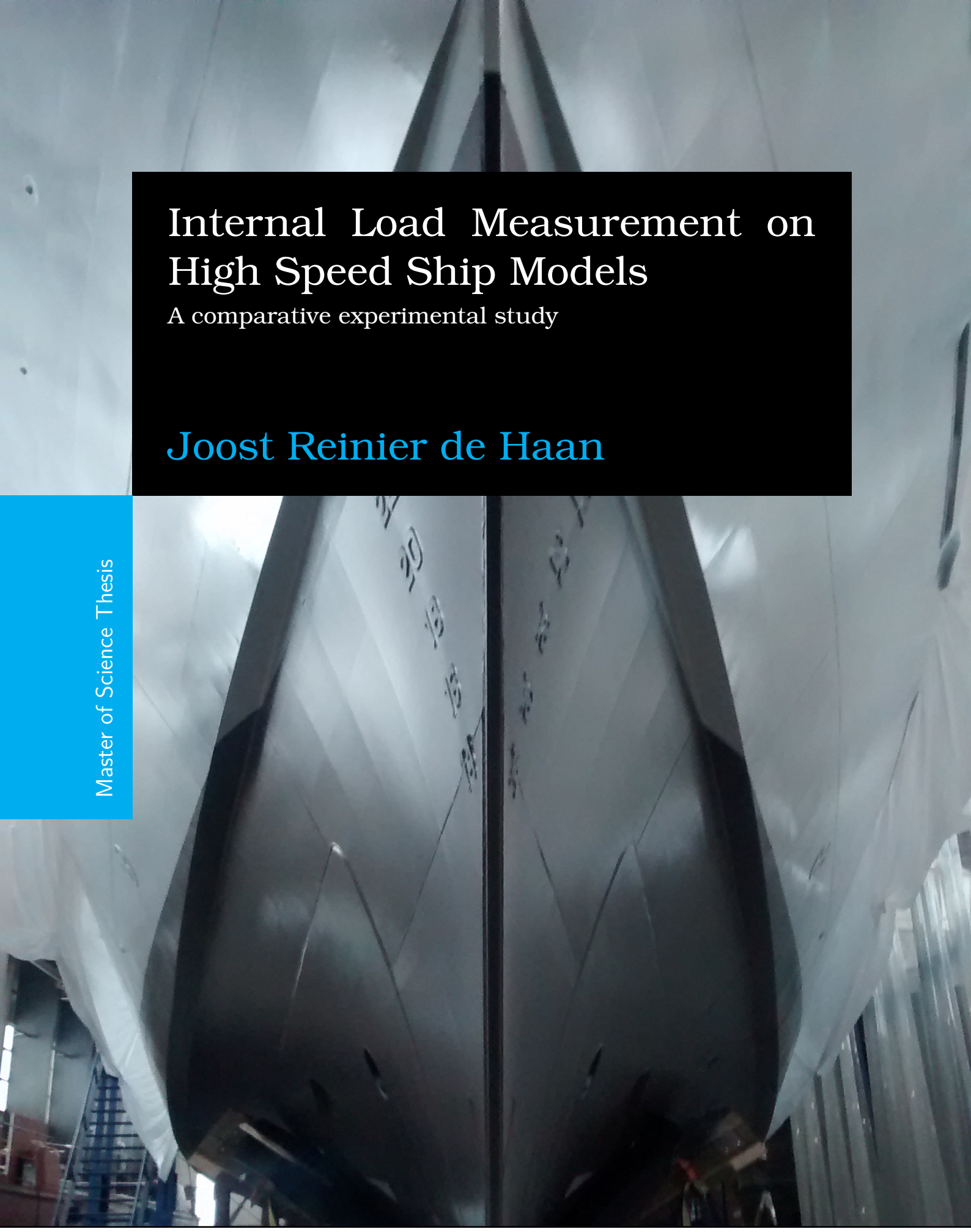

Internal Load Measurement on High Speed Ship Models

A comparative experimental study

Joost Reinier de Haan

Master of Science Thesis

TU Delft Delft University of Technology

Offshore and Dredging Engineering – 3mE

Internal Load Measurement on High Speed Ship Models

A comparative experimental study

Master of Science Thesis

For the degree of Master of Science in Offshore and Dredging Engineering at Delft University of Technology

Joost Reinier de Haan

March 31, 2015

Faculty of Mechanical, Maritime and Materials Engineering (3mE) · Delft University of Technology

The work in this thesis was supported by Damen Shipyards Group, Gorinchem.
Their cooperation is hereby gratefully acknowledged.

Delft University of Technology
Department of
Ship Hydromechanics and Structures (SHS)

The undersigned hereby certify that they have read and recommend to the Faculty of Mechanical, Maritime and Materials Engineering (3mE) for acceptance a thesis entitled

Internal Load Measurement on High Speed Ship Models

by

Joost Reinier de Haan

in partial fulfillment of the requirements for the degree of

Master of Science Offshore and Dredging Engineering

Dated: March 31, 2015

Supervisors:

Prof.dr.ir. R.H.M. Huijsmans

Dr.ir. P. de Jong

Ir. P. de Vos

Abstract

For over a century, model tests have supported in ship and offshore structures design. Experimental results can be used to (1) validate theory to apply numerical simulations in the design and (2) for design by testing, directly using the (scaled) results in the design. Recently, at the Ship Hydromechanics and Structures lab of the TU Delft, a series of experiments was carried out with a 1/20 scale 42 m fast patrol vessel. The model was segmented to enable internal loads measurement. Unfortunately the results were unsatisfactory, in all probability due to errors in the measurement set-up. As a consequence, a new routine of the numerical program FASTHIP could not be validated. The current research goal was to identify flaws of the prior measurement set-up, develop an improved set-up and determine its performance.

First, a broad range of experiments was conducted to gain a deeper understanding of the load path of the previously used set-up. By systematically increasing the disturbance factors, the defects in the set-up could be identified. Due to its versatility and relative easy construction, the two segment rigid backbone construction was used. Two measurement options were developed and implemented, both with the aim to measure the vertical bending moment amidships.

The bending moment was measured:

1. Indirectly using 9 force transducers.
2. Directly using 4 coupled fixed strain gauges.

The set-up was tested before final assembly. This included an extensive calibration of the strain gauges placed directly on the backbone. Hereafter, experiments with increasing complexity were carried out. During calm water tests, the model was towed at a range of forward speeds. The equations forming the indirect method were verified using the measurement data and the free-free beam boundary conditions. To assess the performance in dynamic conditions, the model was towed at three velocities through a frequency range of regular head waves, forming 48 conditions.

The signals were processed using a digital band pass filter and fitted against the excitation frequency. Inertia correction at the indirect method was conducted per time step by using the backbone mass properties and the vertical and rotational accelerations.

The methods were compared regarding the bending moment values and the associated 95 % confidence limits. Both options deliver equal and accurate results in calm water tests. In regular head waves the required processing to obtain the indirectly measured vertical bending moment proved specific and devious. This leaves the direct method the preferred choice for in particular the semi-planing regime velocities.

By increased adaption of the backbone design to the expected excitation forces, the confidence bound limits will turn out more favorable. For this, it is key to incorporate a structural member with limited mass and obtain the required strain levels at the section cuts while maintaining sufficient global stiffness to avoid unwanted resonance. The improved measurement accuracy will further enlarge the practicability of measurement results for direct use in the design and numerical code validation.

Table of Contents

I Introduction and Literature **1**

1 Introduction **3**

1-1 Background . . . 3

1-2 Problem statement . . . 5

1-2-1 Sub-problems of the problem statement . . . 6

1-3 Scope and Outline . . . 7

2 Theoretical Background **9**

2-1 Model types for internal load measurement . . . 10

2-2 Scaling . . . 14

2-3 Load types . . . 18

2-4 Model segmentation . . . 19

2-4-1 2-segment model . . . 20

2-4-2 3-segment model . . . 20

2-4-3 4-segment model . . . 20

2-5 High speed craft implications . . . 20

2-5-1 Planing hull . . . 21

2-5-2 Slamming . . . 21

2-5-3 Fatigue . . . 22

2-5-4 Model weight limitation . . . 23

2-5-5 Neutral axis . . . 23

2-6 Seakeeping (numerical code) theories and application . . . 26

2-6-1 Methods for ship motion and load calculation for ships with forward speed 27

2-6-2 Equations of motion . . . 29

2-6-3 Analytic expressions for internal loads . . . 29

2-7 Concluding . . . 31

II Experiments **33**

3 Measurement set-up development **35**

3-1 Experimental problem identification . . . 35
3-1-1 Vertical load and -moment representation . . . 36
3-1-2 Sensitivity to applied torque and 'parallel' load . . . 37
3-1-3 Horizontal- and combined load . . . 38
3-1-4 To conclude . . . 41
3-2 Objectives - Load cases . . . 41
3-3 Functional requirements . . . 42
3-4 Force measurement concepts . . . 43
3-4-1 Force transducers at the segment-backbone interface . . . 43
3-4-2 Strain gauges mounted to the backbone . . . 44
3-5 Ship mounting . . . 45
3-6 Data acquisition . . . 46

4 Experiment Preparation **49**

4-1 Boundary conditions . . . 49
4-2 Test program . . . 50
4-2-1 Dry testing . . . 51
4-2-2 Calm water . . . 51
4-2-3 Regular head waves . . . 52
4-2-4 Irregular head waves . . . 52
4-3 Force sensors' calibration and validation . . . 53
4-3-1 Calibration process . . . 53
4-3-2 Validation . . . 54
4-4 Auxiliary sensors' calibration . . . 55
4-5 Model mass and inertial properties . . . 56

5 Results **57**

5-1 Calm water . . . 57
5-1-1 Ship model resistance . . . 57
5-1-2 Ship model vertical bending moment . . . 59
5-1-3 VSF and VBM along the backbone . . . 60
5-2 Regular head waves . . . 62
5-2-1 Stationary . . . 62
5-2-2 Forward velocity . . . 65

III Interpretation and conclusions **69**

6 Discussion **71**
6-1 Concept . . . 71
6-2 Calm water experiments . . . 72
6-3 Regular head waves experiments . . . 73
6-3-1 Resonance and other confounding effects . . . 73
6-4 Confidence bounds . . . 75

7 Conclusions **77**

A Experiment results **81**

B Euler-Bernoulli beam theory **85**
B-1 Euler-Bernoulli beam equation . . . 85
B-2 Second moment of area . . . 86
B-3 Modulus of Elasticity . . . 86
B-4 Strain . . . 87
B-5 Loads . . . 87
B-6 Boundary conditions . . . 88
B-7 Solution . . . 88
B-7-1 Displacement . . . 88
B-7-2 Strain . . . 89
B-7-3 Natural frequencies of a free-free beam . . . 90

C Data processing **93**
C-1 Zero runs . . . 93
C-2 Calm water . . . 94
C-3 Regular waves . . . 97
C-3-1 Inertia correction . . . 97

D Uncertainty analysis **99**
D-1 Approach . . . 99
D-2 Bias error . . . 100
D-2-1 Indirectly measured VBM . . . 100
D-2-2 Directly measured VBM . . . 101
D-2-3 Other . . . 102
D-3 Precision error . . . 102
D-3-1 Indirectly measured VBM . . . 103
D-3-2 Directly measured VBM . . . 103
D-4 Total uncertainty limits . . . 103

E Paper Article **105**

Bibliography **115**

Glossary **119**

List of Acronyms 119

List of Symbols 120

Acknowledgements **123**

List of Figures

1-1 Damen Stan Patrol 4207 render 5
1-2 Structure of the thesis. 7

2-1 Hogging and sagging phenomena 9
2-2 Ship model used in Kim (2010) 11
2-3 Load distribution over the length of a planing ship. 13
2-4 Governing excitation forces and ship responses 19
2-5 Slamming types indicated on the Damen Twin Axe Fast Crew Supplier. 22
2-6 HSC advancing in calm water, front segment with hull cut at midship. 24
2-7 Superposition of the bending stress and axial stress results in the absolute stress distribution. 24
2-8 Calm water hydrostatic forces acting on the aft hull segment. 25
2-9 Forces acting on the hull as used in the fastship routine. 29
2-10 Loads on a cross section. 30

3-1 Replicated prior set-up. 36
3-2 Photograph of free hanging part – prior set-up. 36
3-3 Replicated prior set-up – added hinges. 37
3-4 Set-up for testing torque sensibility. 37
3-5 Force transducer's sensibility to torque. 38
3-6 Experimental set-up – schematic side view. 39
3-7 Leaking F_h as function of applied vertical and horizontal loads. 40
3-8 Experimental set-up concept – side view. 43
3-9 Vishay general purpose strain gauge. 45

5-1 Model resistance: regular and rough hull. 58
5-2 Model added VBM: regular and rough hull. 59

5-3 Regular and rough hull VBM values inc. confidence bounds. 60
5-4 VSF along the backbone length. 61
5-5 VBM along the backbone length. 61
5-6 Vertical force amplitudes and VBM RAOs, constrained model. 63
5-7 RAOs for heave and pitch, $V_m = 0$ m/s. 64
5-8 Added VBM, $V_m = 0$ m/s, $\kappa = 1/60$. 65
5-9 Response Amplitude Operators (RAOs) for heave and pitch, $V_m = 3$ and 4.5 m/s. 66
5-10 RAOs added VBM, $V_m = 3.0$ m/s, $\kappa = 1/60$. 67
5-11 Added VBM timetrace at two wave frequencies, $V_m = 3.0$ m/s. 68

6-1 (In)direct VBM and acceleration timetrace, $V_m = 4.5$ m/s, $\omega_m = 5.81$ rad/s. . . 74

A-1 RAOs and direct VBM values, $V_m = 0.0$ m/s, $\kappa = 1/60$. 81
A-2 RAOs and direct VBM values, $V_m = 3.0$ m/s, $\kappa = 1/30$. 82
A-3 RAOs and direct VBM values, $V_m = 4.5$ m/s, $\kappa = 1/60$. 83

B-1 Conditions for analytic strain calculation. 88

C-1 Acting forces during zero run. 94
C-2 Backbone free body diagram. 95

List of Tables

2-1 Past studies on internal load measurement on ship models. 12
2-2 ITTC Recommended Procedures and Guidelines. 13
2-3 Agreement with continuous beam numerical model for segmented models. 21

3-1 Load conditions during the experiment. 40
3-2 Sensors and input signals. 48

4-1 Rounded calm water velocities. 51
4-2 Regular head waves parameters. 52
4-3 Irregular wave parameters. 53
4-4 Calibration values of force and moment sensors. 54
4-5 Minimum, maximum and average measurement deviations. 55
4-6 Model mass and inertial properties. 56

5-1 Absolute and relative force and moment discrepancies. 62

B-1 Numerical solutions to $cosh(kL) \cdot cos(kL) = 1$. 91

C-1 Model mass and inertial properties. 94

D-1 Indirectly measured VBM calibration parameters. 101
D-2 Directly measured VBM calibration parameters. 102
D-3 Bias limits 102

Part I

Introduction and Literature

Chapter 1

Introduction

It may be in people's nature to find the internals of any object more interesting than its externals, no matter how beautiful the object is at first sight. Whether it concerns a young child who cannot wait to unwrap its birthday or Christmas present, or a car-enthusiast that is dying to take place in the drivers seat of his favorite car, the internals are particularly appealing. Similarly, the aspiration to know what is happening inside a model ship is the motive for this thesis and research topic. Numerous studies have been conducted on seakeeping behavior for a variety of offshore structures and ships. The studies are either analytic, numerical, experimental or a combination thereof. Acquired knowledge had led to designs optimized to enhance operational safety and sailing comfort. Future design optimization is expected in the structural internals more than in hydromechanical response. An important requirement for the structural design is knowledge of the internal loads. The current study's emphasis is on conducting sound, accurate and reliable experimental research of scale model high speed ships to acquire the internal loads. The results can ultimately lead to material and cost savings for the world's shipbuilders.

1-1 Background

Initiated by William Froude, ship model tests support in ship design for over 150 years [1]. When proper scaling is applied, the results of small-scale tests can be used to predict the behavior of full-sized ships. Historically, a substantial amount of model testing is conducted in a towing tank; i.e. a water basin, typically several meters wide and several hundred meters long. A carriage tows the model along the length of the basin to simulate an advancing ship. Simultaneously, a set of measurement data (e.g. motions, forces) is being recorded. Before computers became widely available, model tests were the single option to obtain both quantitative and qualitative results. Developments of electronics and likewise in numerical simulation ended this monopoly (to a certain degree) by the 1970's [2], nevertheless it is not expected that model testing will discontinue in the foreseeable future. Today, model tank tests still are a valuable and essential tool for design of structures that interact with a fluid (water

as main medium). Besides ship design, tests are typically performed for offshore structures which include semi-submersibles, tension leg platforms or smaller elements e.g. propellers and risers. The results may be used in two ways: (1) to validate theory and apply numerical simulations in the design of structures or (2) for design by testing; the experimental results are scaled and used directly in the design.

The experiments are performed all around the world. In The Netherlands, the largest facility is located in Wageningen at the Maritime Research Institute Netherlands (MARIN). Furthermore, at the Delft University of Technology (in short TU Delft) two towing tanks are available predominantly for research purposes. At present, the experiments are mostly used to validate numerical code. Examples are: validation of simulating unconventional hull forms, - operations or extreme sea states.

FASTSHIP is an example of numerical simulation software. Developed at TU Delft, the program calculates the ship's motion response using strip theory. As the name indicates, the program is specially developed for calculations of crafts operating at high speeds. More specific: mono-hull crafts operating at (volumetric) Froude numbers between 1.5 and 3.0. Today's High Speed Craft (HSC) hull and superstructure are often constructed from aluminium. The material's strength-to-weight ratio makes it a beneficial material of choice for this type of vessels. A disadvantage of aluminium is its reduced resistance to fatigue. Compared to steel, it is more sensitive to fatigue crack growth. The use of aluminium demands for more knowledge of the ship's internal loads, especially the vertical bending moment. No closed form analytic solution is available for solving the internal loads of such complex structures. A numerical approach should be applied to solve this problem. In 2010, a routine was added to FASTSHIP to calculate the load distribution and resulting shear and bending moment along the length of the ship [3].

At the Ship Hydromechanics and Structures (SHS) section of the 3mE faculty of the TU Delft, a study aimed to validate the routine was conducted. The validation was carried out using a carbon fiber model of the Damen Stan Patrol 4207 vessel, which was downscaled by a factor 20. The Stan Patrol operates in coastal waters and offshore. It is primarily used for military duties (e.g. operated by coastguards), but built to commercial specifications and standards. Please refer to Figure 1-1 for an impression of the ship. For the study, the scale model was cut at midship and the two segments were connected via a carbon fiber backbone. The natural frequencies of the backbone are significantly higher than the excitation frequency of the occurring sea spectra. As a result this backbone configuration is considered as a rigid body. Force transducers were placed at the interface of the backbone and the two segments.

The model experiments were conducted in Towing tank 1 at the SHS laboratory. The model was towed at different velocities in calm water, and water with regular - and irregular waves. The model was free in heave and pitch, all other degrees of freedom are fixed with respect to the towing carriage. By using a total of 7 force transducers, the vertical bending moment at midship was calculated and evaluated. The measured forces showed values that conflict with Newton's first law and were considered not usable for validation of the FASTSHIP routine. The next section explains this more detailed.

Figure 1-1: Damen Stan Patrol 4207 render

1-2 Problem statement

From the model experiments, no validation could be conducted. The results demand a review of the set-up and experimental procedures. The measured and simulated motions as well as the measured forces and resulting bending moment showed a significant discrepancy. Although the motions during calm water tests were in good agreement after tuning the added mass and buoyancy coefficients in FASTSHIP, response in (ir)regular waves did not match the measured values during model tests. By adding a correction factor for damping in the numerical code, the discrepancy is expected to practically diminish. Moreover, modification of the routine is not in the scope of work for this research. In this study, the focus is on investigation of the differences in measured and calculated forces and moments of the segmented scale model ship.

The main observations during the analysis of the measured forces are listed below.

- The sum of horizontal forces[1] was non-zero for stationary, (quasi) static equilibria.
- Calculation of the midship bending moment was conducted in two ways, providing different results.
- Both results were significantly different from the results obtained from the simulations.
- The contribution of the horizontal (i.e. resistance) component to the bending moment was extensive.

The measured results showed physically impossible shear values at the backbone boundaries. The ship (and backbone as its structural member) can be considered as a free-free beam. The boundary conditions for this type of structural element state that the shear force and bending moment at the ends should be zero at all times. The cause of the non-zero measured

[1] primarily consisting of one transducer at each segment and one transducer at the towing arm.

values is disputed, but expected to be found in errors of the measurement set-up. The fact that the sum of measured horizontal forces is not equal to zero, reinforces the hypothesis of errors being present in the set-up. Briefly and generalized:

> **The earlier used set-up for internal load measurement on a high speed ship model is unable to provide results suitable to predict full scale values or validate numerical code.**

The prior research's goal was to validate the FASTSHIP numerical routine using the Damen Stan Patrol model. Since this goal is still present, the model will be continued to be used. The full scale ship's aluminium hull increases the relevance of predicting the internal forces and moments. As the thesis title states; the research is focused on internal load measurement on high speed ship models, however it is not necessarily limited to high speed conditions.

1-2-1 Sub-problems of the problem statement

A number of sub-problems directly relate to the problem statement and cover topics as part of the research. As a start, a literature study in the field of internal load measurement is conducted. Special attention is payed to physical phenomena that apply in particular for crafts operating at high speeds. It is known that at planing velocities, multiple nonlinear effects start to affect the ships motions and internal loads. These effects must be taken into account regarding the the set-up design and data processing. Moreover, whilst it was known that the measurements results showed illogical values, it was claimed that the ship resistance contributed significantly to the midship vertical bending moment. This allegation can raise doubts for multiple reasons and therefore further theoretical and experimental research effort is put into this sub-topic.

Please find the more complete list briefly described below:

- Analyze methods that are used for internal load measurements at model scale and compare the methods to the earlier used rigid backbone representation.
  - What physical aspects differentiate experiments at (semi) planing velocities from lower velocity experiments?
- Investigate the type of loads present during operation/experimentation.
  - Governing loads per operation condition.
  - Load characteristics of the relevant loads.
- Systematically investigate possible errors in the prior used set-up.
- Design and evaluate the new set-up to confirm reliability.
  - Mathematically formulate and process physical consequences of the measurement set-up, e.g. inertial properties.
  - Identify nonlinearities in the motion- and force response, incorporate in the processing where possible.
- Investigate the possible influence of the resistance component on the vertical bending moment.
- Evaluate the performance and reliability of the measurement set-up.

1-3 Scope and Outline

Starting off with the top level distinction: thesis is divided into three parts. In the first part, the theoretical basis for conducting experiments aimed to measure internal loads is outlined in two chapters. The second part continues using this basis by explaining the theoretical and operational preparation and experiment execution. In the third part, an interpretation of the earlier presented results is given and conclusions are drawn. Below, the three parts are outlined in more detail.

The current chapter, chapter 1 started with an analogy and first 'encounter' with internal load measurement. The chapter continued with providing background information and the principal reasons to this research, summarized by the problem statement. The last, current, section explains the main structure and topics that are discussed per chapter.
Chapter 2 provides the theoretical basis for conducting scale model experiments. After evaluating earlier research at internal load measurement, several relevant topics are discussed. These topics include scaling laws, load types during seakeeping (tests), model segmentation and implications for HSC design. The chapter closes with an overview of numerical code theories and their application.

Using the theoretical background, chapter 3 elucidates the process of experimental set-up design. The chapter starts with experimental problem identification which is no typical step in design. However since errors were present in the past, this step is essential for successfully implementing improvements in the set-up. The chapter continues with explaining the objectives of the experiments, the requirements for achieving the objectives and then discusses the aspects that are key for a success set-up. Although model hull production is also key, this is a briefly discussed aspect.
Chapter 4 outlines required preparatory steps. These steps include setting up a test program and, defining key model properties and closes with outlining the calibration of sensors and verification of the assembled set-up.
Data of calm water and regular head waves experiments is processed. The data is presented in chapter 5, supported by an appendix explaining the process steps.

The results' interpretation is discussed in chapter 6. The final chapter outlines a number of conclusions and provides recommendations for further research and future experiments.

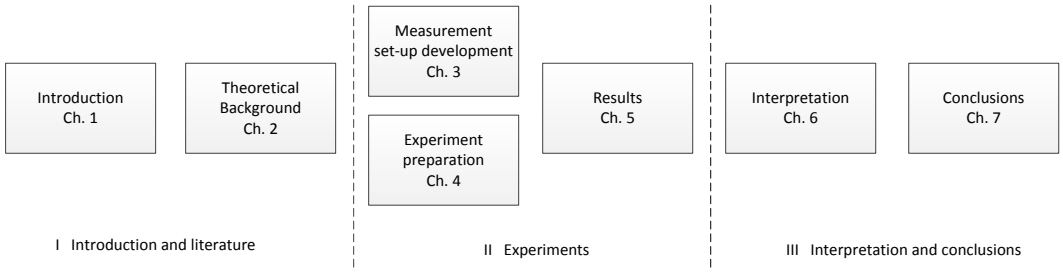

Figure 1-2: Structure of the thesis.

Chapter 2

Theoretical Background

Model experiments are inextricably linked to ship design since the second half of the 19th century. Early tests led to the development of scaling rules that cleared the way to predict the behavior of full-sized ships by using scale models. The initial goal of towing rigid scale models was to obtain the hull resistance, assisting in optimizing the design for minimum resistance and fuel consumption. Later, by applying artificial wave making equipment, motions of ships or offshore structures in various ocean conditions could be determined. From these tests, the safety and operational limits of the structure can be determined and optimized.

With increasing ship sizes, there was an increasing demand for acquiring internal reaction forces and moments. In calm water, the governing factor for the Vertical Shear Force (VSF) and Vertical Bending Moment (VBM) is the local inequality of buoyancy and mass. A ship with excess buoyancy at midship causes a negative, or *hogging* VBM. Refer to figure 2-1a. This corresponds with tensile stress at the deck and compressive stress at the keel. At the opposite conditions a positive, or *sagging* VBM is present (Fig. 2-1b). Wave excitation can intensify or attenuate this effect depending on wave amplitude(s), -number(s) and -phase(s). Please note that the M states the bending moment that is present at midship. At the stern and aft no moment is present.

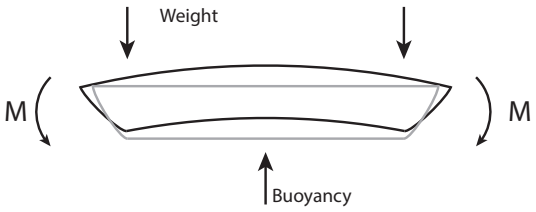

(a) Hogging due to an excess of buoyancy at midship / excess of weight at the stern and aft.

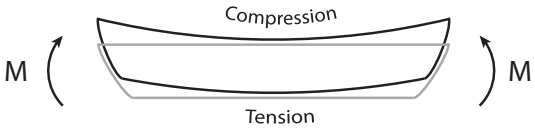

(b) Sagging, leading to compression at deck level / tension at the ships keel.

Figure 2-1: Hogging and sagging phenomena

The current chapter discusses three principal theoretical aspects. The first four sections discuss subjects that must be considered when one conducts model experiments aimed to

measure internal loads. The subjects include model types used in former experiments. Certain model types are scaled to deliver representative structural response, the theory behind this scaling is briefly discussed in Section 2-2. Subsequently, the conditions at which a ship model can be considered rigid are explained. At Section 2-3 the governing load types are stated. Section 2-4 discusses the required number of segments depending on the required type of results. The sensitivity to a change in mass distribution is outlined as well.

The second part's purpose is twofold, i.e. serving as general background for operating conditions and design considerations of full size high speed crafts and secondly outlining design considerations for scale model versions of this type of ship. Topics that are discussed are for instance planing, slamming and fatigue at aluminium ships.

The chapter closes with an overview of seakeeping physics theories and derived numerical codes for internal load calculation. The analytic expressions are also stated. Since future targets include validating numerical code name named FASTSHIP using measurement data of the experiments of the current study, one sub-section outlines the output data of this routine. First, regularly used techniques for internal load measurement on segmented ship models are outlined.

2-1 Model types for internal load measurement

Conventional rigid body models are not able to produce results for determining internal loads. Literature indicates four main options for internal loads measurement at scale model ships. To wit:

1. Model with scaled elasticity (hull).
2. Model with scaled elasticity (backbone) connecting multiple rigid segments.
3. Model with rigid backbone representation connecting multiple rigid segments.
4. Model with force transducer(s) connecting the bulkheads.

One must realize that in fact the term rigid only applies theoretically. For scale model tests, rigid indicates a significantly higher scaled stiffness than structural similarity would require. This aspect is discussed further at the end of Section 2-2. All four numbered options are suitable to produce realistic motion responses of the model. If flexibility and dynamics of the hull structure are important, a flexible model is required. In addition to scaling geometry and mass (including moments of inertia), the model flexibility should be scaled to deliver satisfying results. This can be achieved either by modeling the ship as a fully flexible hull or connecting rigid sections via a flexible connection. A substantial number of recent experimental set-ups use a flexible backbone to measure global structural response. Table 2-1 shows a selection of studies that have been conducted over the last decades. The selection's emphasis is on the rigid representation.

A fully elastic model is the sole option that can deliver structural response at an arbitrary hull location. At the fully elastic concept, the load is directly measured via strain gauges that are glued on the model. As a result, from experiments the bending moments, shearing

forces and torques at any cross section can be obtained. The same applies for stresses at the local hot spots and slamming effects at the bottom or bow flare. Downsides of the method are relatively difficult manufacturing and instrumentation of the model. Wu *et al.* (2003) [4] describes the appropriate technique for design and production. A prime example of a study using a fully elastic model is conducted by Du *et al.* (2004) [5].

The flexible connection can be achieved by a flexible beam connecting the sections, e.g. by Okland *et al.* (2003) [6] or by applying springs between stiff sections (hinged model). The required minimal amount of segments is dependent on the desired results. For global bending moments and shear forces a 2 segment model is sufficient, however for example a 4-segment model is required for correct measurement of accelerations. Section 2-4 addresses segmentation considerations more in depth.

Rigid segmented models with a stiff interior beam are adequate for direct measurements of response to external forces at the hull cuts. This is either achieved by strain gauges at the interface of backbone and segment (Rousset (2010) [7]) or by transducers inserted in between the hull cuts. E.g. Fonseca (2004) [8][9]. The segments operate as a pressure pickup point, therefore automatically producing the surface integrated pressures. The interaction[1] between water (and to a minor extend air) and the structure's deformation is negligible at the rigid backbone representation.

As mentioned earlier, a fourth option is to connect the segments directly via force the measurement equipment. Clauss conducted several studies (including [10]) using a segmented FPSO which was connected through force transducers. The transducers consisted of small metallic beams with fixed strain gauges. Furthermore, Kim *et al.* (2010) [11] conducted a study using a scale model large container carrier. The four segments were connected via three 6 – Degrees of Freedom (DOF) load cells and the results were compared with a set-up using flexible-backbone connected segments. The results showed that the set-up using load cells, the nonlinear wave loads were successfully measured even for extreme wave conditions. The VBM in design waves showed very good agreement with numerical results. The set-up using the backbone system showed successful measurement of springing loads in regular and irregular waves.

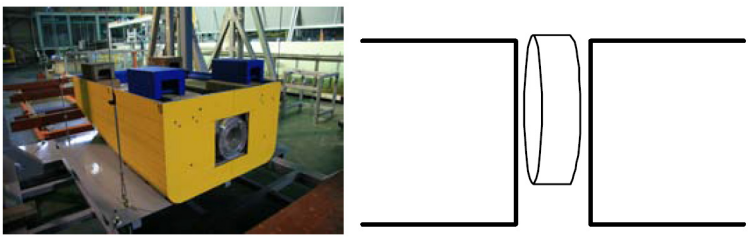

Figure 2-2: Ship model used in Kim (2010) [11].

In addition to the prior studies as listed in Table 2-1, considerations in this thesis were taken with help of International Towing Tank Conference (ITTC) published documents. The documents provide recommended procedures and guidelines for towing tank experiments. Please refer to Table 2-2 for an overview of the most relevant documents.

[1] In literature this effect is referred to as hydro-elasticity. The influence of the structure's deformation on the hydrodynamic pressure is negligible for scale models. When speaking of the interacting loads during scale model experiments, the term hydro-structural load is in fact more correct.

Table 2-1: Past studies on internal load measurement on ship models.

Date	Author(s)	Ship type	Model type	No. of segments	Scope
1991	Gerritsma [12]	Cylinder, series sixty	rigid backbone	7	forced oscillation
2001	Dudson, Rambech, Wu [13]	287 m high speed pentamaran containership	force transducer between bulkheads	4	global load determination
2003	Okland *et al.*[6]	90 m catamaran	flexible backbone	2,3,4	whipping responses
2003	Schellin *et al.* [14]	122 m fast monohull, 110 m high-speed ferry	flexible backbone	4	VSF, VBM for numerical code validation
2005-2013	Dessi *et al.* [15][16][17][18]	128 mm fast ferry	flexible backbone	6	VSF, VBM Output-only analysis technique, slamming on HSCs
2004	Du *et al.* [5]	S-175 container ship	fully flexible hull	1	wavelet analysis of loads
2004	Fonseca, Guedes [8][9]	176 m container ship	rigid backbone	3	VBM, motions also in severe conditions
2004	Marón, Fonseca, Guedes [19][20]	122 m fast monohull	flexible backbone	4	free moving, forced oscillation, hydrodynamic coefficients
2004-2009	Clauss *et al.* [21][22][10][23][24]	280 m FPSO	force transducer between bulkheads	3	VBM, longitudinal forces, extreme seas
2005	Wu, Moan [25]	270 m container ship	force transducer between bulkheads	4	Hybrid method to calculate wave-induced vertical loads
2010	Rousset, Ferrant, Alessandrini [7]	Large cruise vessel	rigid backbone	4	irregular uni/bi-directional waves without forward speed
2010	Kim, Yu, Hong [11]	337 m 6500 TEU class containership	force transducer between bulkheads & flexible backbone	4	nonlinear wave loads, springing loads
2011	Begovic [26]	5414 destroyer frigate	force transducer between bulkheads	2	intact and damaged ship experiments
2011	Zhu, Wu, Moan [27][28]	290 m containership	flexible backbone	17	natural frequencies of VBM, HBM, TM, oblique seas

Table 2-2: ITTC Recommended Procedures and Guidelines. Acquired via: http://ittc.sname.org.

Section	Effective date	Name	Relevant content
7.5-02-01-01	2014	Guide to the Expression of Uncertainty in Experimental Hydrodynamics	Uncertainty analysis of experimental data.
7.5-02-05-04	1999	Seakeeping Tests (specific for HSC)	Towing a planing HSC, measurement parameters etc.
7.5-02-05-06	1999	Testing and Extrapolation Methods High Speed Marine Vehicles Structural Loads	Global load measurement model types.
7.5-02-07-02.1	2011	Seakeeping Experiments	Nat. frequencies, guidance system, wavelength/-height.
7.5-02-07-02.6	2011	Global Loads Seakeeping Procedure	Weight and inertial properties, segmentation.
7.5-02-07-02.x	Concept	Verification of Hydroelastic Seakeeping Computer Codes	Verification tasks of numerical code.

The studies forming Table 2-1 differ from the current study in two principal senses. To start, the studies were conducted using models of ships that were longer by a factor 2-8 compared to the 42 m Stan Patrol. Second, following from the different length to velocity ratio, most studies' experiments were carried out in relatively low Froude numbers. At the Stan Patrol's operation velocities, the ship propagates in a semi-planing regime.

In the semi planing velocity range lift effects form a large part of the total of hydrodynamic forces that act on the ship's hull. Figure 2-3 shows an arbitrary load distribution over the length of a planing monohull ship.

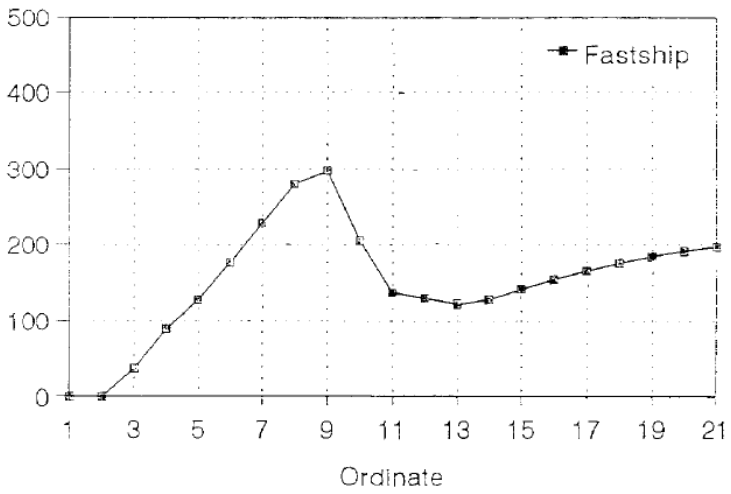

Figure 2-3: Load distribution over the length of a planing ship. From Keuning (1994) [29].

A pressure peak at $\pm$ 1/3 of the water line length is clearly visible. At higher velocities the peak's absolute and relative amplitude and steepness tend to increase. A consequence of the steep peak is a nonlinear increase of the VBM for planing velocities. Naturally, this phenomenon also present at model experiments.

For a more elaborate explanation of the implications of a High Speed Craft (HSC) on full- and model scale, please refer to Section 2-5.

2-2 Scaling

The experiments mentioned above are carried out after applying proper scaling. This is essential to provide usable results. In this section, the most relevant scaling laws are discussed, highlighting the Froude number and scaling of hull flexibility.

Geometric similarity

Geometric similarity requires that the model and the full scale structure must have the same shape. All linear dimensions must have the scale ratio. The geometric scaling factor is by definition:

$$\Lambda_L = L_s/L_m \tag{2-1}$$

Here the subscripts s and m represent the full size and model structures respectively. L is any geometric dimension. For the Stan Patrol ship used in the current study, $\Lambda_L = 20$. In practice, the geometric similarity is not present for the entire vessel. As a minimum, the structural parts that interact with water (wetted surface) are geometrically scaled. Scaling also applies to environmental factors; wave dimensions (wavelength λ and wave amplitude a) being the most dominant. Additionally, when structural response is considered at the model, elastic deformations of the model and ship must agree. Following from (2-1) the water displacement $\nabla = L^3$ must be equally scaled. Symbolically:

$$\Lambda_L^3 = \frac{\nabla_s}{\nabla_m} = \frac{(\mu \cdot L)_s}{(\mu \cdot L)_m} \tag{2-2}$$

Here μ represents the mass per unit length of the ship.

Additional note: A Froude scaling's effect for the towing tank experiments is the introduction of a second scale factor since the fluid density of fresh water differs from the sea water's density (approx. 1026 versus 998 kg/m^3 for 20 $^\circ C$ fresh water). This factor is denoted as Λ_ρ. The model mass should be scaled in compliance with the difference in fluid density. In symbols:

$$M_m = \rho_{freshwater} \cdot \nabla_m = M_s/(\Lambda_L^3 \cdot \Lambda_\rho) \tag{2-3}$$

Hydrodynamic similarity

Dynamic similarity implies that accelerations are equal to the full size vessel's accelerations. With an equal displacement the mass is correctly scaled, however also the moments of inertia must be the same to ensure reliable rigid body motions. Regarding hydrodynamic interaction of a ship (i.e. modeled by a free-free beam), the inertial- and gravitational forces are governing.

Inertial forces:

$$F_i \propto \rho \frac{dU}{dt} L^3 = \rho \frac{dU}{dx} \frac{dx}{dt} L^3 \propto \rho U^2 L^2 \tag{2-4}$$

- ρ is fluid density $[kg/m^3]$
- U is the characteristic velocity $[m/s]$
- t is time $[s]$
- L is the characteristic length $[m]$

Gravitational forces are equally calculated, only using g as the gravitational acceleration.

$$F_g \propto \rho g L^3 \tag{2-5}$$

The Froude number is composed from the ratio between inertia and gravity.
From Eq. (2-4) and (2-5):

$$\frac{F_i}{F_g} \propto \frac{\rho U^2 L^2}{\rho g L^3} = \frac{U^2}{gL} \tag{2-6}$$

With constant Froude number, the gravity forces are correctly scaled. Surface water waves are gravity driven; therefore with equal Fn, correctly scaled wave resistance is ensured.

$$Fn_L = \frac{U_s}{\sqrt{gL_s}} = \frac{U_m}{\sqrt{gL_m}} \tag{2-7}$$

For planing or semi-planing vessels, the Froude number is generally calculated using the cube root of the displacement as a substitute for the length. The physical meaning is debatable, however since the hulls have a highly varying waterline at (semi)planing speeds, the displacement is used. The cube root makes the number dimensionless.

$$Fn_\nabla = \frac{U}{\sqrt{g \cdot \nabla^{1/3}}} \tag{2-8}$$

The Reynolds number indicates the relation between inertia and viscous forces.

$$\frac{F_i}{F_v} \propto \frac{\rho U L}{\mu} = \frac{UL}{\upsilon} = Re \tag{2-9}$$

- υ is the kinematic viscosity, $\upsilon = \frac{\mu}{\rho}$ $[m^2/s]$

- μ is the dynamic viscosity $[Pa \cdot s]$

Equality in Reynolds number will ensure that the viscous forces are correctly scaled. When comparing the Reynolds and Froude numbers, one notices that scaling causes a conflict. For Re, the velocity scale should be proportional to the inverse of the length scale while for Fn, the velocity should be proportional to the square root of the length scale. This is only valid for the full scale 'model'. Gravity forces are the predominant forces at towing tests experiments, and therefore Froude scaling is usually applied. An exemption to this is for example with experiments involving fully submerged submarines. Here viscous forces are dominant over gravity forces.

As a complement to the note on viscous forces, at model scale experiments the following forces are not taken into consideration:

- Elastic fluid forces (the fluid is considered incompressible).
- Surface forces (the typical geometric scaling factor results in negligible surface tension forces).

Structural similarity

When structural response results are required, Froude scaling requires equal ratios of the natural frequencies and the frequency of wave encounter. When considering the hull geometry as a Euler-Bernoulli beam with bending stiffness EI; the 2-noded natural frequency of a vertical hull vibration can be considered proportional to the factor $\sqrt{EI/\mu L^4}$ [30]. (Or equivalently $\sqrt{EI/\nabla L^3}$ as indicated in ITTC Guideline 7.5-02-07-02.6 [31]).
Scaling laws state that time is scaled by a factor $\sqrt{\Lambda_L}$ and (thus) frequency (= time^{-1}) by a factor ${\Lambda_L}^2$.

$$\Lambda_L = {\Lambda_\omega}^2 \tag{2-10}$$

Substituting $\sqrt{EI/\mu L^4}$ from [30] in (2-10) results in:

$$\Lambda_L = \frac{(EI/\mu L^4)_s}{(EI/\mu L^4)_m} \tag{2-11}$$

Rearranging:

$$\frac{(EI)_m}{(EI)_s} = \frac{L_s \cdot (\mu \cdot L \cdot L^3)_m}{L_m \cdot (\mu \cdot L \cdot L^3)_s} \tag{2-12}$$

Replacing μL using (2-2) one obtains:

$$\frac{(EI)_m}{(EI)_s} = \frac{L_m^5}{L_s^5} = \frac{1}{\Lambda_L^5} \tag{2-13}$$

Compared to using a geometrically similar construction, and a material with an equal elastic modulus:

$$\frac{(EI)_m}{(EI)_s} = \frac{I_m}{I_s} = \frac{1}{\Lambda_L^4} \tag{2-14}$$

From comparing Eq. (2-13) and (2-14) it can be concluded that when the same (internal and external) geometry and material is used, the scaled bending stiffness is a factor Λ_L too high. This fact is advantageous for building a model that one would like to behave as a rigid body.

The results during experiments should be scaled according to the following ratios:

Shear force	${\Lambda_L}^3$
Bending moment	${\Lambda_L}^4$
Accelerations	1.0

Model rigidity

One has to realize that models with scaled flexibility show results for that particular flexibility. When the internal structural design is altered, the bending stiffness of the model must change to study the effect of this change. In the design stage, a rigid model is advantageous due to increased employability. Change of structural stiffness does not lead to the requirement to change the model structure. In case of a rigid model, the true girder loading is measured in stead of the result of this loading: strain at the hull or flexible backbone. To consider the model as a rigid body, the natural frequencies of the model must be higher than the wave encounter frequencies.

Wave encounter frequency

From selecting the scaling factor Λ_L, the model scale wavelength and amplitude can be determined. The wave frequency ω at an arbitrary water depth d can be determined from the wavelength λ using the dispersion relationship as explained in [32].

$$\omega^2 = gk \cdot tanh(kd) \; or \; \lambda = \frac{gT^2}{2\pi} \cdot tanh(\frac{2\pi d}{\lambda}) \tag{2-15}$$

For deep water ($tanh(kd) \to 1$ for $kd \to \infty$) the equation simplifies to

$$\omega_0 = \sqrt{gk_0} \; or \; \lambda_0 = gT^2/(2\pi) \tag{2-16}$$

with k_0 the deep water wave number, proportional to $2\pi/\lambda_0$. Deep water waves are commonly considered from $d \geq 0.5\lambda$.

Example

For the Stan Patrol model, $\Lambda_L = 20$. Consider full scale wavelengths of 15–100 m. Scaled wavelengths are 0.7–5.0 m. With the towing tank water depth being 2.3 m, deep water wave theory cannot be applied. From (2-15) for this example the frequency range results in $0.55 - 1.5 \; Hz$ ($\omega = 3.5 - 9.4 \; rad/s$)

The wave encounter frequency ω_e can be calculated from the ships velocity V, the angle of encounter α, the wave frequency and the wave number k.

$$\omega_e = \omega - k \cdot V cos(\alpha) \tag{2-17}$$

With head waves ($\alpha = 180\,^\circ$) the cosine term equals -1. With $Fn_\nabla = 3.0$, $V = 5.0 m/s$. Then $\omega_e \approx 10 - 54\ rad/s$ or $1.6 - 8.6\ Hz$.

Requirement for rigidity

To consider the segmented ship as a rigid body, the structural natural frequencies must be far higher, an order of magnitude higher than the frequency of interest. Frequency of interest for encountering regular waves is discussed above, making the minimum first natural frequency 86 Hz. In practice, this factor is more in the order of 6-8 times higher than the frequency of interest. The requirement is not only applicable to the backbone, but to the natural frequency of the segments, the connection to the backbone and the connection to the towing carriage.

2-3 Load types

A wide range of load types contributes to the generated internal loads of the full scale and model scale ships. Please refer to Figure 2-4 for an overview of the governing excitation forces and the resulting motions and structural response. As explained in the Chapter's introduction hydrostatic pressure is always present for a floating ship. Local inequality in buoyancy and mass causes vertical shear forces and a vertical bending moment. When the ship advances, the addition of dynamic pressure causes a difference in sinkage and trim.

When waves are present, wave frequent loads introduce a motion and structural response of the hull. In open seas, a typical frequency range of waves is from $0.05 - 0.25\ Hz$. Please mind that the excitation frequency increases with a ship advancing in waves as discussed in 2-2.

A third governing phenomenon for ships advancing in waves is named slamming. Slamming can cause a dynamic transient load on the hull, named whipping. In Section 2-5 special attention is payed to this event. Since slamming plays an important role when considering the load type spectrum especially for HSCs, in numerical models the hydrodynamic loads must be considered in the time domain.

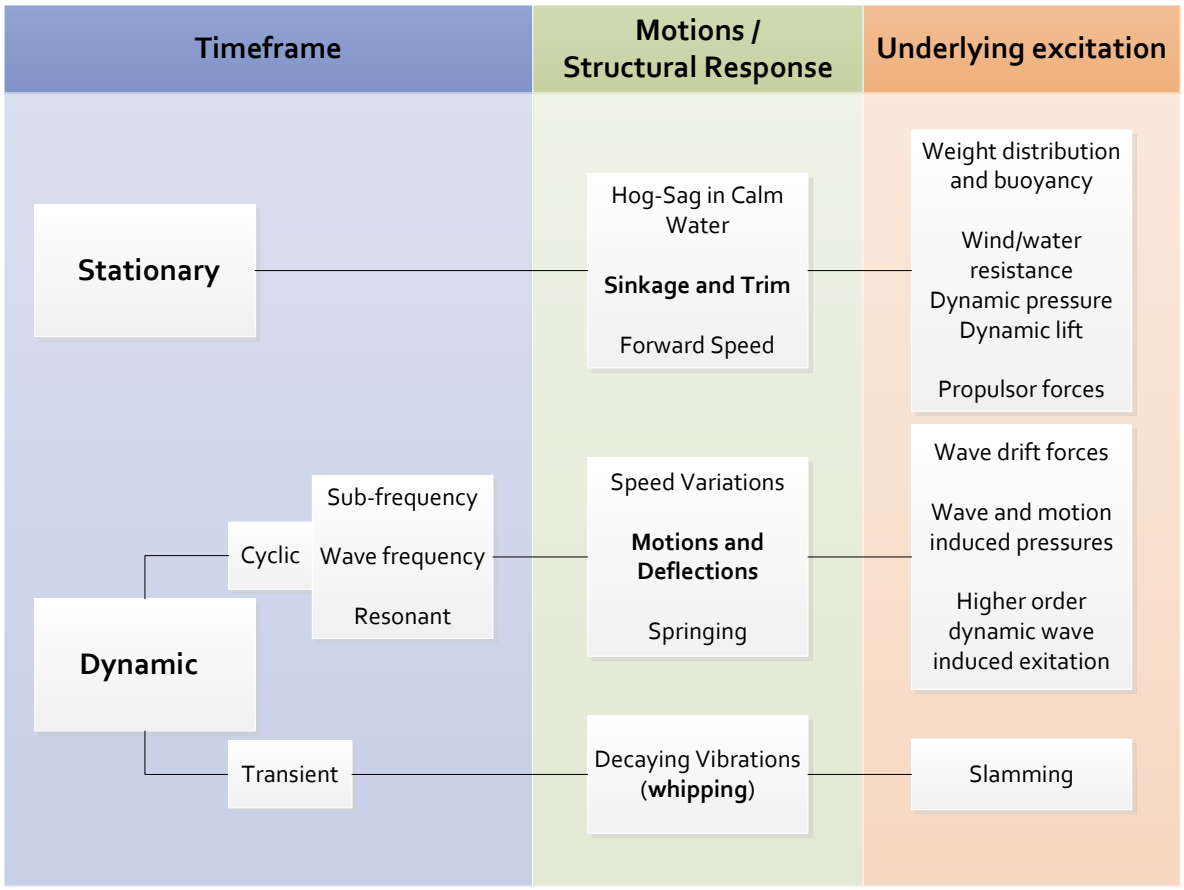

Figure 2-4: Governing excitation forces and ship responses. Partly based on [33].

2-4 Model segmentation

Considering global structural responses, the maximum shear force and bending moment along the hull are the most important parameters. The critical locations for these responses are about 0.25 L_{pp} and 0.75 L_{pp} for the shear force and 0.5 L_{pp} for the bending moment. The contribution from the 2-node mode is most important. In the case of an impulse load, (typically during bottom slamming) the 3 and 4-node may also contribute to the global response.

Three parameters are key for how well the flexible modes are represented. For models using a rigid backbone the modes are barely present, but the reliability of the integrated load representation is equally dependent on the three parameters.

1. Number of segments.
2. Cut location(s).
3. Mass distribution.

Generally, the accuracy of mode representation will increase with increasing number of segments, however it also adds complexity to the model. Per model this amount should be

considered. With flexible models, the amount of damping influences the reliability as well. Depending on the amount of damping, whipping response may be due to superimposed responses from two or more following slam events. Økland thoroughly compared 2, 3, and 4-segmented models [6]. The results for the VSF and VBM are summarized in the ensuing subsections. Table 2-3 summarizes the accuracy comparison for multiple measurement parameters.

2-4-1 2-segment model

In a 2-segment model only the 2-node mode is present. It has been demonstrated that the slam induced maximum VBM is governed by the response in the 2-node mode. For this reason, the 2-segment model shows a fairly accurate result. Nevertheless the model seems to underestimate the global structural response. The writer relates this to the inaccurate description of the 2-node mode. The prediction of global response is very sensitive to the location of the cut. This can be explained by the representation of the mode shape. The relative error is minimized by using a section cut at $L_{pp}/2$.

Sensitivity to changing *mass distribution* is examined for the 2-segment model. In Økland (2003) two cases have been investigated. The displacement is equal to the initial displacement (i.e. equal displaced water and trim/roll angles), however the mass distributions discrepancy manifests itself in a reduced and increased local radius of inertia for the aft and front section respectively. The second alternative has an increased mass for the aft section and a forward shifted Center of Gravity (CG) for the front section to obtain an equal global longitudinal CG. The change in mass distribution causes a relatively small error for option 1. Option 2 results in a more serious error. Økland concludes that a correct representation of the segment mass and CG are most decisive. Having equal radii of inertia for the segments is less critical.

2-4-2 3-segment model

The VBM is very well described by the 3-segment model. For the VSF the accuracy fluctuates depending on the applied load case. The accuracy of a slam with relatively short rise time and short duration can only achieved by the 4-segment model. Regarding the accelerations, the response in the 3-node is captured, however both the period and the mode shape is inaccurate.

2-4-3 4-segment model

Regarding the bending moment and shear force, all conducted load cases show excellent agreement between the experiment and the modeled continuous beam. Furthermore, only the 4-segment model shows well agreement with the modeled accelerations.

2-5 High speed craft implications

As a result of increased understanding of ship motion response, ship designs have significantly been improved (e.g. reduced vertical accelerations, increased cruising velocities). A prime example is the Enlarged Ship Concept (ESC) [34]. An ESC type ship such as the Stan Patrol

Table 2-3: Agreement with continuous beam numerical model for 2, 3 and 4-segmented models.

	2 segments	**3 segments**	**4 segments**	**Cont. beam**
VBM at $L_{pp}/2$	undervalued	very well	very well	benchmark
VSF	small deviation (2-node case)	very well (2-node case)	very well (all load cases)	benchmark
Accelerations	deviation up to a factor 2	false period / mode shape	very well	benchmark

4207 has operating velocities of around 30 kn. At this speed, the ship is in the semi-planing regime, meaning that the majority of the lift is still generated through buoyancy, with a substantial amount of dynamic lift present. Improved designs led to increased operability, meaning that the crafts could be operated in increasingly severe sea states. Where previously crew comfort was the limiting factor in the design of ships and operability, developments resulted in a shift. Current section discusses phenomena that are specifically valid for HSCs (not necessarily limited to HSCs).

2-5-1 Planing hull

Hulls are proved to introduce more hydrodynamic challenges when the level of planing increases. Dynamic stability gets important and the hydrodynamic forces become increasingly nonlinear. Examples of unwanted instability consequences are dynamic roll instability, broaching and porpoising. Furthermore, the high speed causes higher probability of cavitation and ventilation [35]. Equal as for more conventional ship types, both theoretical and experimental approaches are conducted in the past. Since experiments are more straightforward, this method was the predominated method in the early studies. Studies resulted in empirical relations for lift, drag and center of pressure for prismatic planing hulls. To the writer's knowledge, studies with the focus on experimental determination of internal forces (for planing hulls in particular) have not been published to date.

Due to the strong presence of non-linearities, application of analytically based linear solutions is limited. In the recent decades numerical solutions were introduced. Many numerical methods assume very high speed, or infinite Froude number for the vessel. With this assumption gravity can be neglected. However, only when gravity is included in the analysis of wave generation, the hydrodynamic features of a planing vessel in osciallatory motions will be frequency and Froude number dependent. Please refer to Section 2-6 for more elaboration on numerical code theories.

2-5-2 Slamming

High speed crafts advancing in waves are confronted with slamming loads. Slamming is often characterized by large hydrodynamic loads within a short duration. This type of load is more dangerous and less predictable than wave frequency loads. Slamming occurs when the ship's

hull emerges from the water and then quickly impinges the wave surface. Slamming can risk the integrity of the ship locally, and introduce a flexural vibration of the girder (whipping) increasing global structural load as well. Slamming can be categorized as:

1: Bow-flare slamming occurs when the bow emerges and quickly hits the water surface.

2: Bottom slamming usually follows if a significant length of the keel is exposed.

3: Stern slamming is a slamming event at the aft-most part of the ship.

4: Wet deck slamming occurs when the wet deck of a catamaran suffers an impact.

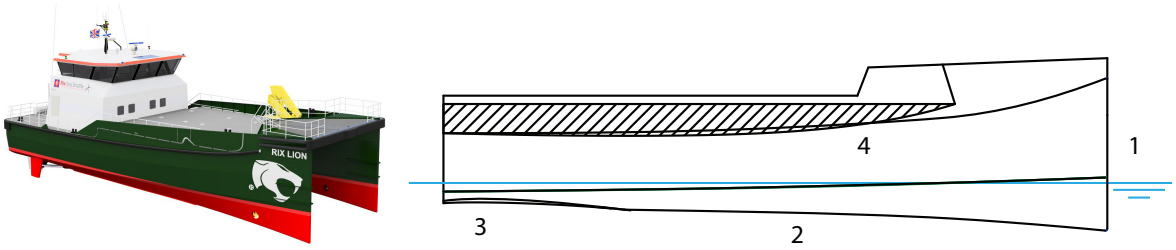

(a) Twin Axe FCS 2610 render. **(b)** Section cut with slamming locations.

Figure 2-5: Slamming types indicated on the Damen Twin Axe Fast Crew Supplier.

Figure 2-5 shows the approximate locations that distinguish the slamming types on a Damen Fast Crew Supplier catamaran. Please notice that for this particular vessel not all slamming types occur, the ship is merely used to indicate the locations. In addition to the mentioned four types, green water slamming can occur during the shipping of water on deck. For offshore structures, slamming is also of concern. Examples are the slamming on horizontal members of a jacket or on the deck of a platform. For HSCs bow-flare slamming and bottom slamming are most critical.

The effects of slamming loads are twofold. First of all, the high pressures can cause *local* structural damages. Amongst others, serious structural damages due to bow-flare slamming is reported by Yamamoto *et al.* (1985) [36]. On the other hand, the integrated loads due to large slamming pressures can greatly affect the *global* ship behavior. Global rigid-body motions can be affected by the local slamming (e.g. sloshing that significantly affects the global sway motions of a ship in beam seas [37]. The earlier introduced whipping is a transient global load effect. This is usually associated with the two-node vertical vibrations, as well as heave and pitch accelerations. Gu & Moan (2005) [38] demonstrated that the whipping related nonlinear loads can greatly increase the fatigue damage for a container ship with large bow-flare and low hull rigidity. The HSCs with aluminium hull or superstructure face similar fatigue problems. To conclude; different kinds of slamming events have important influences on ships and offshore structures. The fact that at high cruising speeds, slamming loads occur practically continuous, endorses the need to take slamming into account at the design process.

2-5-3 Fatigue

Today's HSCs are regularly built from aluminium. In Damen's design portfolio, below $\approx$ 35 m the hull- and superstructure are built from aluminium, above this value generally only

the superstructure is built from aluminium. An aluminium superstructure lowers the ship's center of gravity, thereby improving transverse stability. The key advantage is the savings in weight of the vessel; increasing carrying capacity and lowering the fuel consumption. On the other hand, using the material comes with higher production costs and in the design one must take the lower resistance to fatigue into account. From historical experience it is known that the welded bottom structures of aluminium HSCs can be vulnerable to local fatigue damage due to slamming. Moreover the global load, in particular the VBM, may lead to failure due to fatigue. This fact supports the demand for internal load prediction at this vessel type and is a key driver for this research.

2-5-4 Model weight limitation

As discussed, by using aluminium a saving in weight is achieved. The Stan Patrol's deadweight is 232,000 t, corresponding to 29.00 kg on 1/20 model scale. This relatively low weight restricts the material types that can be used to create a correctly scaled model. Due to an exceedance in weight, a rigid beam type segmented model cannot be constructed by using a steel beam for instance. Previous experiments involved a carbon fiber beam to ensure natural frequencies far beyond the excitation frequencies.

The weights of the previously used model parts are: 1.96 kg for the backbone and wooden supports; 2.80 kg for the front section and 2.84 kg for the rear section.

2-5-5 Neutral axis

The neutral axis is the definition for the axis in the (theoretical 2 dimensional) cross section of a member resisting bending. No longitudinal stresses or strains are present along this axis. Two types are distinguished, the elastic and plastic neutral axes. The *plastic* neutral axis is the location such that the tension on one side equals the compression on the other. In contrast, the *elastic* neutral axis is determined based upon equilibrating the moments of area of the tension and compression elements of the cross-section. With the linear elastic material behavior that is desired and expected in model tests, the elastic neutral axis is considered. Due to forward speed of the model, the neutral axis can shift from the geometric axis that is based upon pure bending. This phenomenon is discussed in the next section.

Shift due to axial stress

Figure 2-6 shows the front section of a HSC traveling in calm water at velocity V. Let's consider the neutral axis at the section cut as indicated. As a result of the acting local buoyancy/mass discrepancy, a certain amount of bending stress is present. The maximum value of this stress is also dependent on the geometric and material properties of the ship structure. In Figure 2-7 one can see that the geometric neutral axis σ_{Mb} is located on the top half of the ship's cross section. Due to the calm water resistance of the hull, a certain amount of 'axial' compressive stress σ_N is present in the material. The dynamic neutral axis' σ_{abs} position can be found by summing both stress graphs. In the current example, the position shifted downwards significantly.

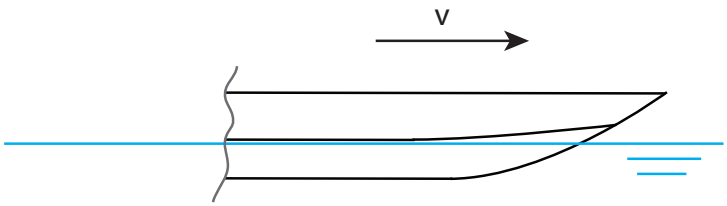

Figure 2-6: HSC advancing in calm water, front segment with hull cut at midship.

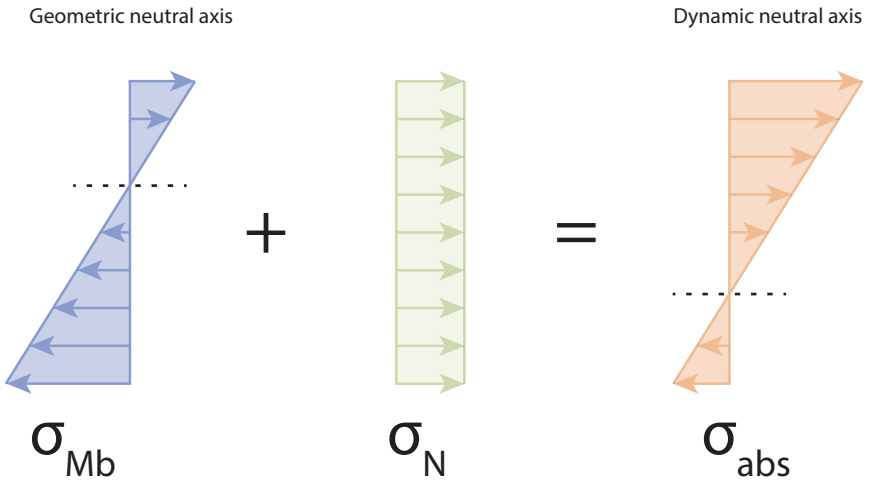

Figure 2-7: Superposition of the bending stress σ_{Mb} and axial stress σ_N results in the absolute stress distribution σ_{abs}.

Depending on the purpose of the research, different approaches are applied. Clauss (2007) [10] based the vertical position of the neutral axis only on the dynamic pressure forces. This complies with the definition of the plastic neutral axis. The hydrostatic pressure as well as the center of area of the structural components are not considered for determination of the vertical position of the neutral axis and the VBM at the water line or at deck level. This is due to the fact that the hogging-sagging (Figure 2-1) fatigue is the governing fail mechanism for the considered ship type (FPSO) and fatigue is not directly influenced by static forces or pressures. The experiments showed that the longitudinal forces had a significant contribution to the bending moment. This additional moment is counteracting, thus reducing the cyclic loads at deck level. This conclusion for moored vessel types confirms the assumption that the horizontal component influences the existing vertical bending moment. The next subsection outlines the acting pressures and their contribution to the bending moment. From that it can be concluded that the level of influence depends on factors including the propulsion, submerged hull surface and the ship's structural properties.

Influence of shift in backbone position

As introduced at the beginning of this subsection the definition of the neutral axis is ambiguous for complex structures as ship hulls. When speaking of the neutral axis at model scale

ship, additional explanation is desirable as well. For a fully elastic ship model the neutral axis' position can be reproduced relatively accurately from the full scale ship position. With a segmented type with interconnecting backbone, the structural stiffness is merely present at the backbone[2] and therefore the position of the backbone has a major influence on the measurement values at the backbone or the interface of backbone and the segment(s). On the basis of an example this influence is illustrated qualitatively.

Figure 2-8 shows a 2-dimensional simplification of the hydrostatic pressure $p_{stat}(z)$ acting on the aft hull segment. The pressure integrated over the hull surface results in a horizontal and vertical force component; F_h and F_v respectively. Due to the linear increase of hydrostatic pressure over depth, the resultant horizontal force is equal to $^1/_2 \cdot p_{stat}(d) \cdot d$, with draft d (equal to the distance between to water line and the ship's keel). The horizontal force's resulting point of action is located at $^2/_3\, d$. The vertical force is located at half of the length of the segment $L/2$. After integrating the local pressure over the segment length, the magnitude of the vertical force is expressed as $p_{stat}(d) \cdot L/2$.

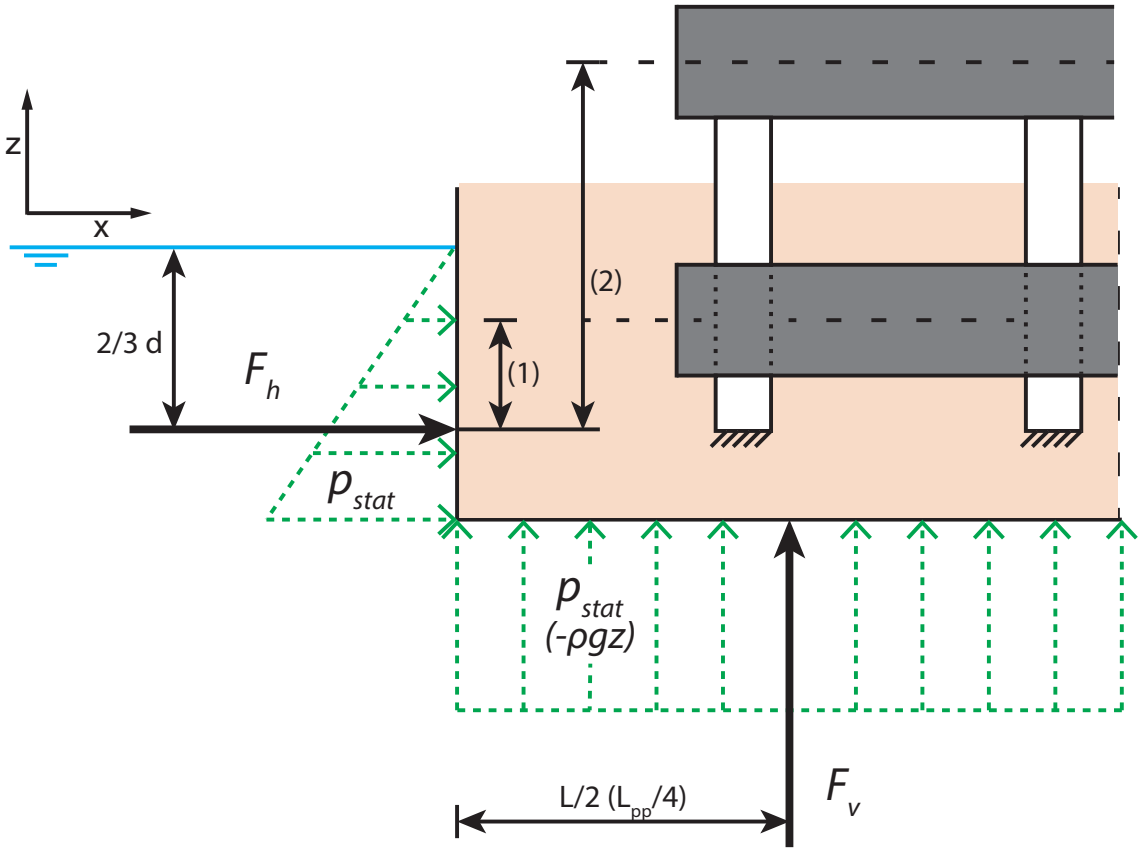

Figure 2-8: Calm water hydrostatic forces acting on the aft hull segment.

The gray bar is a representation of a half-backbone, showed at two arbitrary locations. The vertical distances (1) and (2) from F_h can be seen as two options to place the backbone. In the schematic drawing the rigid backbone is rigidly connected to the segment via the white connecting elements. Please note that at the actual set-up hinges and/or force transducers are

[2]Stiffness of the seal that waterproofs the assembled segments is considered negligible.

present rather than the rigid body elements. However for displaying reasons this simplification is applied here.

Please note that although these forces do change with changing draft/trim, they can be considered earthbound. In contrast, the VBM and VSF are calculated using the shipbound forces since the force transducers are fixed to the model. Section 2 of Appendix C outlines the conducted transformations to obtain the earthbound force equilibria from the measured shipbound forces. The italic printed forces in Figure 2-8 and Appendix C indicate earthbound forces.

The VBM at midship is caused as a result of both the vertical force and the horizontal force. For the vertical force, a shift in location leaves the resulting bending moment unchanged. The (N.B. *counteracting*) bending moment due to the horizontal force is different for (1) and (2). The example demonstrates the relevance of being aware of the vertical position of the backbone and its influence on the measured forces and bending moment(s). This is valid for measurement at the backbone as illustrated in the figure, and for when force transducers interfacing the backbone and the segments. As Clauss indicated [10], the horizontal component is counteracting, increasingly lowering the VBM, in this particular example also named Still Water Bending Moment (SWBM) for increasing vertical distances between the point of action of the horizontal force component and the backbone.

Naturally, with propagating waves and forward speed the vertical and horizontal forces will change significantly. However, the resulting forces are still generated through pressure integration over the surface and the load path in the assembly remains unaltered. From the illustrated situation it can also be concluded that the contribution of the horizontal components, diminishes at situations where the structural member is located close to or at the vertical positions of these components (i.e. thrust and resistance). At a ship model with the backbone positioned near or below the water line this applies. The model experiments may confirm this.

2-6 Seakeeping (numerical code) theories and application

Part of the research is identification of the required validation parameters. For the Stan Patrol ship, the validation will eventually be executed for the FASTSHIP routine. This routine is buildup from the nonlinear strip theory. However, the research goal is to develop an experimental set-up for a fast moving scale model ship. Therefore, the section considers any arbitrary strip theory numerical routine. After presenting a brief overview of the potential flow theories used for development of seakeeping simulation routines, the formulae used by FASTSHIP are presented. Since motion response calculation is not in the current scope, this matter is rather briefly formulated.
With the growing available amount of computational power, more demanding methods using Computational Fluid Dynamics (CFD) are used increasingly. However, CFD and its applications with respect to internal load calculation is not in the current scope of work and besides a brief introduction in the subsequent section, the method is not further addressed in the thesis. An important reason for this is the fact that with the current state of art, CFD seems unusable for simulation of bodies that operate at high speeds.

2-6-1 Methods for ship motion and load calculation for ships with forward speed

One can distinguish two main theories to calculate behavior of advancing ships. Initially potential theory was the sole option to solve this type of problems. The majority of methods for ships at forward speed is still using this theory, ranging from linear and hybrid to fully nonlinear. CFD is the other fundamental theory that is used, which uses Reynolds-Averaged-Navier-Stokes (RANS) equations as its foundation. The calculation methods may be classified using 6 levels:

- Level 1 (Linear)
- Level 2 (Froude-Krylov nonlinear)
- Level 3 (Body nonlinear)
- Level 4 (Body exact – weak scatterer)
- Level 5 (Fully nonlinear – smooth waves)
- Level 6 (Fully nonlinear)

Below, per level the main characteristics are briefly discussed. For a more in-depth description and examples of recent studies per method read section 2.2 of the recently published review titled *Loads for use in the design of ships and offshore structures* (2014) [39]. The subsection closes with emphasis on numerical methods for planing crafts.

Level 1 methods can be considered as the founding methods of potential flow theory for ships with forward speed. The earlier methods assume a linear system, i.e. the motion response amplitudes are linearly related to the incoming wave amplitude. This assumption is only valid for infinitesimal motion response around the equilibrium position and the incoming waves have a limited steepness. By using the superposition principle for the waves and motions, the method can be used for irregular waves as well. The procedure is usually referred to the frequency domain approach. The linear strip theory uses the assumption of linearity is the most widely used method for quick motion response calculations. The theory represents the ship hull by a series of two dimensional cross sectional strips, on which the forces are calculated independently. It can only be used for slender structures, making it unsuitable for offshore structures such as semi-submersibles. Further developments of the strip theory led to properly validated code for advancing ships. Simulating large asymmetrical motions (e.g. roll, sway, yaw motions) were found unsuccessful with strip theory. Further developments led to the linear frequency domain three-dimensional diffraction theory. Equal to the strip theory, it assumes linearity and superposition, but the requirement of slenderness is not present. Several attempts to include forward speeds were relatively unsuccessful, especially for higher Froude numbers. Some seakeeping methods have recently been modified to enable analysis for special vessels such as HSC please refer to the end of this subsection for more detailed information on methods for planing crafts.
Level 2 methods use the same calculation method to calculate the disturbance potential. The incident wave forces are evaluated by integration of the incident wave pressure and the hydrostatic pressure over the wetted hull surface. This surface is defined by the instantaneous position of the hull under the incident wave surface. The level 2 methods are very popular since many important nonlinear effects are taken into account with only limited amount of computational power required compared to level 3 methods.
Level 3 methods are scarcely used since the required computational costs are dramatically

higher than Level 2 methods. Here, the disturbance potential is calculated for the wetted hull surface which is defined by the instantaneous position of the hull under the mean position of the free surface. The disturbance potential must be re-gridded and recalculated for every time step.
Level 4 methods are similar to level 3 methods, except that the wetted hull surface is now defined by the instantaneous position of the hull under the incident wave surface. The methods are sometimes referred to as "weak scatter methods", since the scattered waves, caused by the ship are disregarded when the hydrodynamic boundary value problem is set up. The methods assume small wave disturbance compared to the incident waves and the steady waves.
For level 5 methods the scattered waves are no longer assumed to be small, and they are included when the boundary value problem is set up. These methods do assume 'smooth' waves; there is no wave breaking or fragmentation of the fluid domain. As a result the computations are forced to stop based on a wave breaking criterion.
For the potential theory it can be concluded that the boundary integral methods that are used cannot handle breaking waves, spray and water flowing onto or off the ship's deck. Moreover, viscous forces are not considered and should be calculated using other methods. Level 6 methods do not make use of the potential theory. In contrast to potential theory they make use of RANS equations, and the water/air volumes are discretized. As mentioned earlier, CFD requires a significant amount of computational power, making it less suitable use in the earlier design phases. These phases are characterized by quickly varying hull forms or even structure concept selection.

Methods for planing crafts

Seakeeping methods for planing hull ships underwent a separate development path. The first type of approach is based on solving the two-dimensional impact of a wedge with potential flow boundary element methods. Most of the studies assume zero gravity; greatly simplifying the free surface condition. Typically these methods are used either to solve the slamming problem or simulate high-speed planing, very often only in calm water.

The second approach to the problem uses the falling wedge theory. This theory was initially used for calculating the behavior of seaplane floats, first published by Von Karman [40]. Further developments considered non linearity: Zarnick (1978) [41], and Keuning (1994) [34]. Keuning's model includes variable deadrise hulls in irregular waves and empirical formulations for the trim and sinkage based on model tests, stretching the applicability of the method into a wider speed range. Using this foundation, Cleine & Deyzen [3] developed a routine in FASTSHIP that adds internal load calculation for semi planing vessels in calm water or head waves.

At present, this model is not validated. This simulation model should take into account the hydrodynamic lift, the steady-state sinkage and trim, the non-linearity of the response and it must be able to predict large vertical peak accelerations.

The following subsections briefly describe the theory behind the internal load calculation.

2-6-2 Equations of motion

The numerical FASTSHIP model and experiments consider forward speed and head waves. For this reason, and since the hull is symmetric with respect to the x-z plane, a 2-d representation is used. In the Cleine model, three degrees of freedom are considered: surge (x), heave (z) and pitch (θ).

$$\begin{aligned} Surge &: M \cdot \ddot{x}_{CG} = T - F_{dyn} \cdot sin(\theta) - D \cdot cos(\theta) \\ Heave &: M \cdot \ddot{z}_{CG} = W - F_{dyn} \cdot cos(\theta) - F_{sta} \\ Pitch &: I_{yy} \cdot \ddot{\theta} = F_{dyn} \cdot x_a + F_{sta} \cdot x_b \end{aligned} \tag{2-18}$$

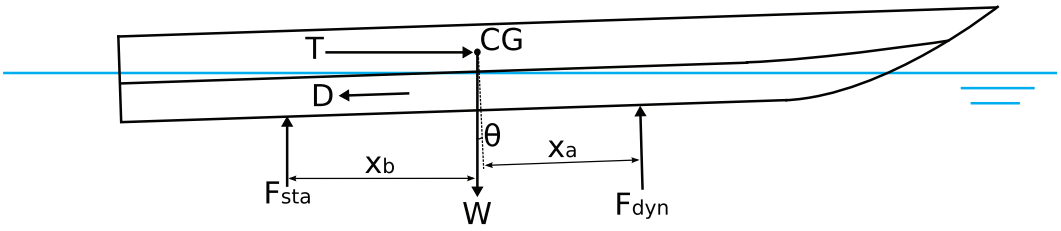

Figure 2-9: Forces acting on the hull as used in the fastship routine. [3]

The equations assume that the thrust T acts horizontally in the CG. The drag D is body fixed and oriented horizontally at trim angle $\theta = 0$. The dynamic and static forces are oriented vertically and counteract the ship's weight W [N]. The routine neglects the vertical frictional component and its contribution to the pitch moment and it neglects wave making and spray rails resistance and whisker spray drag.

For the model experiments, the drag is earth fixed and always oriented horizontally. The drag counteracts the thrust at all times. As a result the surge acceleration is zero for the considered measurement interval, where the velocity is constant.

2-6-3 Analytic expressions for internal loads

The shear force can be calculated by supposing the the ship as a Timoshenko beam. Consider a infinitesimal ship section with length dx_b to calculate the vertical shear forces Q and bending moments M. The resultant load $q(x_b)$ on the piece creates an extra force dQ and moment dM. Figure 2-10 schematically illustrates the loads on a arbitrary cross section with length dx_b.

The VSF at a cross section with x-coordinate $x_b = x_1$ can be calculated by integration of the load distribution.

$$Q_z(x_1) = -\int_{stern}^{x_1} q(x_b) \cdot \mathrm{d}x_b \tag{2-19}$$

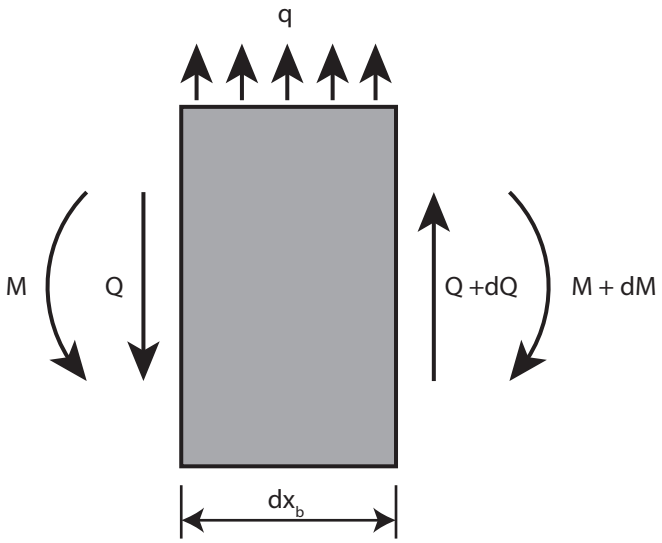

Figure 2-10: Loads on a cross section.

Equivalently the vertical bending moment can be calculated.

$$\begin{aligned} M_y(x_1) &= -\int_{stern}^{x_1} \cdot q(x_b) \cdot (x_1 - x_b) \cdot \mathrm{d}x_b \\ &= +\int_{stern}^{x_1} q(x_b) \cdot x_b \cdot \mathrm{d}x_b - x_1 \cdot \int_{stern}^{x_1} q(x_b) \cdot \mathrm{d}x_b \\ &= +\int_{stern}^{x_1} q(x_b) \cdot x_b \cdot \mathrm{d}x_b + Q(x_1) \cdot x_1 \end{aligned} \tag{2-20}$$

The load $q(x_b)$ consists of solid mass and hydromechanical terms. Eq. (2-19) and (2-20) represent the static equilibrium.

The **dynamic equilibrium** is formulated using Newton's second law. Combining the static and dynamic component, the maximum shear force and bending moment is obtained.

For the vertical dynamic loads acting on a section with length $\mathrm{d}x_b$, the harmonic longitudinal and vertical dynamic loads per unit length on a transverse 'slice' of the ship is given by:

$$\begin{aligned} q_x(x_b) &= +X'_{hx}(x_b) + X'_{wx}(x_b) - m'(x_b) \cdot \{\ddot{x} - \overline{bG}(x_b) \cdot \ddot{\theta}\} \\ q_z(x_b) &= +X'_{hz}(x_b) + X'_{wz}(x_b) - m'(x_b) \cdot \{\ddot{z} - x_b \cdot \ddot{\theta}\} \end{aligned} \tag{2-21}$$

Where:

- $\overline{bG}(x_b)$ is the distance of the centroid of the cross section to the x_b axis [m].
- $X'_{hx}(x_b), X'_{hz}(x_b)$ and $X'_{wx}(x_b), X'_{wz}(x_b)$ are the sectional hydromechanical and wave forces for surge and heave, respectively [N].

Using (2-19) and (2-20) the harmoning vertical shear force and bending moment at cross section x_1 become:

$$\begin{aligned} Q_z(x_1) &= Q_{z_a} cos(\omega_e t + \epsilon_{Q_z\zeta}) \\ &= -\int_{stern}^{x_1} q_z(x_b) \cdot \mathrm{d}x_b \end{aligned} \tag{2-22}$$

$$\begin{aligned} M_y(x_1) &= M_{y_a} cos(\omega_e t + \epsilon_{M_y\zeta}) \\ &= +\int_{stern}^{x_1} q_z(x_b) \cdot \overline{bG}(x_b) \cdot \mathrm{d}x_b + \int_{stern}^{x_1} q_z(x_b) \cdot x_b \cdot \mathrm{d}x_b + Q_z(x_1) \cdot x_1 \end{aligned} \tag{2-23}$$

With similar theory, the lateral dynamic loads can be calculated. By the nature of the current objective and the associated experiments, these loads expect to play no relevant role here. For reference please read chapter 8.7 of Journee, Massie (2001) [42] for the corresponding formulas.

Boundary Conditions

The equations above are solved adhering the boundary conditions. The conditions apply at the stern and at the bow, indicated with (0) and (L_{pp}) respectively. The boundary conditions are valid for all structures that can be considered as a free-free beam: no shear forces and moments are present at the boundaries.

$$\begin{aligned} Q(0) &= 0 \\ Q(L_{pp}) &= 0 \\ M(0) &= 0 \\ M(L_{pp}) &= 0 \end{aligned} \tag{2-24}$$

2-7 Concluding

Chapter 2 introduced aspects that must be considered when performing model tests for high speed crafts. More specifically: experiments to determine the VSF and VBM at model scale. A segmented model with interconnecting rigid backbone is relatively easy to fabricate and remains usable with a change in structural stiffness of the design. This makes the rigid (backbone) concept the preferred option over a flexible backbone or fully flexible model. Literature indicates that for obtaining the global bending moments and shear forces a 2-segment model is sufficient, however for example a 4-segment model is required for correct measurement of accelerations. For planing HSCs in waves slamming loads are governing in the total of acting forces. For the experimental set-up, one should be aware that placement of the backbone, in particular its vertical position, influences the outcome of experiment results. The chapter ends with a brief introduction to potential flow theory and its application in FASTSHIP. In the view of the discussed aspects, the next chapter describes the design of the experimental set-up more detailed.

Part II

Experiments

Chapter 3

Measurement set-up development

Chapter 3 considers the design part of experimental research of scale model testing. The chapter starts with providing an overview of the requirements and goals of the experiments. The ultimate goal is to develop a method to accurately measure internal loads on planing hulls, hence ships sailing with relatively high Froude numbers. To systematically evaluate the results, the experiments increase in the number of disturbance factors (e.g. forward speed, dynamic oscillation, irregular waves generation etc.) when the set-up proves reliable. The distinct experiments are discussed in the next chapter which outlines the operational aspects of the experimental research.

Before discussing the objectives and requirements, preliminary experiments and their results are discussed. By carrying out experiments that imitate the prior (unsatisfactory) set-up, more knowledge on the physical phenomena is obtained. This knowledge is applied at the set-up concept development sections. These sections consider the method of force measurement, physical interface(s) with the carriage or towing tank and the equipment for data acquisition. The final section is a wrap up and summarizes the final design that will be used in model experiments.

3-1 Experimental problem identification

A broad range of experiments was conducted to obtain more insight on the load path of the prior used set-up. Additionally, the force transducers used are thoroughly examined for sensitivity for cross talk. Current section summarizes the experiments in chronological order with the associated results.

The maximum applied load here was $\approx$ 100 N in both vertical[1] and horizontal direction. In consequence, the maximum Vertical Bending Moment (VBM) at midship is $\approx$ 100 Nm. To put this into perspective; the applied moment during earlier carried out experiments with the segmented ship yielded a Still Water Bending Moment (SWBM) in the order of 10–15 Nm.

[1] here vertical is defined as the direction parallel to the direction of the gravitational acceleration vector.

Loads measured at the transducers were valued up to ≈ 50 N horizontally and vertically. The maximum values of the applied loads here were considerably higher to increase the visibility of errors in the set-up configuration.

3-1-1 Vertical load and -moment representation

The goal of these experiments was to replicate part of the measurement set-up as used previously in the research of A. van Hoeve. Van Hoeve carried out experiments with the same segmented hull, however the results were considered not reliable. This fact is the direct reason for the present research. In the current set-up, the backbone is partially fixed to a steel table, representing the fixed world. The other half is connected to a wooden plate representing one ship model section. At the connection, (1) force transducers are placed similar to the prior set-up and were placed using (2) an altered set-up containing hinges. The influence of the hinges was evaluated and documented. Figures 3-1 and 3-3 schematically demonstrate the measurement arrangements. Please note that the figures are not drawn to scale. It is shown that the reliability for measurement of vertically directed forces increases significantly after applying the hinges in the experimental configuration. Any potential bending moment is uncoupled; it is no longer transferred through any of the force transducers. The results show that when only vertical forces are present, determination of the VBM at midship is expected to be considerably more accurate. This applies for determination of the still water bending moment for example. Loads applied directly at the backbone were not noticeably registered by the force transducers. In case of large pitch angles earthbound loads shift from the vertical to horizontal transducers and vice versa. This should be accounted for during interpretation of measurement data. Measurement of horizontal load proved unreliable. A part of the applied load 'leaks' at the set-up containing hinges as well as the set-up without hinges. In contrast to the vertical forces, the error increased by applying hinges. During the experiments, horizontal loads are exerted by waves and drag at (high) forward speeds.

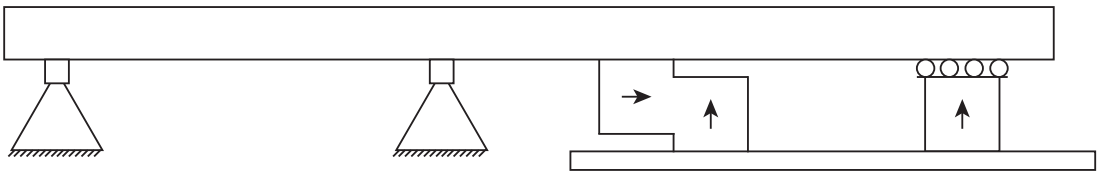

Figure 3-1: Replicated prior set-up.

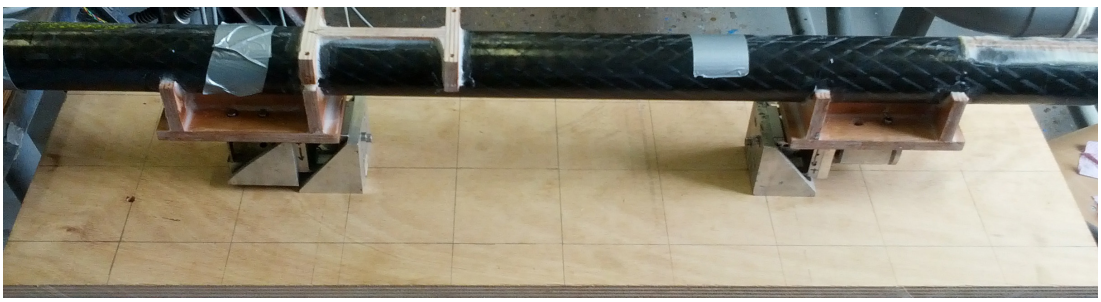

Figure 3-2: Photograph of free hanging part – prior set-up.

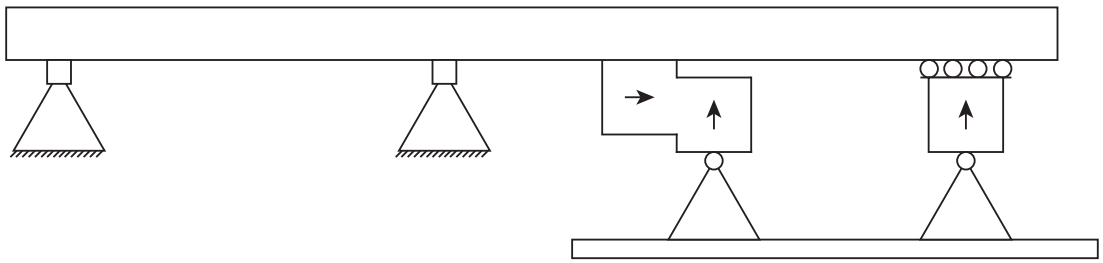

Figure 3-3: Replicated prior set-up – added hinges.

Therefore correct measurement of the horizontal forces requires particular attention during the research and design of the measurement configuration. Furthermore, the experiments provide arguments to calibrate the set-up after assembly in addition to calibration of the individual components. These experiments resulted in a request for more experiments, focused on registration of horizontal loads. However, first the set-up was disassembled to test the registration of a moment transferred by the force transducer and its sensitivity to load perpendicular to the intended load direction (i.e. horizontal load for a transducer oriented to register vertical load).

3-1-2 Sensitivity to applied torque and 'parallel' load

Tests have been carried out to increase the understanding of the transducers' sensitivity to load that potentially disturbs measurement of the load in direction of interest. Two main topics are investigated. The first topic was determining the relation between applied moment and the measurement value of the force-transducer. The set-up is formed by a single transducer which is fixed to the steel table. A horizontally oriented rod is attached and a fixed amount weight is translated over the rod to increase the applied moment with constant force. The used masses measured 2 and 4 kg, hung at distances ranging from 10–50 cm. Please refer to Figure 3-4 (left). Alternatively, an increasing moment is created by keeping the moment arm $L/2$ constant while increasing the weights shown in the right side of figure 3-4.

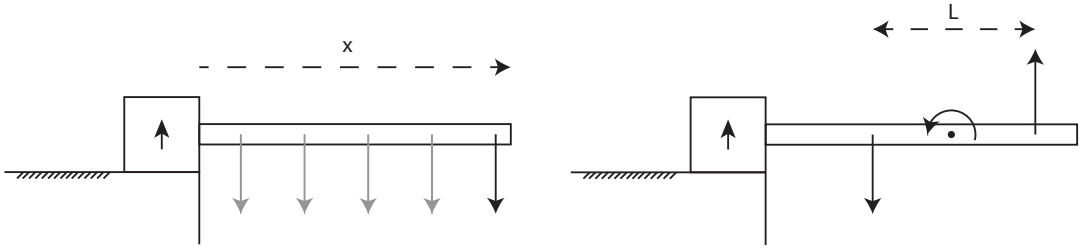

Figure 3-4: Set-up for testing torque sensibility.

Figure 3-5 shows the change of registered (vertical) force as function of the applied moment. As a result of the used weights and arms, a moment of up to 20 Nm is applied. The left axis shows the difference [N], the right axis shows this value divided by the applied moment [1/m]. The graph shows a fairly linear relation between the error and the applied moment. The green (dashed) line is not completely constant valued, showing a slight progressive course.

In the prospective testing environment, VBM values up to 20 Nm are feasible. This is not equal to the torque that is transferred through the force transducers however. From static equilibrium, these values are roughly an order of magnitude smaller.

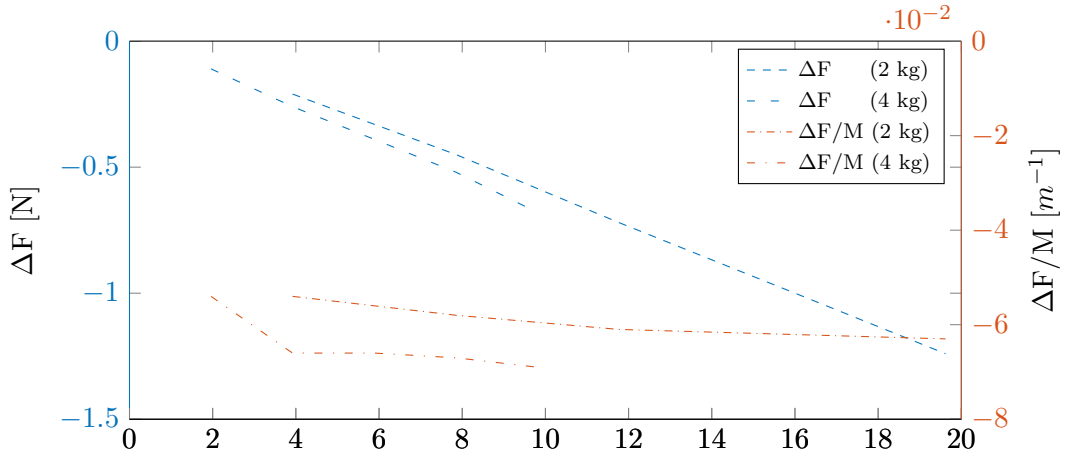

Figure 3-5: Force transducer's sensibility to torque.

Parallel load was applied by positioning the force transducer directly on the steel table and place weights on the force transducer. At the 2–10 kg placed weights the sensor reading was constant. Here from it is concluded that the force transducer is insensitive to weight placed perpendicular to the intended measurement direction. The third (second perpendicular) direction is irrelevant since no considerable forces in that direction are expected. This is due to the symmetric hull shape and no drift angle and waves other than head waves during experiments.

3-1-3 Horizontal- and combined load

The set-up containing three force transducers is evaluated for a second time. Former experiments show minimal deflection of the carbon fiber backbone, nevertheless now the transducers are fixed to a steel table to eliminate any potential deflection at the 'backbone side'. The hinges used in previous experiments are altered, lowering the moment arm that is generated through the horizontally applied load. The hinges allowed several mm of play in the direction perpendicular to the vertical and horizontal load. Results show that the vertical load representation yields considerably accurate again (i.e. avg. error $< 1\%$)

The focus during the experiments is on the combination of vertical load and horizontal load. This is since the horizontally applied and measured load show a significant discrepancy.

Friction at the pulley is potentially present. The pulley is used to guide the steel cable, which in its turn is used to transfer the horizontally applied load. Please refer to Figure 3-6, *(c)* for a schematic view of the measurement set-up. Tests results yield that friction in the pulley can be neglected. The set-up was able to register an added amount weight of 20 g, which is almost similar to the resolution in which the transducer can register.

Load conditions that were present during the experiments are listed in Table 3-1. Asymmetric load at (a) was applied as well, however the processed results proved inaccurate due

to the low amount of vertical load transferred through the roller support (i.e. a block sliding on ball bearings, serving as roller support). These results are therefore not included in Figure 3-7. In this figure, the conditions are plotted, together with the average and linear fit. The vertical axis' ticks show the leaked amount of applied horizontal load F_h divided by the applied vertical load F_v that is transferred through the roller support. Here, the load consists of the weight of the wooden plate and one hinge, with added weights (Table 3-1) in particular cases. The horizontal axis states the amount of applied horizontal load (c) ranging from (offset corrected) 0 to 10 kg. N.B. the horizontal load F_h is equal to the applied load [kg] multiplied by the gravitational acceleration g. By using MATLAB, a linear fit is created and indicated in the figure by a bold black line. The parameters of the linear fit are stated in Eq. (3-1) and in the legend of Figure 3-7. *Settled* instances imply that at each measurement the set-up was gently hit with a hammer to minimize effects of phenomena such as misalignment and stick slip.

$$\begin{aligned} y(x) &= P(1) \cdot x + P(2) \\ P(1) &= 0.021 \\ P(2) &= 0.066 \end{aligned} \tag{3-1}$$

P(2) is the value that is correlated to vertical load that is transferred through the roller support. The coefficient states that F_h offsets 0.066 N per Newton of transferred vertical load through the roller support.
P(1) is correlated to the moment that is transferred through the roller support. This moment is generated by the horizontal load and is created through the arm d from the center lines of the hinge and roller support. The coefficient states that F_h offsets 0.66 N per kg of applied horizontal load. Equally, from Newton's first law: F_h offsets 0.27 N/Nm (from $m \cdot g \cdot d$) with m being the hung mass [kg] at (c) and d the arm; valued 0.042 m for this set-up.

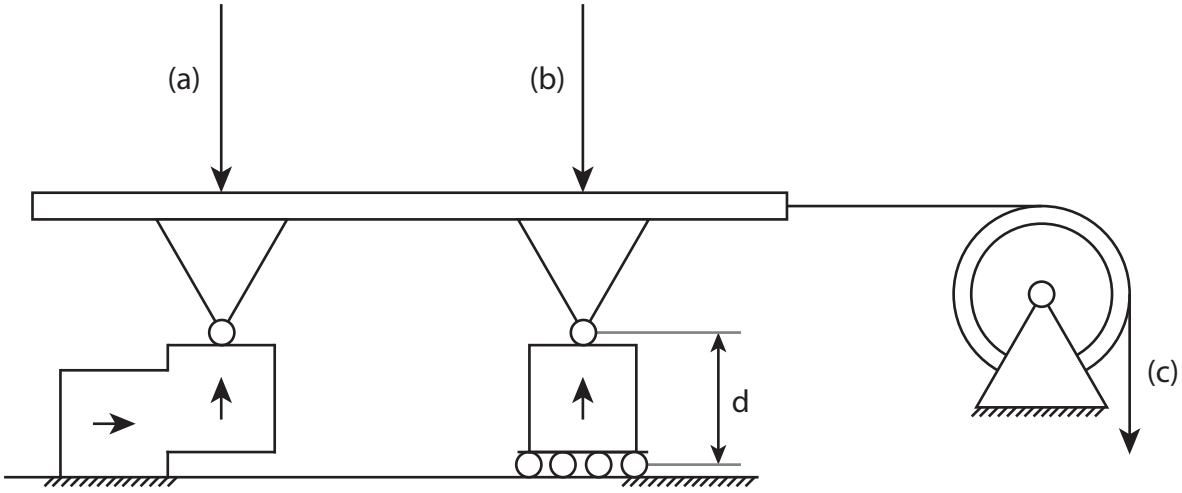

Figure 3-6: Experimental set-up – schematic side view. N.B. the figure is not drawn to scale.

It is indisputable that with the outlined set-up a significant deviation between the applied load and measured load values is present. Where the vertical components are measured within 1 percent accuracy, the horizontal transducer shows deviations up to 25 N at $\approx$ 100 N horizontal load. From experiments, it appeared that the deviation is correlated to both the

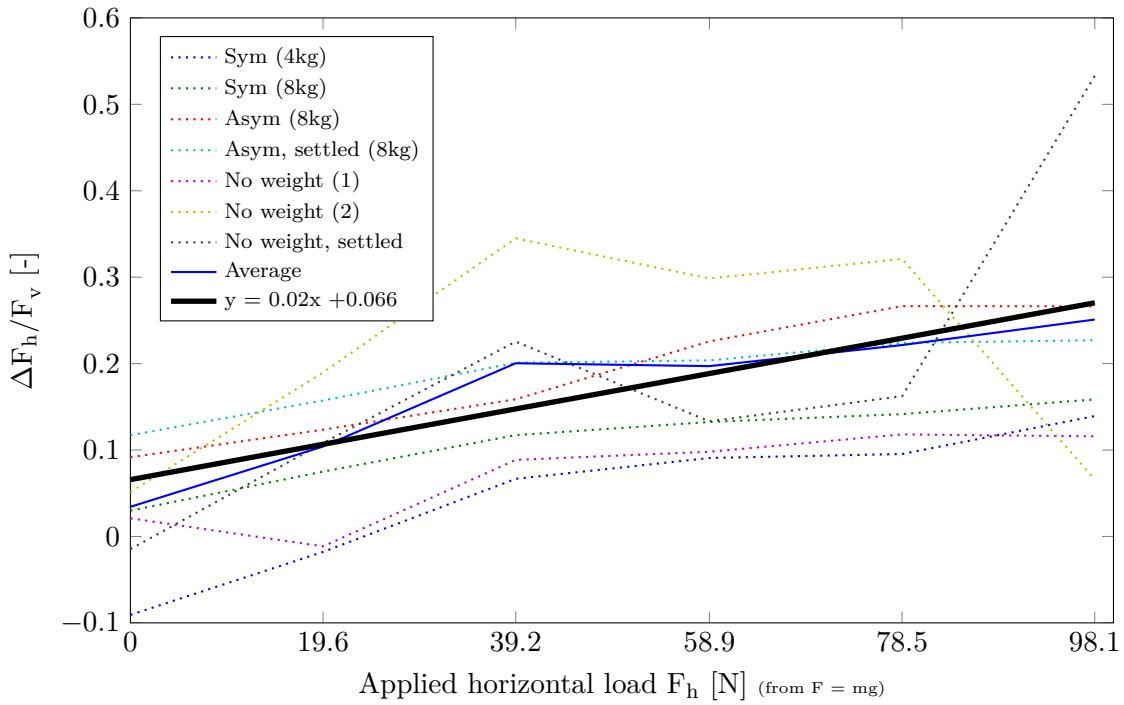

Figure 3-7: Leaking F_h as function of applied vertical and horizontal loads.

Table 3-1: Load conditions during the experiment.

Name in Legend	(a)	(b)	Settled
Sym (4kg)	2 kg	2 kg	No
Sym (8kg)	4 kg	4 kg	No
Asym (8kg)	0 kg	8 kg	No
Asym, settled (8kg)	0 kg	8 kg	Yes
No weight (1)	0 kg	0 kg	No
No weight (2)	0 kg	0 kg	No
No weight, settled	0 kg	0 kg	Yes

applied vertical and horizontal load to the set-up. When a linear relation is assumed at for the measurements plotted in Figure 3-7, the following correlation exists in the linear elastic region of the force transducers:

1. correlated with vertical load transfer through the roller support.
2. correlated with the generated moment through horizontal forces acting on the ship segment.

The exact values for the coefficients are less important, and should be calibrated in each setup. Nevertheless (3-2) states the correlation quantitatively. The value correlated with the vertically applied force can be linked to the friction coefficient of steel to steel contact. In

this particular case the friction coefficient can be expressed as $\mu_{steel-steel} = 0.0657$ $[-]$. To a large extend, this value agrees to the static friction coefficient[2] of greasy hard steel - hard steel contact (values ranging from 0.05 to 0.11).

$$\Delta F_h = 0.0657 \cdot F_{v,rs} + 0.271 \cdot M_{F_h} \tag{3-2}$$

- $F_{v,rs}$ is the vertical force transferred through the roller support $[N]$.
- M_{F_h} is the moment created by the horizontal load, acting on the roller support $[Nm]$.

3-1-4 To conclude

It is certainly plausible that friction at the roller support results in leakage of horizontal forces. The friction is created through a vertical force and -moment that is created by any horizontal load. The outlined linear correlation assumes that this is the only factor causing the discrepancy. Section 2-2 demonstrates that the used force transducers are too sensitive to cross-talk of applied torque. Compared to the deviation that is present during the conducted experiments, the contribution of this deviation factor is marginal.

From the experiments lessons can be learned regarding the use of set-up parts that *should* operate as frictionless roller supports. The geometry of this part and the load path that is present most probably results in the significant amount of leaking horizontal force. The part consists of stationary operating ball bearings, while the bearings are designed to revolve. Stationary, and in the current configuration, the resulting friction turns out to greatly exceed the (earlier) expected values. Alternatives to this configuration are presented later. First the objectives and requirements are systematically outlined.

3-2 Objectives - Load cases

Earlier sections stated the objectives for the study as a whole. These objectives can only be achieved if all relevant load cases are considered. The enumeration below briefly mentions the proposed type of experiments to systematically verify the applied theory. The first items' goals are to calibrate the load sensors and to verify the experimental set-up by applying known forces. After a successful verification, measurement series aimed to validate numerical code can be conducted. The test program will be composed using the enumeration. For further reading, please refer to the following chapter, Section 4-2.

1. (Quasi) static.
   (a) Predefined loads (dry testing).
   (b) Non moving ship in calm water.
   (c) Ship towed in calm water at different velocities.
2. Dynamic, regular waves.

[2]Source: http://www.engineershandbook.com/Tables/frictioncoefficients.htm

(a) Non moving ship in regular waves.

(b) Moored.

(c) Towed at different velocities.

3. Dynamic, irregular waves.

(a) Towed at different velocities.

3-3 Functional requirements

The geometric and dynamic scaling factors were discussed in 2-2, the emphasis in this section is on requirements regarding the structural part. For a ship design that is in an early phase of its development, many (structural) factors are still unknown and prone to change. These facts alone make an exactly scaled ship impossible. Structural similarity requires the construction, the mass distribution, the Center of Gravity (CG), moments of inertia, stiffness and geometrical neutral axis to be similar. In practice the mass distribution cannot be properly scaled. However, research shows that reliable results can already be obtained when the CG and moments of inertia are correctly scaled. Except one option, all concepts considered in the current study, the scale model is sawed in two vertically and connected via a backbone. The created gap at midship should be sealed to prevent water from entering the model. Furthermore it prevents a pressure drop at the midship cut. The seal must be constructed using a flexible material to minimize the influence on the (bending) stiffness. The ITTC guideline Global Loads Seakeeping Procedure paragraph 2.2.2 states that the sealed gap is typically 5–10 mm [31].

The use of a rigid backbone to connect the two segments is inherent to using an internal force measurement system that consists of force transducers connecting the backbone to the segments. The minimum amount of vertical force transducers is equal to the number of connection points. Regarding measurement of the horizontal forces, the required amount is disputable. However, one transducer per segment is minimally desired. A flexible backbone allows for measurement of the VBM directly on the backbone. Although marginal, the carbon fiber backbone will deform under load. The potential strain will be considered and evaluated in this thesis. Linearity of deformation (and resulting strain) is required since the calibration of the strain gauges, but more importantly verification of the complete system of sensors, is based on linear elastic behavior. Furthermore, no (or only a negligible amount of) hysteresis may be present in the system to ensure repeatability of measurements.

The fixation to e.g. the towing carriage may not lead to motion response that cannot be linked to the full scale ship. In the first place this implies that the model must be free in heave and pitch. Moreover, the full scale thrust must be resembled correctly (i.e. the combination of point of action and direction resulting in an equal trimming moment). Course stability can be significantly reduced by placing the fixation point towards the back of the model, e.g. at the aft segment. In this case in particular, mounting a guiding slider element is essential for safety and practicality reasons.

Additionally, a set of non-functional requirements influences the final decisions e.g. accessibility, compliance, maintainability, operability, price, quality etcetera.

3-4 Force measurement concepts

This section outlines the used measurement set-up to (eventually) determine the VBM. Due to the demand for a versatile option and the available workforce, the earlier used rigid backbone and two model segments are part of the measurement set-up. Section 2-4 explained that a 2-segment model is suitable for determining this phenomenon accurately when the segmentation is carried out at midship. Below, two potentially feasible options are outlined. (1) Improvement of formerly used set-up consisting of force transducers at the interface of the rigid backbone and the two segments. (2) measurement of strain directly at the backbone when it is kept in one piece or measure at a element connecting two backbone halves.

The inevitable compromise:

As mentioned earlier, the segmented model with rigid backbone concept is advantageous by, inter alia, its versatility. One must realize that *rigid* is only a theoretical notion. All materials deform under load, no matter how small. Force/Moment measurement directly on the 'rigid' backbone is therefore a possible option that should be investigated. Feasibility of measuring directly on the rigid backbone depends on the resolution in which the placed strain gauges can measure bending deformation under the load values. The amount of strain at the carbon fiber backbone was determined (analytically) first to estimate the feasibility.

3-4-1 Force transducers at the segment-backbone interface

In this concept, multiple force transducers connect the backbone and the two ship segments. The VBM is considered to be only dependent on forces acting in the x-z plane. Therefore the used force transducers are oriented to measure the acting vertical and horizontal forces. Per segment, two vertically oriented transducers measure the shear force acting on the backbone. Together with the horizontal load, measured by two horizontally oriented transducers per segment, the vertical bending moment can be determined. Figure 3-8 schematically illustrates the concept. The model is connected to the towing carriage via a roller supported steel pole. The roller support allows heave motion of the model. Pitch motion is possible from the pivot point, directly below the backbone.

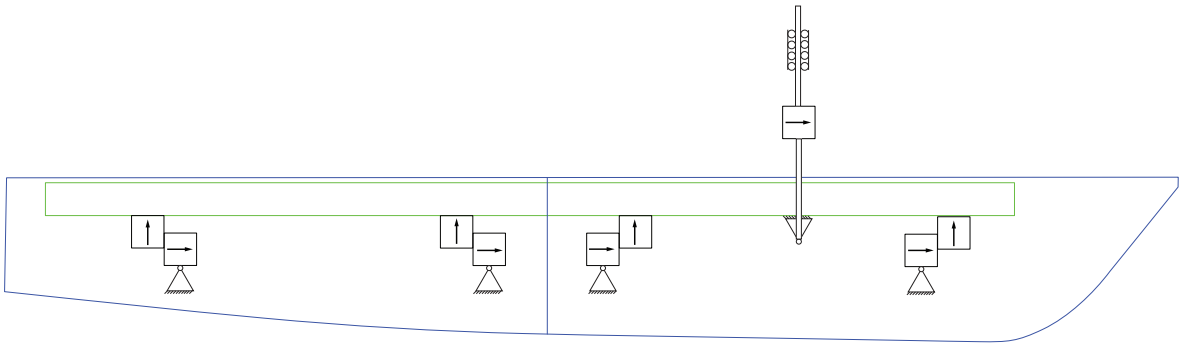

Figure 3-8: Experimental set-up concept – side view.

From statics laws, using a roller support is required to ensure a statically determined system. Due to deformation of the backbone and segment, extremely high forces may be transferred

through the force transducers. Since a rigid backbone and stiff segments are used, the deformation is expected to play a marginal role. During verification potential deformation and the consequences for the force measurement are considered. This makes the concept preferred over a concept involving roller supports. By using two horizontal force transducers, the total amount of horizontal force can be determined. The roller support will always transfer some amount of force due to internal friction in the sliding element. Section 3-1 showed that this is a considerable amount for the prior used support. For the sliding element friction significantly increased when a vertical force or bending moment was transferred through the part.

Furthermore, from the experiments stated in Section 3-1 it is known that hinges are required to ensure veracious distribution of vertical load between the two vertical transducers that connect one segment to the backbone. The force transducers that are typically used for scale model experiments at the Ship Hydromechanics and Structures (SHS) laboratory have proven reliability in force registration, the conducted primary experiments endorse this. The amount of torque that will be transferred through the transducers is expected to be low, influencing the outcomes to a very little extend. Moreover, in-situ assembly calibration/verification can identify this influence quantitatively.

3-4-2 Strain gauges mounted to the backbone

By placing strain gauges directly on the backbone or on an element connecting two backbone halves the bending moment at mid-ship can be determined. The formerly used backbone is constructed out of carbon fibers which are placed under an angle in creating a diamond shaped pattern. Due to the fiber material and production process, the beam's stiffness to weight ratio is extraordinarily high. The accuracy of the strain gauges is dependent on the amount of strain at the location, hence the high stiffness can lead to inaccurate results. To overcome this potential event, a material with lower stiffness (e.g. aluminum) could be placed in between two stiff beam halves. The gauges are then placed on this material.

The curvature (and hence strain) under transverse load was determined analytically before. Appendix B discusses the calculation in detail. As a result of the assumptions, the expected strain at midship is expected to be in the order of 2.2 $\mu\varepsilon$ (i.e. 0.025 ‰). This is on the lower boundary of the measurement bandwidth of strain gauges. To enhance the measurement resolution, two strain gauges are placed on the top and two on the bottom of the beam. This set-up measures the positive strain and negative strain at the top or bottom (or vice versa) via a full Wheatstone bridge configuration. When it appears that the expected accuracy is insufficient, the concept containing the lower stiffness connecting element is presumably a better solution. Then again, a lower stiffness lowers the natural frequencies and may potentially result in resonance under (scaled) wave frequency excitation.

Strain gauge type and placement

The selected Strain Gauges (SGs) have a linear measurement grid. The used gauges are typically used for force measurements. If placed as described in the previous subsection, they can be used to measure a bending moment. The SR-4 type, manufactured by Vishay (Figure 3-9) has a nominal resistance of 120 ohms and is available in various geometries. The measuring grid consists of constantan; the material of the measuring grid carrier is polyimide.

The selected measuring grid length depends on the aim of measurement, since the result of a measurement with strain gauges will be determined as the average of strains. In general, measuring grid lengths of 3 to 6 mm represent a good solution. A long strain gauge will bridge the inhomogeneity of the workpiece and return the strain underneath the measuring grid as the measurement result. The selected measurement grid is 6 mm, which is recommended for an inhomogeneous material such as woven carbon fiber.

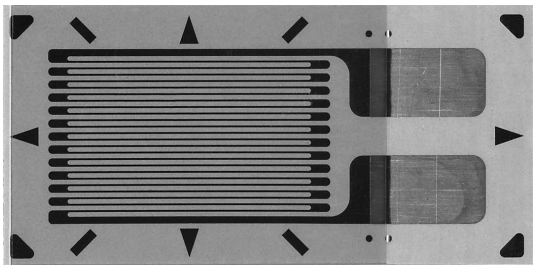

(a) Photocopy.

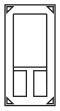

(b) Actual size.

Figure 3-9: Vishay general purpose strain gauge.

The selection of the resistance depends on the constraints of the measurement task. Strain gauges of 120 ohms are relatively insensitive to fluctuations in the insulation resistance; for example, due to the effects of moisture. The advantage of higher-impedance strain gauges is that they produce less specific heat due to the lower measuring current. In addition, they are less sensitive to resistances in the connecting cables to the measuring amplifier. There is also a disadvantage that high- impedance strain gauges may be more sensitive if noise pulses are received.

Four SR-4 SGs are placed directly on the backbone. The location of interest is at midship. To maximize the potential amount of strain, they are placed on the outer fibers of the top and bottom of the beam. The full Wheatstone bridge configuration consists of two gauges placed on the top and two placed on the bottom. After installation, the configuration is extensively calibrated (Refer to Section 4-3) before the backbone is assembled in the final experimental set-up.

3-5 Ship mounting

Since the model is not self propelled and experiments with forward speeds are planned to be conducted, a proper towing location must be considered. Primarily, the location should have sufficient agreement with the location and direction of thrust of the full size ship. For validation of the FASTSHIP code different assumptions should be made. In the routine, the equations assume that the thrust acts horizontally in the CG. Additionally the routine neglects the vertical frictional component and its contribution to the pitch moment and it neglects wave making and spray rails resistance and whisker spray drag.

For a two-segment model with a backbone connecting the segments and providing the structural strength, three principal options can be distinguished. The model can be towed at the:

1. backbone
2. front segment
3. aft segment

Despite the fact that a consequence of changing the towing location is interesting to investigate, this is not included in the research simply because at the time of construction and assembly no workforce was available to include multiple mounting points.

3-6 Data acquisition

The experimental set-up consists of a combination of concepts mentioned above. The altered set-up will consist of a carbon fiber backbone that connects the two ship segments via 8 force transducers in total. Four SGs are placed on the backbone at the potion of the hull cut.

An essential part of any measurement set-up is to make proper use of data acquisition equipment. This includes sensors, signal conditioning circuitry and A/D conversion. At this section the emphasis is on the sensors and consequently the input signals. Three types of quantities are measured: forces, ship motions and the local water level.

Forces

The majority of sensors is intended for force measurement. A total of 10 force/moment measurement sensors are placed in the set-up to compare the internal force measurement concepts (Section 3-4). The sensors can be categorized as strain gauges placed directly and strain gauges placed on a specially fabricated force transducer (also referred to as 'temple' by the Delft University of Technology (TU Delft) personnel). The signals are captured at a sampling rate of 100 Hz.

Input signals: 10.
Sampling rate: 1000 Hz.

Ship motions and accelerations

The motion sensor that is used for towing tank experiments at TU Delft is named Certus. The sensor consists of a 120 by 120 mm plate, mounted on the model and a stationary camera that is mounted on the towing carriage. Processing of the images provided by the camera, results in an accurate decomposition of the ship movements. All six Degrees of Freedom (DOF)'s output is available, however in the current experiments surge, yaw, sway and roll are valued (practically) zero.

Additionally, two accelerometers are placed on the ship. One near the CG and one at the ship's bow. The number of input signals per sensor is 1. Three 3-axis accelerometers measure the accelerations at the backbone in three places. The total of signals is 11.

The forward speed (and acceleration) is determined from the change in carriage position. One signal is logged.

Input signals: 18.
Sampling rate: 100 Hz for Certus and towing carriage velocity, 1000 Hz for the accelerometers.

Wave height

The wave height at position of the CG is measured using a wave rake. This sensor consists of two metallic wires that transmit electric current. With an increasing water level, a larger part of the wires will submerge and as a consequence, the circuit's total electric resistance will decrease. This change in resistance eventually provides the in situ wave height. Unlike the other sensors, the wave rake requires calibration prior to each testing day.

Input signals: 1.
Sampling rate: 100 Hz.

Signal overview

Summing the amount of signals discussed in the previous subsections results in a total of 22 inputs. The signals are outlined in Table 3-2.

Table 3-2: Sensors and input signals.

#	Type	Input	Symbol	Unit	Sampling rate $[Hz]$
1	Force transducer$_1$	VSF$_1$	F_1	N	1000
2	Force transducer$_2$	HSF$_1$	F_2	N	1000
3	Force transducer$_3$	VSF$_2$	F_3	N	1000
4	Force transducer$_4$	HSF$_2$	F_4	N	1000
5	Force transducer$_5$	VSF$_3$	F_5	N	1000
6	Force transducer$_6$	HSF$_3$	F_6	N	1000
7	Force transducer$_7$	VSF$_4$	F_7	N	1000
8	Force transducer$_8$	HSF$_4$	F_8	N	1000
9	Force transducer$_9$	resistance	F_9	N	1000
10	Strain gauges	VBM	F_{10}	Nm	1000
11	Certus	surge	x	m	100
12	Certus	sway	y	m	100
13	Certus	heave	z	m	100
14	Certus	roll	ϕ	m	100
15	Certus	pitch	θ	m	100
16	Certus	yaw	ψ	m	100
17	Accelerometer$_1$	surge acc.	$\ddot{x}_1$	m/s^2	1000
18	Accelerometer$_1$	sway acc.	$\ddot{y}_1$	m/s^2	1000
19	Accelerometer$_1$	heave acc.	$\ddot{z}_1$	m/s^2	1000
20	Accelerometer$_2$	surge acc.	$\ddot{x}_2$	m/s^2	1000
21	Accelerometer$_2$	sway acc.	$\ddot{y}_2$	m/s^2	1000
22	Accelerometer$_2$	heave acc.	$\ddot{z}_2$	m/s^2	1000
23	Accelerometer$_3$	surge acc.	$\ddot{x}_3$	m/s^2	1000
24	Accelerometer$_3$	sway acc.	$\ddot{y}_3$	m/s^2	1000
25	Accelerometer$_3$	heave acc.	$\ddot{z}_3$	m/s^2	1000
26	Accelerometer$_4$	heave acc.	$\ddot{z}_4$	m/s^2	1000
27	Accelerometer$_5$	heave acc.	$\ddot{z}_5$	m/s^2	1000
28	Wave rake	wave height	ζ_a	m	100
29	Towing carriage	fw. velocity	$\dot{x}$	m/s	100

Chapter 4

Experiment Preparation

Chapter 4 discusses the operational steps that must be carried out before commencing the towing tank experiments. Part of this preparation is composing the test program, which is the set of experiments on *run-level*. The test program is composed against the background to systematically increase the amount of disturbances (i.e. influencing factors) to eventually validate the experimental set-up such that the internal forces and moment can be determined accurately. Simultaneously, as always, various boundary conditions apply. The applicable boundary conditions are explained first.

4-1 Boundary conditions

During the experiments the testing equipment (principally the towing carriage and wave maker) and available testing time are the governing limiting factors. To start with the time aspect: there is time for approximately 10 days of testing in Towing tank 1. On average a maximum of 20 runs can be carried out during one testing day. This totals the number of runs to 200. If one in ten runs is repeated to review reliability of measurement values, the number of available runs is approximately 180.

Towing carriage and wave maker

The towing carriage is able to accelerate at a maximum of 8 m/s^2. The dimensions of the towing tank are 142 x 4.2 x 2.5 m (L x W x D). The effective tank length is 110 m. When considering constant speed, the effective measurement length is typically between 75 and 100 m. The maximum velocity when measuring in a wave spectrum is 4 m/s, yielding 22 seconds of measurement time. Higher velocities yield a shorter measurement time and is therefore rarely applied. Measuring in a wave spectrum requires minimally 600 s measurement time. For the carriage velocity of 4 m/s, this results in a minimum of 28 runs. For regular and calm water tests, a maximum towing velocity of 7 m/s applies. In the case of captive tests, the experimental set-up must be changed. This change requires extra time, however from

previous studies it is expected that the amount of extra time needed will not result in a significant time loss.

The wave maker is of a so called flap-type. The flap can swivel at two positions, to be able to accurately produce both long and short waves. The transfer function from input voltage to wave amplitude is nonlinear, a software routine is available to generate the required input voltages from the desired wave heights. The wave making device is able to produce waves having a 5 cm amplitude from approximately 0.9 rad/s to 6.5 rad/s. The maximum is derived from the maximum wave steepness per frequency and the maximum force the wave maker can exert.

Full scale and numerical code parameters

As stated before, the ship of interest is the Damen Stan Patrol 4207, a derivative of the Enlarged Ship Concept (ESC). The ship has a maximum working velocity of approximately 30 kn. (eq: 55 km/h or 15 m/s). This velocity corresponds to a volumetric Froude number of 2.0. For the 1:20 scale model for $Fn_\nabla = 2.0 \;\widehat{=}\; V_s = 3.5\ m/s$. As a result, (using Froude scaling) the velocity range 0 - 3.5 m/s is the range that matches the full scale values.

The goal to validate the FASTSHIP routine that calculates the internal loads is not part of the current research's scope, nonetheless the program's working range is considered as well. It is known that regarding motion response FASTSHIP performs best at $1.5 \leq Fn_\nabla \leq 3.0$. At model scale, this corresponds to a velocity range of $V_s = 2.6$ - 5.2 m/s.

4-2 Test program

Variables that can be adjusted throughout the test program are listed below. Since varying all parameters will result in a exceedingly high number of required runs, a selection of varying parameters must be made.

Amendable parameters:

1. Carriage
   (a) Velocity
   (b) Carriage - model connection point/type
2. Model properties
   (a) Initial trim angle
   (b) Initial displacement
   (c) Hull roughness
3. Wave maker
   (a) Wave frequency
   (b) Wave height
   (c) (Resulting) wave steepness

The principal goal of the current research is to validate the experimental set-up. This makes testing in irregular waves of lower priority. If the set-up proves valid in regular waves, in all probability the set-up measurement results will remain valid in irregular waves.

Note on the hull roughness parameter.
The status quo at the start of the research was that amount of influence of the horizontal force component (i.e. resistance components) on the vertical bending moment is uncertain. When the horizontal component proves to be of (great) influence on the Vertical Bending Moment (VBM) at midship, the validation of numerical routines that calculate the VBM by using strip theory is to say the least debatable.

By using data of previous ESC model tests and the ITTC-1957 curve, an estimate of the of frictional resistance was made. Depending on the forward speed (1-5 m/s) the share of skin friction in the total resistance is 23-37 percent. The fact that this share is considerable high makes it interesting to alter the model's hull roughness. Doubling the amount of skin friction would mean an additional horizontal resistance of roughly 15 percent. This change is clearly measurable and therefore potentially, the magnitude of the VBM changes significantly as well. NB: Experiments as part of this research proved that the resistance was practically doubled by increasing the skin friction. This increase is conducted to magnify the potential effect of friction, i.e. the horizontal force component on the VBM.

The following subsections demonstrate the test program in blocks having increasing complexity of disturbing factors. The experiments vary from static dry testing to quasi static calm water tests to dynamic behavior as a result of encountering waves.

4-2-1 Dry testing

The dry testing experiments' goal is to calibrate the force transducers and verify correctness of the experimental set-up after assembly. More information can be found in Section 4-3. The set-up is similar to the set-up discussed in Section 3-1 with half of the backbone attached to a steel table.

4-2-2 Calm water

Calm water tests will start with the ship without any adjustments to trim, displacement or hull roughness. An advantage of calm water tests is that the measurements can be considered as quasi static. Dynamics are negligible shortly after the constant end speed is reached. The measurements can eventually be used to derive the added mass and cross flow drag values for potential flow numerical code.

From the boundary conditions and requirements, the following towing end speeds are derived:

Table 4-1: Rounded calm water velocities.

V_m	$[m/s]$	0.5	1.5	2.5	3.5	3.8	4.5	5.0	5.5
Fn_∇	$[-]$	0.3	0.9	1.5	2.0	2.2	2.6	2.9	3.2
Fn_L	$[-]$	0.1	0.3	0.6	0.8	0.9	1.0	1.1	1.2

The measurements at 3.75 and 5.0 m/s are carried out to allow a direct comparison with results of van Hoeve's results.

4-2-3 Regular head waves

In regular head waves, the ship was tested at three velocities and two wave steepness ratios, in a range of wave frequencies. The frequencies range from 3.58 to 6.71 rad/s on model scale. Table 4-2 shows the wave parameters. Inherent to the use of a constant steepness ratio, is a variable wave amplitude over the frequency range. The amplitude for 1/60 steepness waves is displayed in the rightmost column.

With the water depth of 2.22 m, waves of all frequencies can be considered as propagating deep water waves. The motion response of the free moving model to regular waves can be used to generate the Response Amplitude Operators (RAOs) considering linear wave theory.

The total number of runs in regular head waves is 40 (8 frequencies times 5 conditions). Due to a high amount of water entering the hull at 3 m/s and steepness ratio 1/30, the 1/30 steepness series for 4.5 m/s was canceled.

Table 4-2: Regular head waves parameters.

ω_s $[rad/s]$	ω_m $[rad/s]$	$\omega(L/g)^{1/2}$ $[-]$	T_m $[s]$	λ/L $[-]$	ζ_a *at* $\kappa = 1/60$ $[m \cdot 10^{-2}]$
0.80	3.58	1.61	1.76	2.43	8.0
0.90	4.02	1.81	1.56	1.93	6.3
1.00	4.47	2.01	1.40	1.56	5.1
1.10	4.92	2.21	1.28	1.29	4.2
1.20	5.37	2.41	1.17	1.08	3.6
1.30	5.81	2.61	1.08	0.92	3.0
1.40	6.26	2.81	1.00	0.79	2.6
1.50	6.71	3.01	0.94	0.69	2.3

4-2-4 Irregular head waves

The ship advancing in regular waves is sufficient to validate the measurement set-up. However, irregular waves are required to measure the response and express this in terms of extremes. Furthermore in (high speed) operations only irregular waves are encountered. Since slamming events are continuously occurring during these operations, the wave spectrum is selected such that the expected number of slamming events is at the approximate maximum (under the occurring circumstances such as wave height and ship velocity). Carrying out experiments in irregular waves involves a relatively large amount of required runs, therefore only one combination of towing speed and sea state is considered.

The forward speed is 3 m/s, corresponding to $\approx$ 25 $kts.$ full scale. This is just below the maximum operating speed of the Stan Patrol. The set statistical minimum required run time in irregular waves is 600 s. at model scale. A run of 3 m/s yields about 30 s. of measurement time, therefore a minimum amount of 20 runs is required.

Table 4-3: Irregular wave parameters.

V_m $[m/s]$	$Runs$ $[-]$	$T_{tot,m}$ $[s]$	$T_{tot,s}$ $[s]$	$H_{1/3,s}$ $[s]$	$T_{p,s}$ $[s]$	$T_{2,s}$ $[s]$	γ [-]
3.0	20	600	2700	1.0	6.3	4.9	3.3

The chosen peak period is 6.3 s, resulting in a non-dimensional peak frequency of $\omega\sqrt{L/g} = 2.1$. De Jong (2011) [43] showed that at the ESC[1] propagating at 25 kts., a peak in vertical acceleration at the bow is expected. It is almost certainly that this peak is present due to slamming events. The encounter period at this speed is $T_e(25kts.) = 2.72\ s$. A selection of parameters can be found in Table 4-3.

Although the irregular head wave experiments are carried out and recorded, this data is not processed as part of this study. This decision is based on the fact that validation of the experimental set-up is not dependent on the irregular wave experiments. The writer advises to include these recordings in potential further research (intended to validate numerical code). Special consideration should be dedicated at investigating the response during slamming events.

4-3 Force sensors' calibration and validation

The calibration process compares the known against the unknown. Regarding calibration of the force transducers, the known is a piece of weight and the unknown is the change of voltage. This change is a result of a change of resistance at the four strain gauges. The Strain Gauges (SGs) are placed connected via a Wheatstone bridge configuration. The steel block and strain gauges form the force transducer. A true calibration usually contains both *as found* and *as left* data. The backbone was calibrated according to this method. The as left calibration resulted in a different calibration factor, however this factor was unchanged. The process and results are described further below. Subsection 4-3-2 describes the validation of the force transducers when (fully) assembled in the model.

4-3-1 Calibration process

The total of 9 force transducers and 1 set of strain gauges directly placed on the backbone was calibrated prior to the set-up's assembly. The calibration of the force transducers was carried out according to the standard procedure used in the towing tank facility. Step wise, an increasing amount of mass was hung vertically on the force transducer up to the transducer's set measuring range. Subsequently, the mass was decreased to zero to check for any presence of hysteresis. After changing the orientation of the transducer, this procedure was repeated. The change in voltage at input of the the A/D converter as a function of the acting force is

[1]The water line length of the ESC used in De Jong's study is approx. 10 m larger than water line of the commercial version. It is assumed that the response (as function of the non-dimensional wave frequency) is approx. equal for the commercial ship's model.

Table 4-4: Calibration values of force and moment sensors.

#	Position	Direction	Range [N], [Nm]*	Sensitivity [N/V], [Nm/V]*	Std. Dev. %
1	Front, front	z	± 100	8.79	0.03
2	Front, front	x	± 50	4.13	1.30
3	Front, mid	z	± 100	8.64	0.11
4	Front, mid	x	± 50	4.18	0.14
5	Rear, mid	z	± 100	8.61	0.19
6	Rear, mid	x	± 50	4.09	0.05
7	Rear, rear	z	± 100	9.39	0.24
8	Rear, rear	x	± 50	4.25	0.10
9	Towing rod	x	± 200	9.44	0.28
10*	Backbone	x-z plane	$\gg \pm 100$	16.5	2.24 - 12.1

checked for linearity. All calibrations showed linear behavior of the system and no noteworthy hysteresis. The outcomes (expressed in N/V and Nm/V) will be further used to indicate the acting forces on the transducers/strain gauges.

The strain gauges placed on the backbone were also calibrated using the 'double-pyramid' procedure. The backbone was fixed to a steel table, and vertical mass was hung to the backbone at the positions of future connection to the segment. The results show that hysteresis of several percents is present after unloading. Apart from this fact, the results were satisfying. Afloat, the backbone will not be fully unloaded, therefore this effect is expected to minimize. The configuration could measure the bending moment directly and on a linear scale (which is advantageous over a non linear scale).

A summary of the calibration values per strain is shown in Table 4-4. The outlined direction refers to the measurement direction expressed in terms of the shipbound axis system (earthbound for # 9). The range indicates the maximum allowable force that may act on the transducer as set by the Ship Hydromechanics and Structures (SHS) staff. A too small range will eventually lead to nonlinear material behavior of the sensor, ultimately causing plastic deformation or rupture. A too large range will lower the actual measurement resolution of the sensor. Ultimately the (always existing) noise will disrupt the signal significantly, decreasing the reliability of the measurement. The rightmost column indicates the standard deviation that is calculated from the accuracy (i.e. linearity) of the sensor.

4-3-2 Validation

In the current section, a process of confirming that the instruments have been installed correctly is outlined. Correct placement implies effective operation and error-less performance. The validation was performed in two stages. At the first stage, the set-up as described in Section 3-1 is assembled to directly compare the previous- with the new-configuration. Table 4-5 shows the minimum, maximum and average deviations per load type. The results show deviations of well below 1 N, resulting in relative deviations of a few tenths of percents.

Part two of the validation was conducted after fully assembling the two halves. For pragmatic reasons, the validation was carried out in calm water. A set of two 2 kg weights was shifted

Table 4-5: Minimum, maximum and average measurement deviations.

Load		ΔF_v	$\Delta F_v/F_v$	ΔF_h	$\Delta F_h/F_h$	$\Delta F_h/100N$
		[N]	%	[N]	%	%
Symmetric	min	-0.24	-0.2	-0.64	0.1 ($/F_v$)	0.0
	max	0.12	0.3	0.03	0.4 ($/F_v$)	0.6
	avg	-0.03	0.0	-0.23	0.3 ($/F_v$)	0.3
Asymmetric	min	-0.08	-0.1	-0.46	-0.1 ($/F_v$)	-0.1
	max	0.13	0.3	0.05	1.2 ($/F_v$)	0.5
	avg	0.06	0.2	-0.12	0.4 ($/F_v$)	0.1
Horizontal	min	-0.02	-	-0.78	1.9	0.0
	max	0.82	-	0.15	2.6	0.8
	avg	0.35	-	-0.03	2.3	0.1
Combined	min	-0.06	0.2	-0.20	-0.7	-0.2
	max	1.67	2.1	0.28	0.8	0.3
	avg	0.68	1.2	0.10	0.4	0.1

in the two segments. During one series, the weights were symmetrically shifted w.r.t. the Longitudinal Center of Gravity (LCG) (11, 39 and 60 cm distanced from the LCG. At the second series, the weights were symmetrically distanced from midship. The first distance was considered as zero measurement. The change in mass distribution results in a change of bending moment (measured at midship).

The measured values could not be directly compared with a moment due to the change in arm times the force since the change hydrostatic pressure was not known, partly because a potential change in trim was not recorded. For that, the change in bending moment is compared for the directly and indirectly measured values. All indirectly measured bending moment values were approx. 3 % higher than the directly measured values. The discrepancy is sufficiently small to consider the assembly of the two halves successful.

4-4 Auxiliary sensors' calibration

Besides the force measurement calibration and verification, auxiliary sensors should be calibrated prior testing. The sensors are listed below.

- Certus
- Waveheight meter
- Accelerometers (5 pc.)
- Wave maker

Certus

The Optotrak Certus system is a system able to deliver accurate motion capture out-of-the-box. The optical sensors are calibrated by the manufacturer. Frequently, the system is checked by the personnel.

Waverake

The waverake is used to determine the local water height. The rake consists of two wires over which a voltage is set. A change in electrical resistance. Any attachment to the wire will result in a change in the sensitivity, therefore the system must be calibrated each day to increase reliability of the results. Calibration was carried out by stepwise raising and submerging the wires into the (calm) water and listing the associated voltages.

Accelerometers

The accelerometers were calibrated by shifting the orientation and listing the change in voltage. By shifting the orientation from -z to z, a change of 2 g ($\approx 2 \cdot 9.81 m/s^2$) is accomplished.

Wave maker

Using an input signal [V], the flap-type wave maker delivers a wave as output [mm]. The transfer function from voltage to wave height is dependent on the water height. Using an interpolation curve, the required voltages for the desired wave heights are generated. These heights were compared to the measured values at the calibrated wave rake and proved equal.

4-5 Model mass and inertial properties

Data analysis with the purpose of validation requires knowledge of several physical properties of the model. Most important are the mass, position of the center of gravity and the rotational inertia. Since only motions in the x-z plane are considered (and present), the LCG, Vertical Center of Gravity (VCG) and rotational inertia around the y-axis I_{yy} are relevant. The values are outlined in Table 4-6. The LCG value is defined as distance measured from the model's transom. The VCG value is measured from the model's keel. The values are fairly equal to the former model, exact reproduction was not of high priority, since the measurement set-up must prove correct for arbitrary mass properties.

Table 4-6: Model mass and inertial properties.

	Mass [kg]	LCG [m]	VCG [m]	I_{yy} [kgm^2]	k_{yy} [m]
Unballasted	17.94	0.85	0.15	7.42	0.64
Fully ballasted	27.48	0.85	0.13	9.03	0.58
Former model	27.22	0.84	0.12	8.24	0.55

Chapter 5

Results

Chapter 5 presents the results from model tests. The results are further discussed in the subsequent chapter. The experiments are increasing in complexity resulting from Calm water experiments are carried out to check , hereafter regular waves results are presented. Although irregular head wave experiments were conducted, the processing and an outline of the results is not included in the thesis.

5-1 Calm water

The conditions of the measurements can be considered quasi static. I.e. no significant accelerations are present. From Newton's second law the sum for forces in any direction should be zero. The measurement values should be interpreted as the additional loads that are induced by towing the model. This is a result of the deduction of values that are obtained from a a zero measurement. This measurement is carried out in calm water for 60 seconds.

Two series of tests are carried out in calm water. The first series consists of a number of constant forward velocities. The second series consists of equal velocity conditions, however the hull surface's roughness was increased.

5-1-1 Ship model resistance

The model's increase in resistance can be seen in Figure 5-1. The smooth surface resistance curve in particular is slightly s-shaped. In between Fn 1.5 and 2.0, the increase in resistance reduces, to then further increase. By roughening the hull surface, the resistance increases roughly with a factor two. In the subsequent subsections, change in resistance's influence on the midship Vertical Bending Moment (VBM) is outlined.

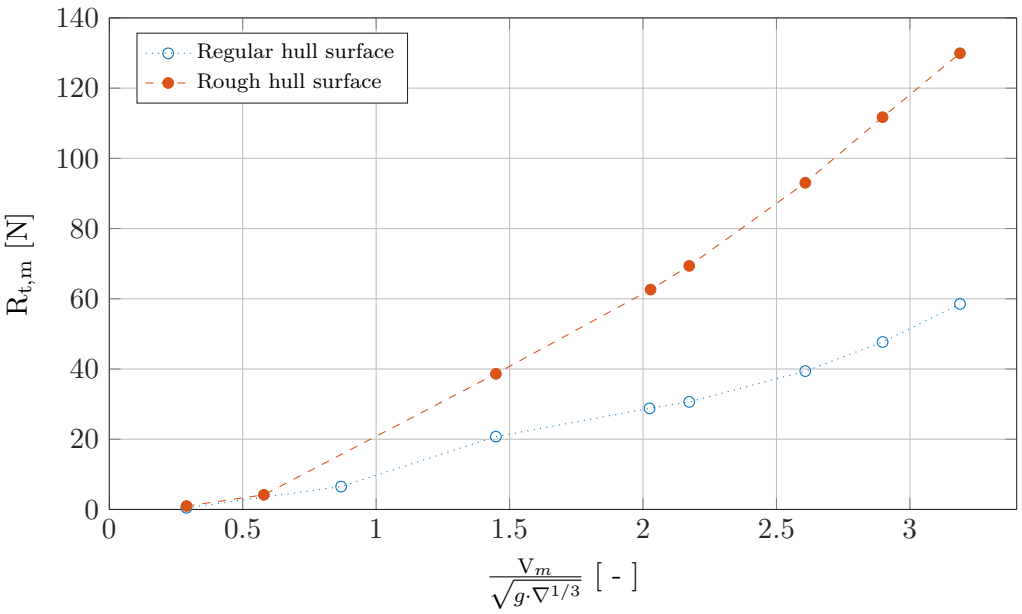

Figure 5-1: Model resistance: regular and rough hull.

Sum of horizontal forces

The resistance is compared with the (earthbound corrected) value that is measured by the eight horizontal and vertical force transducers. Additionally, a change in trim angle requires a correction for the zero measurements. Weight of the construction[1] above the vertical transducers will be measured by the horizontal force transducers. This phenomenon requires a correction by adding part of the weight to the horizontal transducers and subtracting it from the vertical transducers. Please refer to **Appendix C-2** for the used equations.

The resulting sum of earthbound horizontal forces is close to zero for all measurements, summarizing: $dF_{min} = -0.1$ N, $dF_{max} = 1.0$ N, $dF_{med} = 0.6$ N.

Sum of vertical forces

Equally, the sum of vertical forces must be zero, the change in hydrostatic force and hydrodynamic forces are in equilibrium with the gravitational force. The model is free in heave as a result of the linear sliding construction. The measurement results show that a portion of the force is leaking away at the guidance pole. Isolated measurements show that a radial force (and resulting bending moment) causes a friction of $\pm 3\%$ of the exerted force. For the vertical sum of forces is resistance is added to the equation. The friction effect shows smaller for the smooth hull's lower resistance, however a linear term for the entire range is used. Resulting sum of forces for the regular hull: $dF_{min} = -0.1$ N, $dF_{max} = 0.4$ N, $dF_{med} = -0.1$ N and rough hull: $dF_{min} = 0.0$ N, $dF_{max} = 2.6$ N, $dF_{med} = 1.3$ N.

[1] outfitted backbone, force transducer measuring resistance, guidance pole etc.

5-1-2 Ship model vertical bending moment

The model's VBM was determined via three options to compare the results. The directly measured bending moment is shown in blue colored O's in Figure 5-2. The red dots and purple diamonds show the indirectly measured VBMs. These are constructed from the individually registered forces, outlined in Appendix C-2. The VSF derivative line constructs the moment merely from the vertically registered forces. The plots show that the directly measured bending moment is generally slightly lower than the indirectly measured moment. Overall, the three methods show good agreement.

For all cases, the added bending moment derivative shows a jump at $\mathrm{Fn}_\nabla \approx 2.0$. At this velocity, the hydrodynamic lift causes the model to start planing. The CG rises up to 7 mm with respect to the zero measurement position. Between $\mathrm{Fn}_\nabla = [1.5 - 3.2]$, the pitch angle remains fairly constant at -2.2 °.

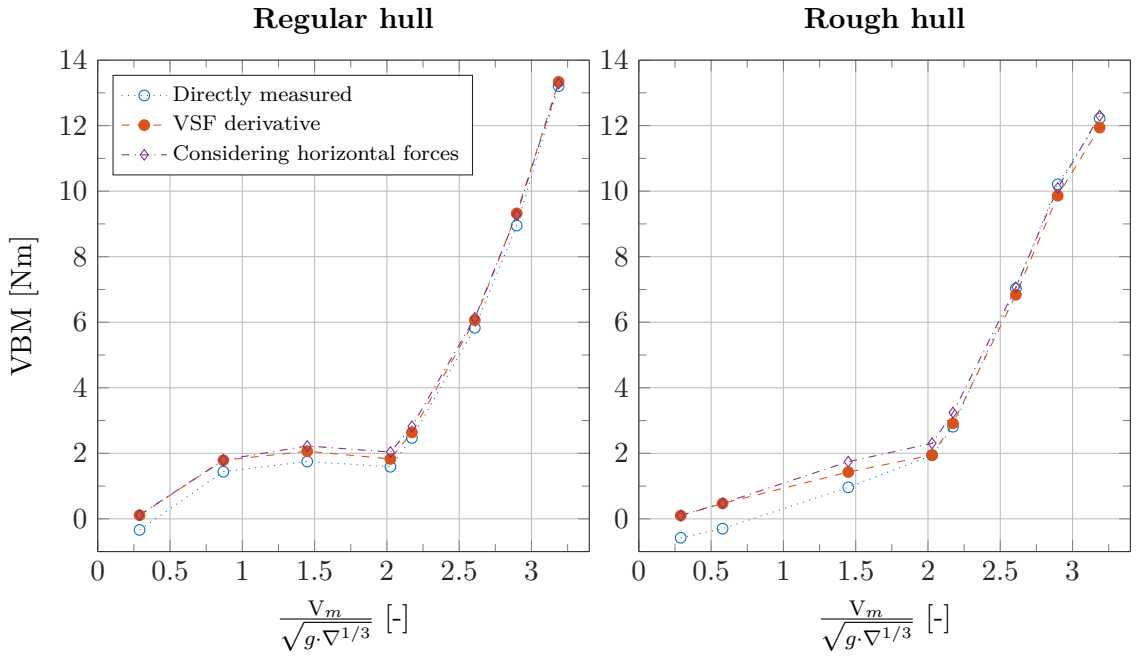

Figure 5-2: Model added VBM: regular and rough hull.

Another remarkable determination can be seen from the comparison of the left and right part of Figure 5-2 is that the added resistance, which increased the total resistance by a factor two, did not result in a significant increase in measured vertical bending moment. In fact, at the majority of the runs, the regular hull has lower added VBM values. This can be seen from Figure 5-3. Here, the determined bending moments considering the resistance component are plotted in the same graph for both the direct and indirect method including horizontal forces. The errorbars show the 95% confidence levels for each measurement. Calculation of these bounds is outlined in Appendix D. The bars directly show that the indirect method provides more accurate results despite the larger amount of sensors that is used to calculate it.

This phenomenon also exists for the directly measured- and VBM constructed from the vertically acting forces. The resistance component has little or no influence on the bending moment acting on the carbon fiber backbone.

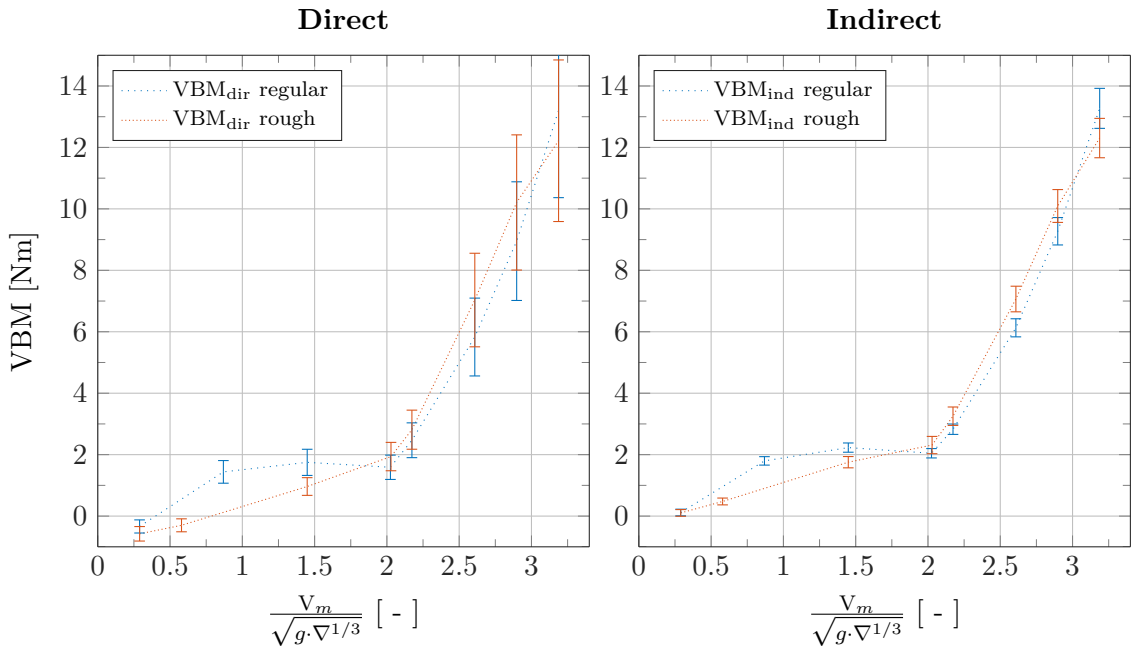

Figure 5-3: Regular and rough hull VBM values inc. confidence bounds.

5-1-3 VSF and VBM along the backbone

The bending moment and shear force was determined as function of forward velocity and x-coordinate. The presented values are derived from the regular hull run series' measurements. The vertical force balance was calculated in an earthbound axes system. The vertical shear force was determined in the shipbound axes system. As a result, the sum of forces for the shipbound system is different. Figure 5-4 shows the shear force over the length of the backbone. The lines show a shift at the four force transducer positions and the position of the towing arm. As mentioned earlier, a linear correlation between the exerted towing force and the friction in the guidance is assumed. The black dots at the position of the foremost force transducer show the remaining error. From the boundary conditions theoretically all end values must be zero.

The confidence intervals are drawn for the end value at 2.5 and 5.0 m/s. The zero shear force is located in this interval for practically all velocities.

Zero values at the boundaries is valid for the bending moment as well. Other than the shear force diagram, moment diagram lines are constructed from the boundaries to midship. Instead of checking the boundary conditions, the values and their derivatives at midship must be equal for both parts. The left graph of Figure 5-5 shows the position dependent VBM for $Fn_\nabla < 2$, the right graph shows the additional bending moment for velocities corresponding to $Fn_\nabla > 2$. The steepness of the line is equal to the local shear force. The vertical jumps are a result of the horizontal forces that are initiated into the backbone.
The lower velocities result in larger discrepancies in the calculations from front to back and from back to front. The derivative's are fairly equal, however the end values for especially 1.5 and 2.5 m/s result in a relatively large jump at midship. For the higher velocities the graphs show a better fit.

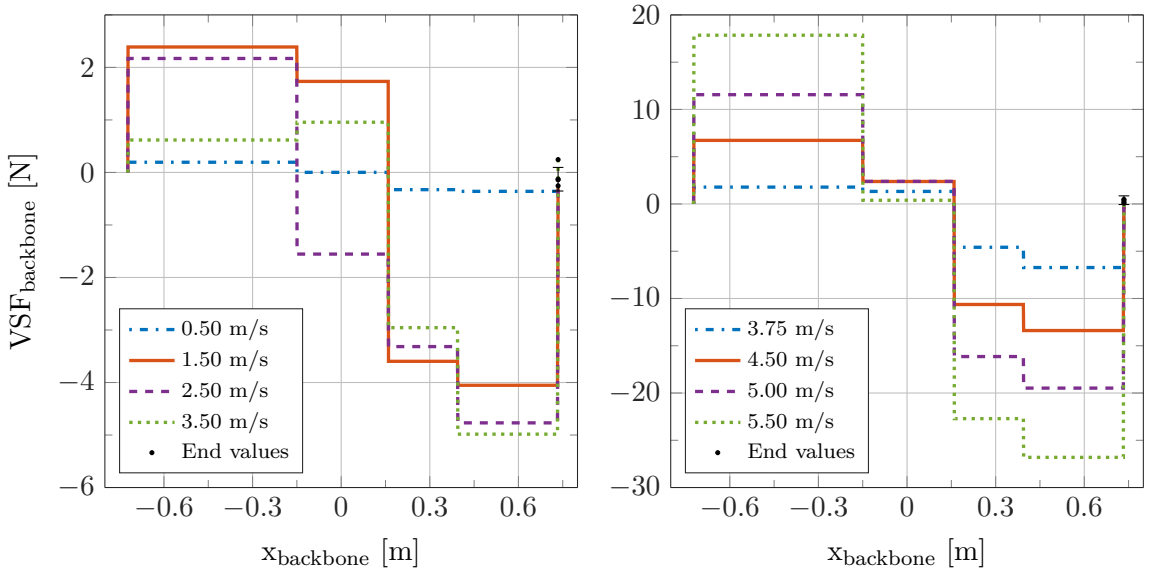

Figure 5-4: VSF along the backbone length. $x = 0$ equals midship

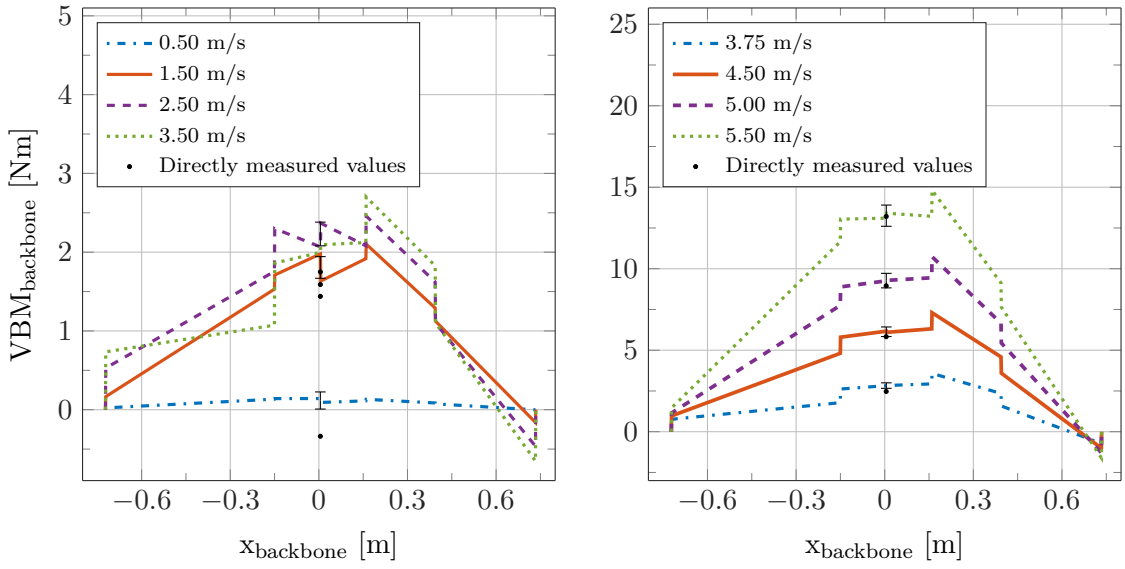

Figure 5-5: VBM along the backbone length. $x = 0$ equals midship.

The midship values can be compared to the directly measured values at midship. The graph shows that the directly measured values are structurally lower than the indirectly measured values. For the higher velocities the directly measured show good agreement with the constructed lines. For lower velocities this agreement is less prominent. For example, the directly measured bending moment at 0.5 m/s is negative while the indirect value is positive.

The indirect values (except 3.5 m/s for viewing purposes) are plotted with their 95% confidence bounds. The error bars of the direct values are larger, as displayed earlier in Figure 5-3. Table 5-1 shows the absolute and relative discrepancies for the two methods. The rightmost column shows the difference of the indirectly measured VBM from front-to-back and from

back-to-front divided by the mean of the two values. Especially high velocity runs show a relatively small discrepancy between the two directions.

Table 5-1: Absolute and relative force and moment discrepancies.

V_m $[m/s]$	ΔF_v $[N]$	$\Delta F_v/VSF_{max}$ $[-]$	$VBM_{ind} - VBM_{dir}$ $[Nm]$	$\Delta VBM_{ind}/VBM_{mean}$ $[-]$
0.5	-0.1	-0.39	0.45	0.42
1.5	-0.3	-0.06	0.37	0.19
2.5	-0.1	-0.03	0.47	-0.14
3.5	0.2	0.05	0.46	-0.04
3.8	0.1	0.01	0.36	-0.00
4.5	0.2	0.01	0.30	0.01
5.0	0.4	0.02	0.32	0.00
5.5	0.5	0.02	0.05	-0.02

5-2 Regular head waves

Regular head waves are generated to include dynamic factors and investigate their influence on the model's motions and forces. At the first subsection, the ship is constrained, mitigating inertial forces. The second part consists of responses at two forward speeds, corresponding to 48 and 72 km/h full scale velocities.

5-2-1 Stationary

Model constrained in heave and pitch

For this series of experiments, the model is constrained such that no ship motions are present. Concomitantly, no inertial forces affect the measurement signals, neither rotating axis systems play part. In addition, due to the constrained backbone, the strain gauges are unable to (accurately) measure the acting vertical bending moment. The midship VBM however can be constructed from the front or rear segment. This bending moment is a result of the acting wave forces: the Froude-Kryflov force and the wave diffraction force. The constrained vessel encountered waves ranging from 3.57 to 6.71 rad/s, having a constant steepness ($\kappa = 2 \cdot \zeta_a/\lambda_{wave}$) of 1/60.

The magnitude of these forces are dependent on the underwater surface of the model. For an arbitrary hull shape, the front and rear segment bending moment time traces will have different maximum values and phases. The left part of Figure 5-6 shows the vertical force amplitudes at the four locations. The prime indicates the fact that the force is plotted dimensionless, equal to $F_a/(\zeta_a \cdot \rho \cdot g \cdot L_{wl} \cdot B_{wl})$.
The trend shows that for increasing wavelengths the force and moment amplitudes increase. This trend is typically valid upto 2 times the waterline length of the ship. Equal trends are visible for the non-dimensional VBM amplitudes.
Here $VBM'_a = VBM_a/(\zeta_a \cdot \rho \cdot g \cdot {L_{wl}}^2 \cdot B_{wl})$.

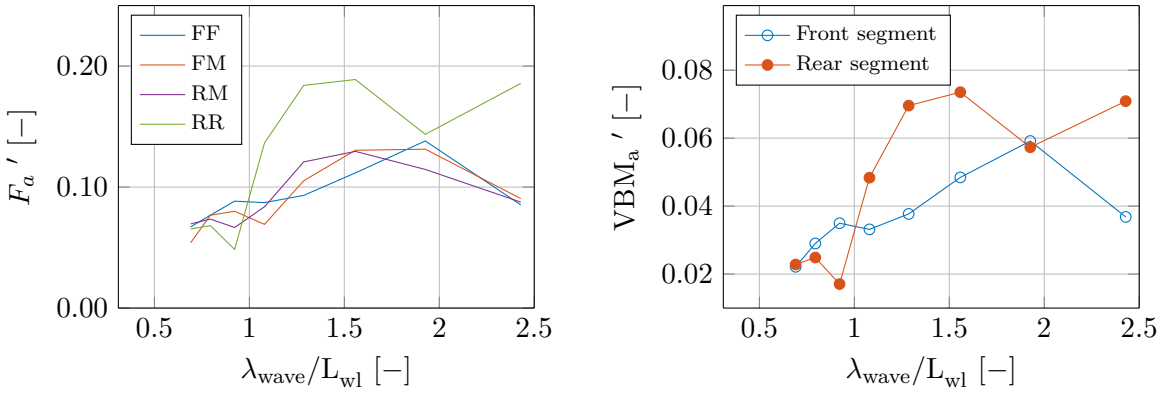

Figure 5-6: Vertical force amplitudes and VBM RAOs, constrained model.

The amplitude of the rear vertical force transducer at the rear segment *RR* is significantly higher than the other amplitudes. The measured force results from the change of hydrostatic pressure of the segment and an extra moment from a local imbalance of the hydrostatic pressure. The measured force is increased due to the moment created from the hanging section part and floating section part.

Apart from this observation, no further or final conclusions are drawn from this series of experiments. This does not imply that the series is unusable for validation of the assembled set-up. The measured force and moment amplitudes can be compared with results obtained from simulation using strip theory or a comparable foundation.

Free moving model

The free moving vessel encountered waves having the same frequencies and steepnesses. Figure 5-7 displays the motion responses. Table 4-2 located in Section 4-2-3 outlines the corresponding environmental parameters such as wavelength over ship waterline length.

At a free moving ship subject to head waves, the RAOs for heave and pitch are typically 1 for low frequencies and converge to zero for higher frequencies. These convergences are not visible in the plots since the tested frequencies are only a part of the spectrum. The trends correspond to the typical trend lines for these conditions. The heave value for the wave frequency 6.71 rad/s is outside this trend. The motions and wave amplitudes are low[2], leading to a relatively high measurement uncertainty. One can ague the reliability of this data point. Indicating accuracy of the measured motion RAOs is not in the current scope of research. Please refer to Chapter 2.3.5 of de Jong (2011) [43] for comparable confidence bounds of regular head wave experiments. The experiments were in similar conditions for a slightly more slender version of the ESC.

[2] $z_a = 1.6\ mm$

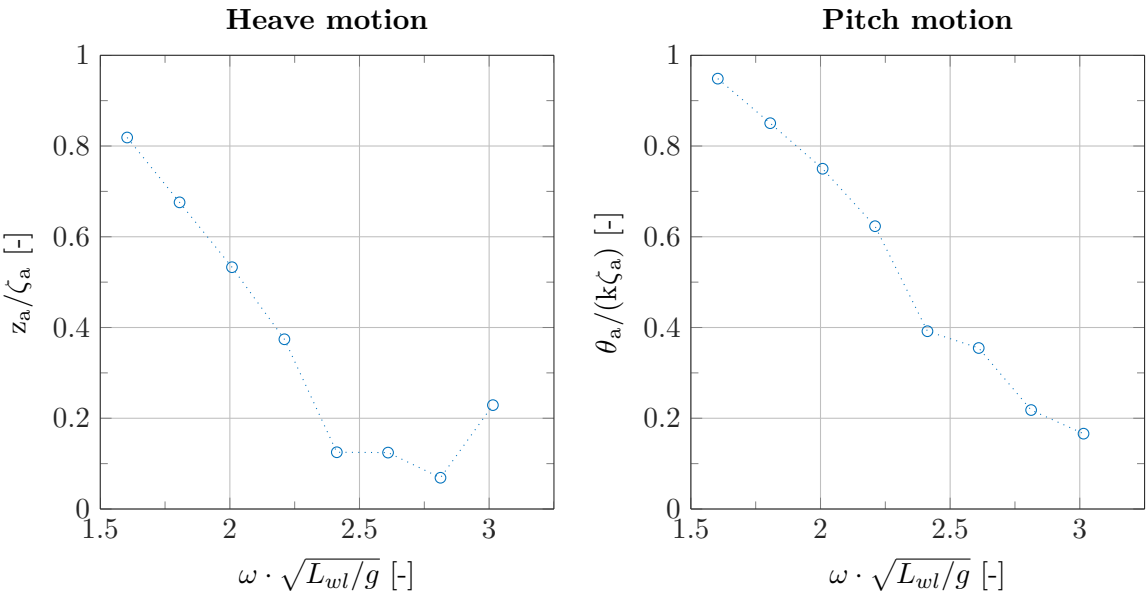

Figure 5-7: RAOs for heave and pitch, $V_m = 0$ m/s.

Vertical bending moment

The vertical bending moment is constructed partly equal to the method described in **Appendix C-2**. This method is expanded by adding correction terms for inertial forces generated by the heave and pitch accelerations. The background and mathematical outline of the correction can be found in **Appendix C-3**.

Figure 5-8 shows the VBM amplitudes of the filtered direct and indirect method, and the corrected indirect method for the free moving moored model. A plot of the bending moment and the moment's the RAO values is included in Appendix A. The F-B lines represents the moments constructed from integrating the forces from the front segment to the back segment, whereas the B-F lines are the result of integration in the opposite direction. The lines show the amplitude as found from a sine fit of the excitation frequency, i.e. the wave encounter frequency.

The uncorrected values are visualized by the striped lines. Especially the resulting bending moment generated from front segment is overvalued when compared to the directly measured VBM. The result of this correction is shown in Figure 5-11. The time-traces show digitally filtered data, the signals contain frequencies up to 25 Hz. It can be seen that higher order effects are present in the signals. In the chapter's last section, special attention is payed to this phenomenon.

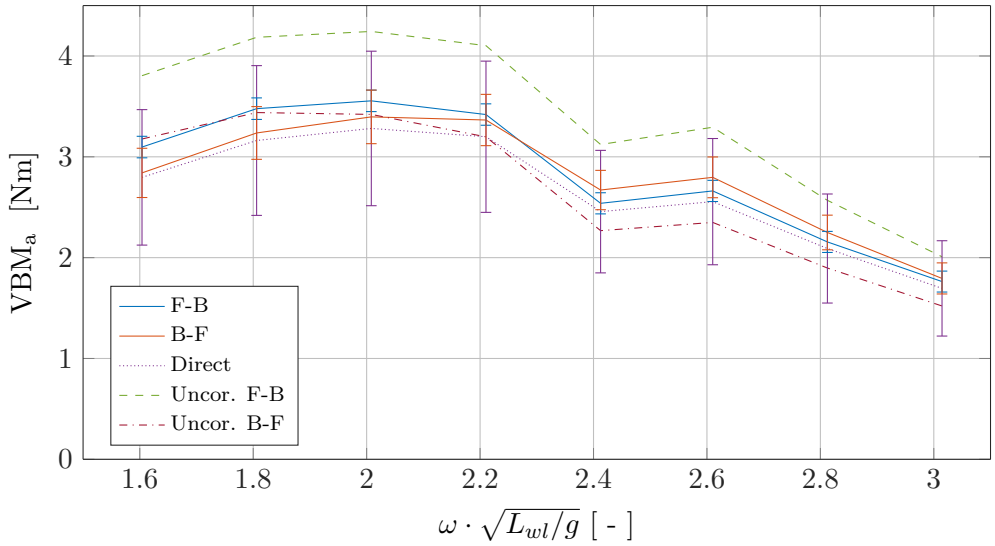

Figure 5-8: Added VBM, $V_m = 0$ m/s, $\kappa = 1/60$.

5-2-2 Forward velocity

The model was towed at 3.0 and 4.5 meters per second with the same range of encountering waves. At 3.0 m/s, the 1/30 steepness caused water to enter the model at several wave frequencies. This caused delay of the experiments and led to the decision to cancel the 4.5 m/s, 1/30 steepness experiments. The disturbance due to water end and resulting delay for that series was expected to turn out higher for the higher velocity.

The two tested steepnesses for the 3.0 m/s series show great overlap of motion response as can be seen in Figure 5-9. From that observation it is concluded that linear wave theory is still valid for the chosen frequency/amplitude ratios. The dimensionless frequencies are representing the earthbound wave frequencies, the (dimensionless) encounter frequencies are higher due to the forward velocity of the model.

Vertical bending moment

The VBM at forward speed was corrected similarly as for the moored model. Figure 5-10 shows the absolute and dimensionless values of the bending moment amplitudes at a range of wave frequencies. For low frequencies in particular, the direct method values are lower than the corrected indirect method's values. This trend of lower direct values was visible at the calm water conditions as well. Furthermore, the 95% confidence bounds are advantageous for the indirect method. However, any inaccuracies in the correction are not incorporated in the plotted bounds.

Since a constant steepness was used, the higher frequent waves' amplitudes are relatively low. This amplifies the trend of decreasing bending moment amplitudes at increasing wave encounter frequencies at the bottom graph. The dimensionless VBM shows that the trend is still present from the dimensionless wavelength of 2.0 in spite of the division of the moment by the wave amplitude. The dimensionless values at the moored experiment series show an increase with increasing wave frequency. As plotted, the results may not be directly compared since the wave encounter frequency is significantly higher at 3.0 and 4.5 m/s velocities.

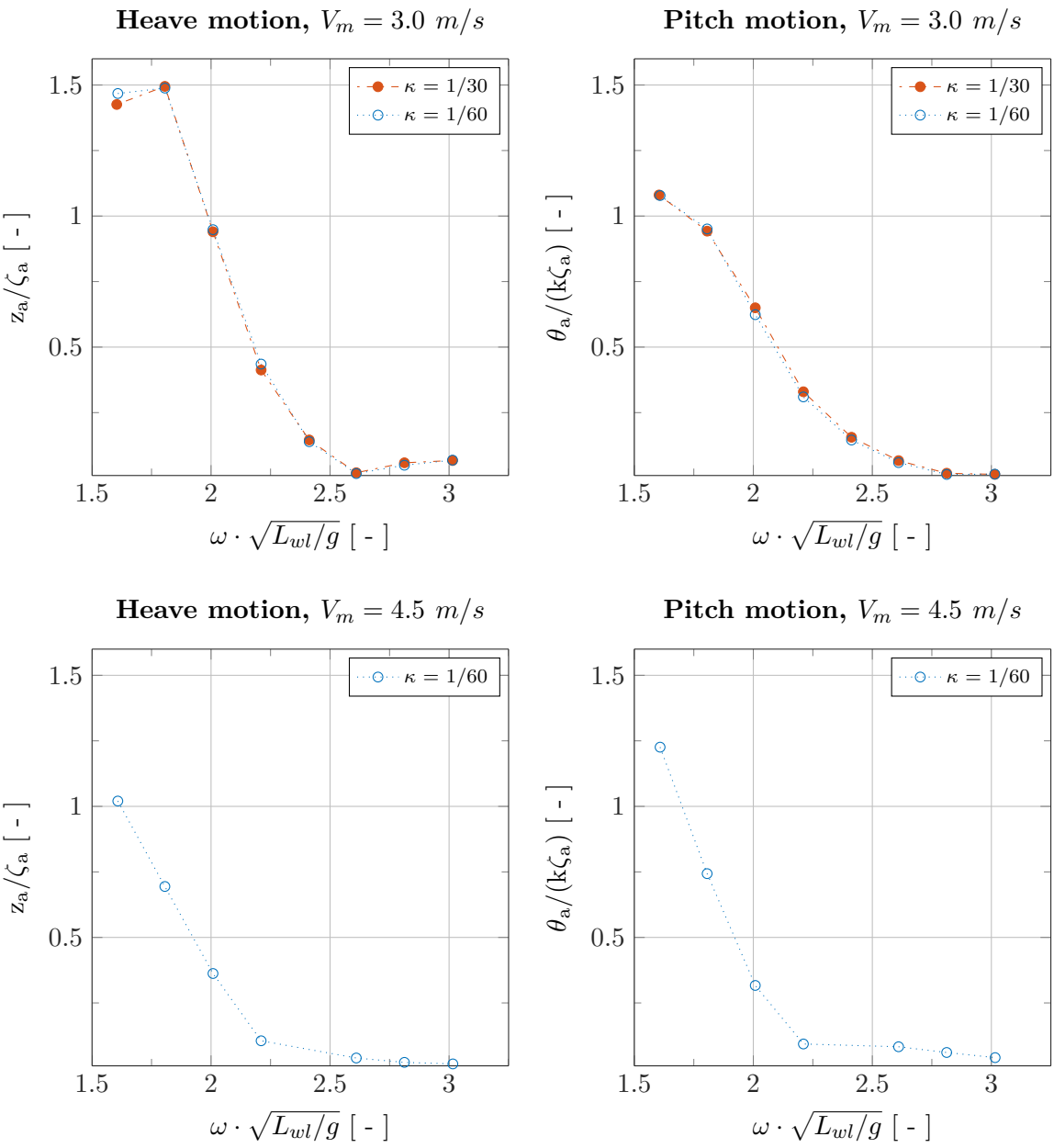

Figure 5-9: RAOs for heave and pitch, V_m = 3 and 4.5 m/s.

The results for the other situations are plotted in Appendix A. Figure A-2 shows the VBM for waves with doubled wave amplitudes. During one run the direct bending moment measurement signal was disturbed, presumably due to water ingress. That particular value is omitted in the corresponding figure. The amplitude values at the doubled wave amplitudes are generally doubled resulting. For this reason, the dimensionless bending moments correspond well.

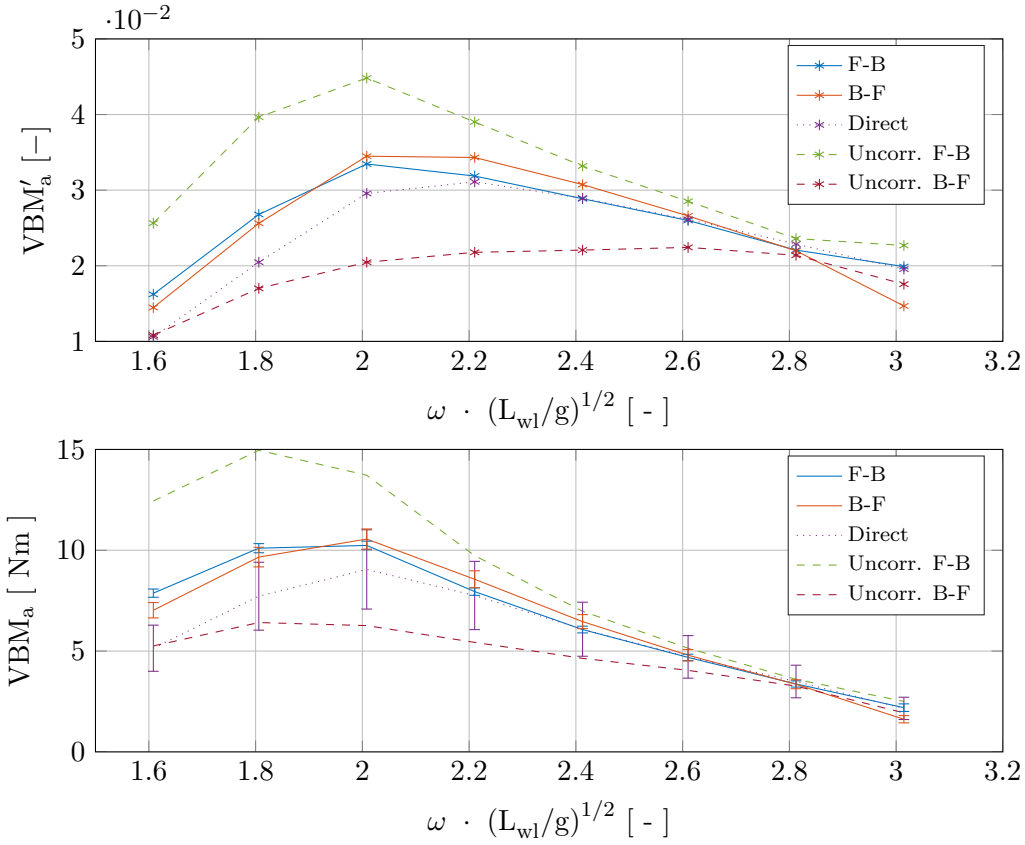

Figure 5-10: RAOs added VBM, $V_m = 3.0$ m/s, $\kappa = 1/60$.

At 4.5 m/s, the correction proved less satisfactory as can be seen from the graph of Figure A-3. Were at 3.0 m/s sine fits could successfully capture the force and acceleration signals in most cases, the 4.5 m/s runs showed impractical high noise levels at the signals. The following chapter further discusses this topic.

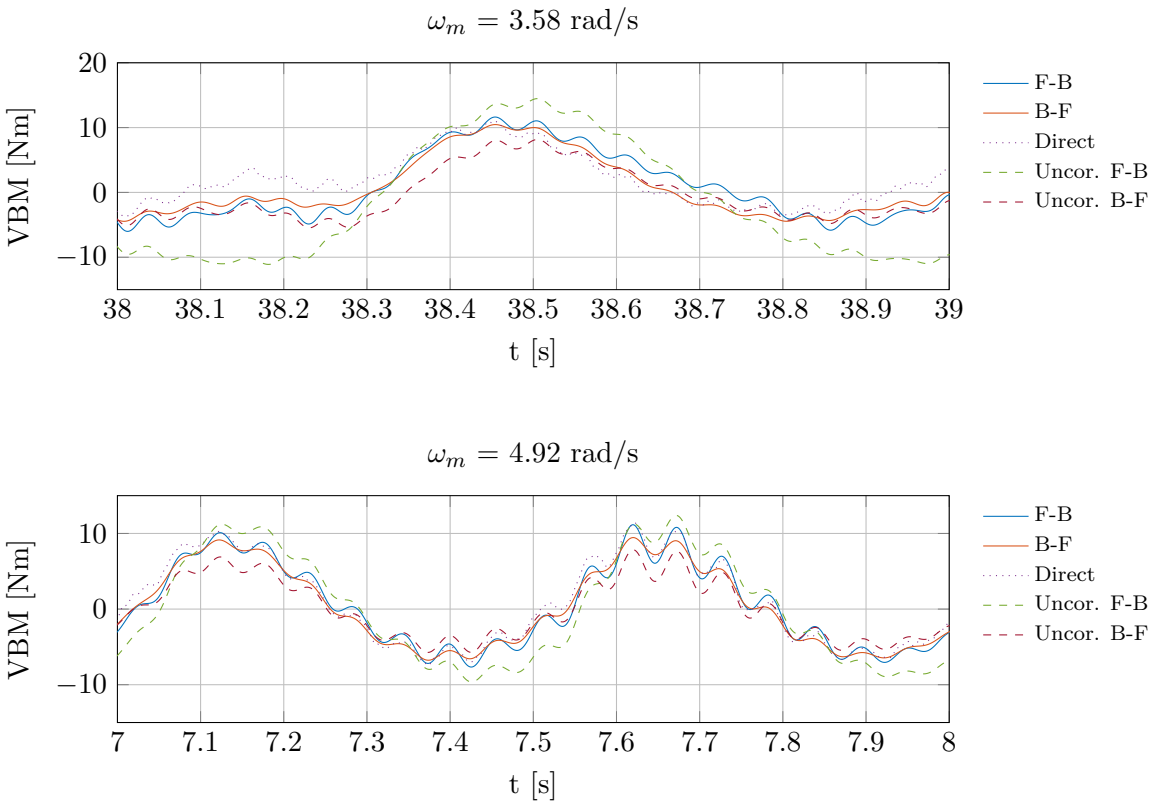

Figure 5-11: Added VBM timetrace at two wave frequencies, $V_m = 3.0$ m/s.

Part III

Interpretation and conclusions

Chapter 6

Discussion

Recapitulating the research goal: develop a measurement set-up able to accurately measure the internal loads at a segmented ship model. In the first section, the key concept choices are argued. This is followed by discussion of the calm water and regular wave experiment results. The final part of the chapter discusses the confidence bounds outcomes.

6-1 Concept

Segmentation

Validation of numerical code is more thorough by using experimental VBM data at multiple hull locations. This can be achieved by increasing the number of segments or by using a fully flexible model. The choice to use a two segment rigid backbone model is threefold.

First of all, the main research goal does not per se demand for measurement at an arbitrary location (or a number of locations). The goal was to develop a working concept of a set-up capable of measuring the internal loads. When the concept proves valid to fulfill the task, the complexity of the model can be increased by using proven technology.

Secondly, from the primary experiments crucial imperfections in the set-up could be identified. The concept of using a two segmented rigid backbone model is not one of the designated flaws in the set-up. The concept is relatively easy to construct and widely applicable, all the more reason to continue applying it. By altering parts of the set-up that are most likely to have caused the unreliable results, the results are promising.

Needless to say the same model is used because of pragmatic reasons as well. At the time of construction and assembly the available workforce was in insufficient to implement major changes in the model. Without the first two arguments the current argument would not hold. However resulting from them, the pragmatic aspect further argues for using the prior fabricated model.

Load measurement

The ship model was outfitted to deliver two options to determine the midship VBM. Both options contained insecurities regarding their practical use. Direct measurement of the bending moment is proven for (scaled) flexible backbones in numerous experimental studies, in contrast to direct measurement via strain gauges at a stiff material like carbon fiber. Moreover placing strain gauges on a anisotropic tube may question the feasibility to accurately measure the acting VBM. After calculating the (order of magnitude) of the backbone strain under bending force, the strain gauge configuration was thoroughly calibrated. Calibration showed a linear elastic behavior of the beam under perpendicular load. In comparison to the 'temple' force transducers that altogether make up the indirect measurement method, the calibration showed a small amount of hysteresis in the low load regions.

The indirect measurement method is built up using the force transducers connecting the backbone and segments rigidly. In for instance the theory of statics and in practice at bridges, this connection type is considered statically undetermined and unwanted. High forces can occur when a typical construction deforms under load. Regarding the model, this can negatively influence the measurement accuracy and ultimately break the sensors and segment construction. Due to the high stiffness and relatively low loads during the experiments, none of the results were influenced, neither impairing any of the transducer.

6-2 Calm water experiments

Extensive testing in calm water was conducted to validate the set up during quasi static conditions. The calm water resistance values correspond accurately with van Hoeve's results. Although it was foreseen that increasing the hull surface roughness would noticeably increase the resistance, a doubling was beyond expectation.

The location dependent shear force proved nonzero at the boundary, indicating presence of a non measured shear force. A set-up experiment showed that stick slip behavior is present at the guidance pole that us used to tow the model. During sliding of the pole, friction was observed. It is assumed that friction is the primary cause of the initial non zero boundary conditions. The estimated amount of friction was dependent on the friction coefficient (0.05) times the total resistance $R_{t,m}$. The shear force diagram including this term was outlined in the results. It is recommendable to measure any potential friction at the sliding pole and potential locations as the linear guide at the back. This can be achieved by adding force transducers. A second source of disturbance is the large amount of cables that was connecting the towing carriage with the ship model. The cables did not notably hit the backbone, however it is preferred to exclude potential disturbance by reducing the amount of cables.

The VBM diagrams were constructed using the same assumption. Especially for the low velocity experiments, the different 'end' values at midship cause a jump in the diagram. This jump is present all velocities, the influence decreases with increasing velocities.

When comparing the midship VBM values for the regular and rough hull it shows that the resistance component has little or no influence on the bending moment acting on the carbon fiber backbone. Especially at $Fn_{\nabla} > 2$ the bending moment increases significantly. It is

expected that this is due to the hydrodynamic lift generated during (semi)planing. The CG rises w.r.t. the non moving value from these Froude numbers.

The direct and indirect methods show a small discrepancy. The direct method values are generally slightly lower than the indirect method values. This can be caused by e.g. inaccuracies in the calibration factors or moment arms, especially for the horizontal force components due to the relatively small arms.

A third option to calculate the bending moment was compared to the other two methods. This option merely uses the measured vertical shear forces to calculate two values at the hull cut. The two values were averaged and plotted together with the other methods. It shows that the results of this method are remarkably equal to those of the other two methods. This fact confirms the conviction that the resistance / horizontal force component does not significantly effect the model's vertical bending moment

6-3 Regular head waves experiments

Measurement data of the carried out regular wave experiments required more intensive processing, in particular regarding the indirectly measured bending moment. Since the forces are measured in between the moving masses of the segments and backbone, an inertia correction must be applied. The direct measurement method is more direct regarding data processing as well. The correction method cannot be seen as versatile or universal. The terms and their parts must be constructed for each experimental set-up and ideally, the corrections are verified from controlled oscillation experiments.

Applying the correction at the four[1] cases could not deliver uniform results. The correction resulted in matching amplitude values regarding the two integration directions at the moored and 3.0 m/s experiments. The measurement signals of the experiments at 4.5 m/s forward speed did not properly correct for inertia forces. The established correction method takes insufficient account of the high level of noise present and the increased non sinusoidal force response.

This makes the direct measurement option favorable in case of dynamic load. On the other hand, the confidence bounds of the indirect method are favorable over the direct method. The chapter's final section further discusses the confidence bound levels. First, the confounding effects at the 4.5 m/s runs are argued.

6-3-1 Resonance and other confounding effects

The resonance levels at the 3.0 m/s runs were acceptable in the sense that the undisturbed force/moment signals could be extracted from the raw signals successfully. Likewise, the vertical acceleration and (determined) rotational acceleration signals at most runs are harmonic at a frequency equal to the wave encountering frequency.

Apart from this observation, a frequency analysis of the raw signals showed apart from the excitation frequency, a ≈ 18 Hz component is present in the signals. This component is clearly

[1] moored, towed 3.0 m/s at two wave steepnesses and towed at 4.5 m/s

visible in time-trace plots as was illustrated in Figure 5-11. Distinct experiments showed that an impact load in surge (x) direction results in resonant vibrations largely consisting of a $\approx$ 18 Hz component. Impact in heave direction did not result in any significant resonance. Although conclusive evidence is missing, it is likely that the origin of this resonance frequency can be found at the guidance pole connection. The 18 Hz component was absent at earlier tests in which a significant part of the set-up was assembled.

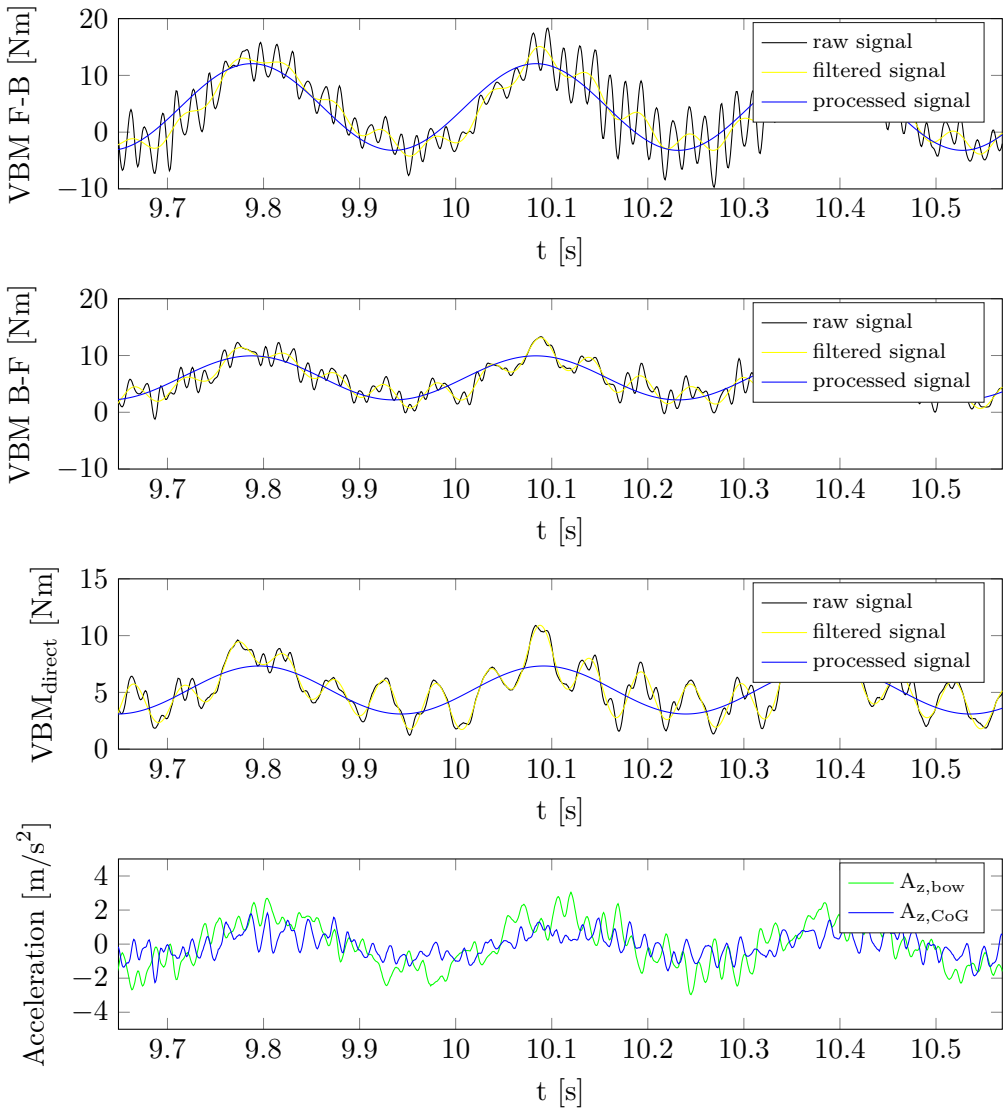

Figure 6-1: (In)direct VBM and acceleration timetrace, V_m = 4.5 m/s, ω_m = 5.81 rad/s.

At higher speed, the level of noise as part of the total signal increases. Especially at the higher wave frequencies (equally: lower wave amplitudes) the share of resonance increases up to levels equal to the excitation frequency. The acceleration signals are equally susceptible to this effect, thereby decreasing effectiveness of the correction. Figure 6-1 illustrates the large amount of high frequent vibration as part of the captured signals. Please note that the acceleration signals are representing the raw signals. The top and second graphs indicate the

indirect bending moments composed from the Front-to-Back and vice versa. In particular the directly measured bending moment and the vertical acceleration signals are greatly influenced by higher order behavior. As a result, the (corrected) Vertical Bending Moment (VBM) amplitudes as obtained from the applied sine fits are underestimated in all probability. This is further illustrated in Figure A-3. In particular at the dimensionless wave frequency of 2.61, the direct and Back-to-Front indirect bending moment amplitudes show a major trend change.

Slamming is another phenomenon that was present at many 4.5 m/s runs. A slam results in a non harmonic vertical acceleration. Likewise, the event is reflected in the directly measured bending moment signal and the force transducers. The non harmonic character of the signals make the used sine fits less usable and more prone to errors. More sophisticated data interpretation is required to fully incorporate the effects of slamming events.

6-4 Confidence bounds

A number of plots show an error bar at the plotted values. The bar is built up from bias and precision errors. From the calibration of the force transducers and the strain gauges at the backbone a 95% confidence level of the calibration factor was determined. Together with factors as inaccuracies of moment arms, total confidence level was generated for each measurement.

Although aggregated from a large number of inaccuracies, the confidence bounds of the indirect method show a smaller bandwidth than the direct method. This is due to the fact that the level of strain at the backbone is in the lower regions of the measurement band of the strain gauges. This led to a relatively large inaccuracy in the used calibration factor. This inaccuracy reflects in the total inaccuracy by multiplying the relative inaccuracy with the measured value. As a result it is proportional to the measured VBM value. In the graph this can be seen from the increasing error bar lengths for increasing bending moment values.

To minimize this error it is advisable to beforehand

1. Calculate the expected forces and moments.
2. Choose force/moment sensor ranges according to the expected values.
3. Calculate natural frequencies of individual components and system if possible.
4. Reflect values to expected excitation frequencies, reconsider set-up if resonance is expected.

The current confidence bounds show that although the direct method values are close to the indirect values, the accuracy seems insufficient to validate numerical code. By increasing the measurement resolution as briefly described in the enumeration, it is expected that a significant gain in accuracy may be obtained.

Chapter 7

Conclusions

A thorough series of calm water and regular wave experiments was conducted. The experiments were aimed to validate a designed measurement set-up for internal load measurement on a two segment HSC.

Before carrying out the experiments, the formerly used set-up was partly reconstructed to investigate the error sources. From a series of static tests with closely monitored conditions, the sources were successfully determined. Founded upon earlier internal load measurement studies while bearing in mind that at high speeds non linear effects (e.g. lift) will play a part, the earlier used set-up was reconsidered. Hereafter, a similar set of static experiments was carried out to verify the new set-up. The results showed that the (combination of) applied forces were properly measured by the set of force transducers, opening the way for conducting towing tank experiments. A second measurement concept was implemented to directly compare two options. The strain gauges forming the direct method were extensively calibrated before final assembly. The calibration demonstrated a linear elastic behavior of the backbone under bending. Nonetheless, the calibration factor showed more spread compared to the calibration factor of the force transducers.

From the quasi static calm water experiments the fundamental force equations could be verified. The results showed a global equilibrium in both vertical and horizontal direction. From this finding, the shear force and bending moment was determined from the individual components. The second method, directly measuring the VBM acting on the backbone, required significantly less processing to obtain usable results. The two methods delivered similar results for especially the semi-planing regime velocities. At lower velocities, the direct method Vertical Bending Moment (VBM) results were in most cases marginally lower.

At the quasi static towing experiments in particular, four force transducers are sufficient to determine the midship VBM. When only vertical shear force is measured, the bending moment may be calculated by taking the mean of the front and rear segment values. This method requires the backbone and towing arm positioned practically at the vertical location of the net acting resistance force to minimize the contribution of horizontal load. A second option is to use transducers at one segment only. In case of the used model meaning 4 force

transducers for the rear segment or 5 force transducers for the front segment. Two downsides to this method are that the VSF along the backbone cannot be determined properly and that one cannot verify the boundary conditions by comparing the front and rear segment contributions.

The regular wave experiments' sensor data required more thorough processing, especially the indirect method. With inertia correction terms included, the bending moment was fairly similar at most conditions for calculations using front segment forces and rear segment forces. At increasing forward speeds, the amount of noise increases considerably. At the 3.0 m/s experiments, the filtering and fitting proved effective. In contrast, at 4.5 m/s the results were less satisfactory due to significant noise levels and nonlinearities of the force response. The guidance pole construction seems the cause of the high levels of resonance at high velocities. The use of this construction (especially) at high velocities should be reconsidered. In addition, more extensive signal processing, taking the impact load into account correctly, may further improve the results.

The current set of confidence bounds are beneficial for the indirect method. The increasing uncertainty for the direct method at increasing bending moments makes sense according to the uncertainty calculation foundation, however physically it is contradictory. A higher bending moment results in higher strain levels. Since the strain levels are on the lower boundary of the measurement range of the strain gauges, higher strain will physically result in more accurate measurements.

In short, it can be concluded that the assembled hull performs well under static and quasi static conditions. This includes sailing at a constant high speed in calm water. For the tested wave conditions, the set-up performed well at sub planing velocities. In fact, the 3.0 m/s runs correspond to the approximate maximum speed of the full scale vessel. At semi planing velocities in regular waves, the nonlinear response and high amount of resonance demand for adjustments in particular regarding the 'propulsion' method. Moreover it demands for more advanced data processing. A more comprehensive set of recommendations is outlined in the next section.

Recommendations

The purpose of this section is threefold. The section starts with findings during the research, reflected together with recommendations to increase reliability and minimize the amount of factors that can negatively influence the results of future experiments. In the subsequent subsection, a set of recommendations for future work regarding post processing is outlined. An example is to process the irregular head wave experiments' data. In the final part, a set of recommendations for future work regarding development of experiments with segmented ship models is proposed.

- A noticeable amount of vertical force was most probably transferred at the roller supports of the towing construction. To completely verify the set-up, it is recommended to place a vertical force transducer at the interface of the model and this connection.
- In particular at high velocities, a significant resonance was present at the set-up. The expected root cause is that same towing construction. Supported by the first recommendation, it is recommended to reconsider towing experiments and conduct future internal load measurement experiments using free sailing models. Another advantage of using a free sailing model is that the required correction is reduced significantly. A large part of the the mass of the backbone construction is accounted for by the steel towing arm. Reducing the amount of correction increases the reliability of measurement results.
- Around 15 cables were connected from the carriage to the model. To allow heave and pitch motion, the cables were freely hanging and had slack. Besides potentially influencing the model's inertial properties, the cables all together were rather stiff and therefore were possibly disturbing the motions and forces. It is advisable to implement either a wireless system with the downside of a battery requirement or a system that aggregates the signals at the model, reducing the amount of cables running from the model to the carriage. At a free sailing model the first option has a strong preference obviously.
- The calculated confidence bounds are partly based on a bias error for errors during calibration. As a result, the uncertainty is expressed as percentage of the measured force/moment. Physically, a contradictory situation is the case. With increased load and thus deflection at the backbone, the accuracy of the strain gauges increases. When small load is applied, the strain is at the lower boundary of the strain gauge's measurement band. It is advisable to reconsider the used uncertainty calculation regarding the bias uncertainty of calibration.
- To determine the precision error levels more accurate, it is advisable to increase the number of repeated runs to approximately 10. The repetitions should be carried out at a minimum one run per series. Here series can indicate a range of velocities in calm water or a range of wave frequencies at a constant velocity for example.

With available data from regular and irregular head wave experiments recommended further steps include:

- Investigate the VBM behavior at slamming events. The signal of vertical acceleration at the bow is most useful to identify slamming events. The sensor's time trace shows a brief high peak at the moments the bow pierces the waves. A sine fit insufficiently represents the actual signal, therefore more extensive data processing is required for run conditions involving slamming.
- Investigate the VBM reproduction at the irregular wave experiments. Although the significant wave height of the tested wave spectrum was rather low, most likely slamming events occurred.
- After further processing, reflect the experiments' outcomes to strip theory code. The experiments conduced with (semi) planing conditions can be compared with the numerical code FASTSHIP. If the motions prove correct, focus on the vertical bending moment.

To further support the assumption that horizontal load is not or negligibly influencing the vertical bending moment at slender ships:

- Conduct a series of experiments with varying height of backbone center line. The assumption is that with the center line significantly higher than the resulting resistance force the resistance component will considerably contribute to the model's VBM. Fortunately, for regular full scale steel and aluminium ships the geometrical neutral axis (in fact plane) is close to the water line height.
- The influence of the point of action of the ship's thrust was not part of the current research. It is known that the point of action influences the steady state trim angle. Dependent on orientation and location, the point of action may influence the vertical bending moment. By altering the thrust (equivalently towing) location, the possible influence can be investigated.

Appendix A

Experiment results

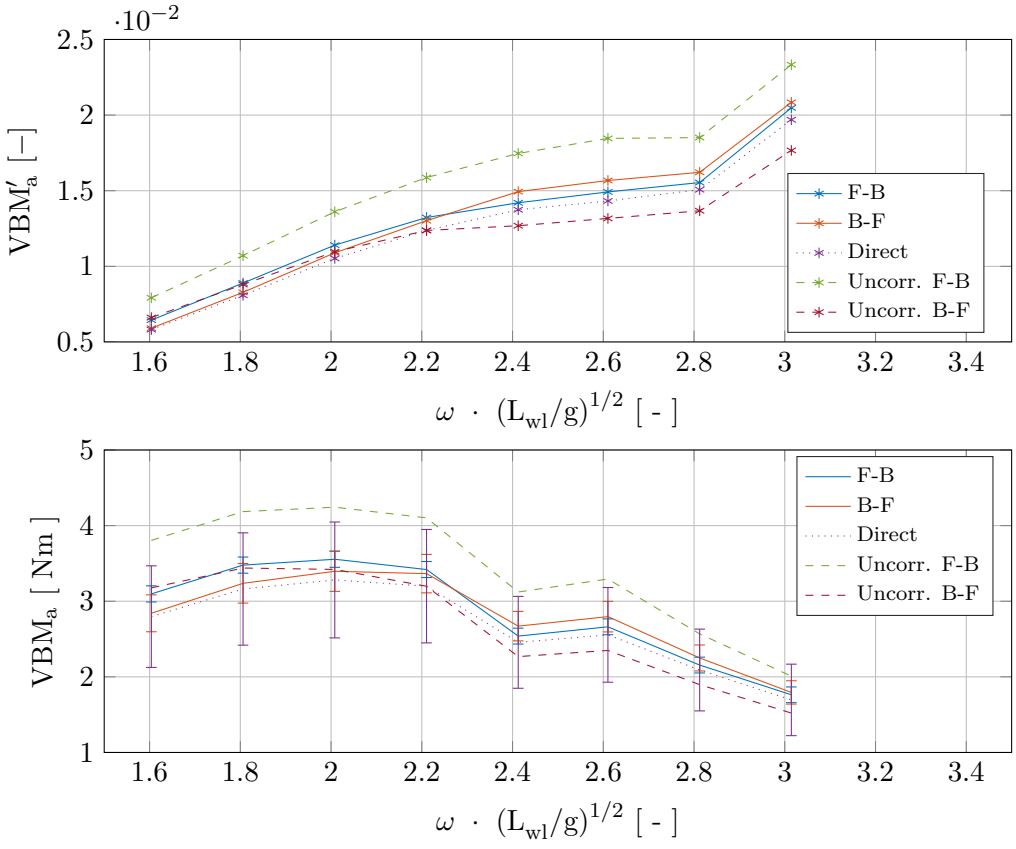

Figure A-1: RAOs and direct VBM values, $V_m = 0.0$ m/s, $\kappa = 1/60$.

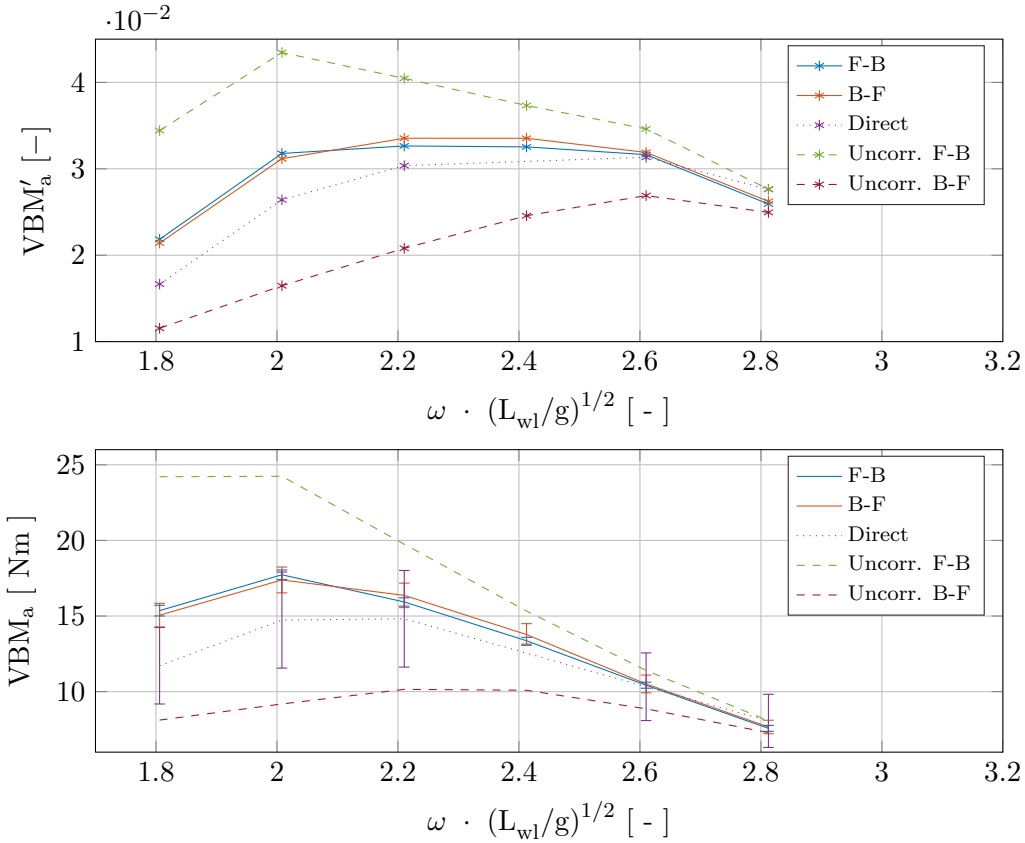

Figure A-2: RAOs and direct VBM values, $V_m = 3.0$ m/s, $\kappa = 1/30$.

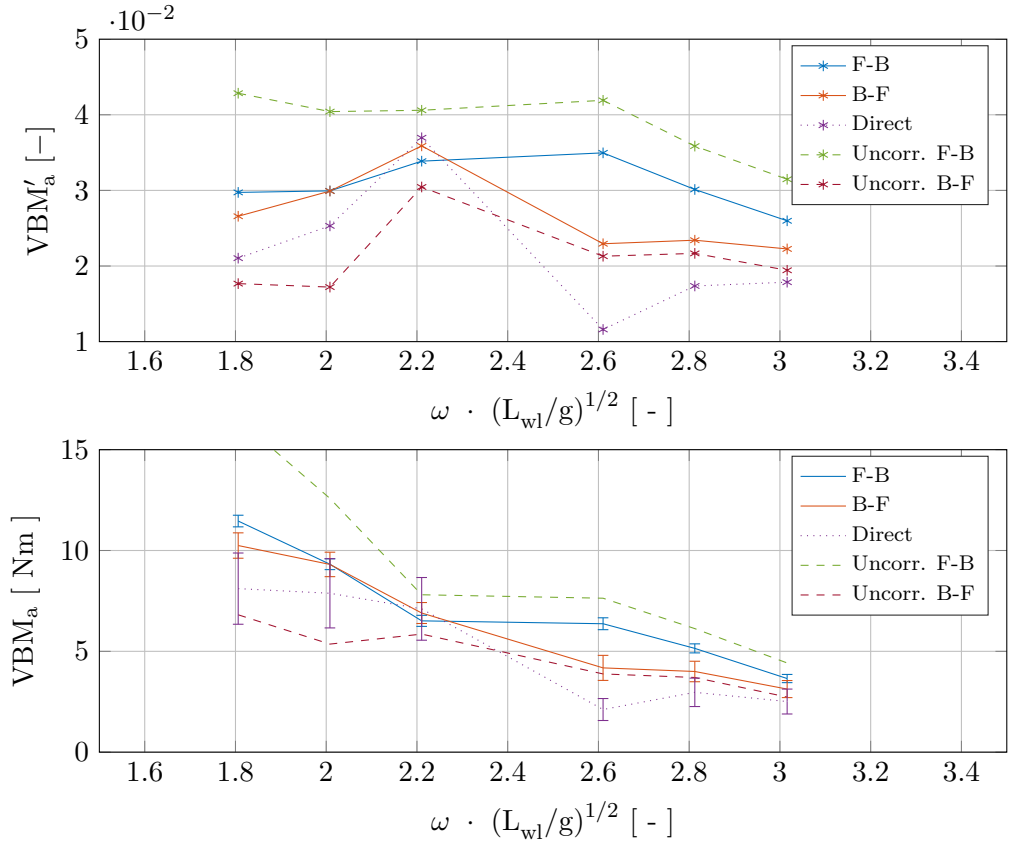

Figure A-3: RAOs and direct VBM values, $V_m = 4.5$ m/s, $\kappa = 1/60$.

Appendix B

Euler-Bernoulli beam theory

B-1 Euler-Bernoulli beam equation

Although the Euler-Bernoulli beam theory is a simplification of actual beam load-carrying and deflection characteristics of beams, for small deflections at slender beams the theory is sufficiently reliable. The Euler-Bernoulli beam equation describes the relationship between the beam's deflection and the applied load:

$$\frac{\mathrm{d}^2}{\mathrm{d}x^2}\left(EI\frac{\mathrm{d}^2w}{\mathrm{d}x^2}\right) = q \tag{B-1}$$

With:

x	$[m]$	the spatial coordinate that is located along the beam's longitudinal axis.
E	$[Pa]$	the elastic modulus of the beam's material, for anisotropic materials beams such as carbon fiber tubes this value is dependent on the direction of interest.
I	$[m^4]$	the second moment of area of the beam's cross-section. Calculation using (B-3) for a beam with its axis along x and a load along z.
q	$[N/m]$	a distributed load, which can be a function of x, w or any other variable.
w(x)	$[m]$	describing the deflection of the beam in z direction at position x.

The equation simplifies the beam to a one dimensional system. The deflection w (in z direction) is only dependent on the x-coordinate.

With the centroid of the cross-section at $y = z = 0$ When the product EI is constant over the beam's length, which is the case for a regular carbon fiber tube, (B-1) can be rewritten as:

$$EI\frac{\mathrm{d}^4w}{\mathrm{d}x^4} = q(x) \tag{B-2}$$

B-2 Second moment of area

The second moment of inertia for an arbitrary cross section is defined by:

$$I = \int\int z^2 \, \mathrm{d}y \, \mathrm{d}z \tag{B-3}$$

For an annulus cross section, which is typical for hollow tubes, the equation boils down to:

$$I_y = \frac{\pi}{4}\left({r_2}^4 - {r_1}^4\right) \tag{B-4}$$

For thin tubes $r \equiv r_1 \approx r_2$ and thickness $t \equiv r_2 - r_1$ than,

$$\left(r_2^2 + r_1^2\right)(r_2 + r_1) \approx \left(2r^2\right)(2r) = 4r^3 \tag{B-5}$$

$$I_x = I_y = \pi r^3 t \tag{B-6}$$

For the carbon fiber tube $r_2 = 0.060\ m$, $r_1 = (0.060 - 0.0025) = 0.0575\ m$. Than $I_y = 1.59 \cdot 10^{-6}\ m^4$.

B-3 Modulus of Elasticity

The modulus of elasticity, also referred to as Young's Modulus and E-Modulus, indicates the ratio between stress and strain:

$$E \equiv \frac{tensile\ stress}{extensional\ strain} = \frac{\sigma}{\epsilon} = \frac{F/A_0}{\Delta L/L_0} \tag{B-7}$$

With:

E	$[Pa]$	the modulus of elasticity.
σ	$[Pa]$	the stress.
ϵ	$[-]$	the strain.
F	$[N]$	the exerted force.
A_0	$[m^2]$	the original cross sectional area on which the force acts.
ΔL	$[m]$	the length change in direction of the applied force.

For tubes consisting of winded carbon filaments which are assembled using resin, the modulus of elasticity is not as straightforward as for instance a aluminium tube. Whereas aluminum, among other metals, is an isotropic[1] material, a carbon fiber tube cannot be considered isotropic. The supplier provided the following data:

Outer diameter	60	$[mm]$
Inner diameter	55	$[mm]$
E-modulus	265	$[GPa]$
Possible deviation	±10-15	%

In the current calculation, the Young's modulus of 265 GPa is used. The modulus was compared with a value obtained from the deflection under several loads load using the formula for deflection of a (weightless) end loaded cantilever beam ($\delta = \frac{FL^3}{3EI}$) and proved accurate.

[1] Of equal physical properties along all axes.

B-4 Strain

Strain in an Euler-Bernoulli beam should be determined to ultimately relate the stresses to the deflection. In the current case, the strain is the final answer that is required. The relation between strain and deflection of the beam is interesting to compare the calculated values with measured deflection during an experiment.

By assuming that the normals to the neutral surface remain normal during the deformation and that the deflections of the beam are small, it is implied that the beam bends into an arc of circle with radius r and the neutral surface does not change in length during the deformation.

The following theory is derived from the E-B beam model. A beam element of length $\mathrm{d}x$ does not change in length after bending. For small deflections, the beam deforms into an arc of radius r. Let $\mathrm{d}\theta$ be the angle subtended by the arc, then $\mathrm{d}x = r\ \mathrm{d}\theta$.

Now consider another segment at a distance z above the neutral surface. The initial length of the element is equal, viz. $\mathrm{d}x$, however after bending the element becomes $\mathrm{d}x' = (r - z)\ \mathrm{d}\theta = \mathrm{d}x - z\ \mathrm{d}\theta$. The strain in that particular element is given by:

$$\varepsilon_x = \frac{\mathrm{d}x' - \mathrm{d}x}{\mathrm{d}x} = -\frac{z}{r} = -z\ \kappa \tag{B-8}$$

With κ the curvature of the beam. The curvature can be expressed in terms of the deflection w. The angle made by the neutral surface and the x-axis is:

$$\theta(x) = \frac{\mathrm{d}w}{\mathrm{d}x} \tag{B-9}$$

The curvature is the change of slope over length, mathematically expressed as:

$$\frac{\mathrm{d}\theta}{\mathrm{d}x} = \frac{\mathrm{d}^2w}{\mathrm{d}x^2} = \kappa = \frac{1}{r} \tag{B-10}$$

The strain in the beam then may be expressed as:

$$\varepsilon_x = -z\frac{\mathrm{d}^2w}{\mathrm{d}x^2} \tag{B-11}$$

B-5 Loads

The used magnitude, direction and location loads is based on measurement data from earlier carried out experiments whereas that data was found unusable. Fortunately, the unexplained values related to the horizontal forces. These values are not taken into consideration for the current calculation. The loads are generally represented through the function $q(x, t)$, however since only static loads are considered the load is only a function of the position.

The Dirac delta function (referred to as $\delta(x)$) is used to model the point loads. The loads F_1 and F_2 are located at two positions: at $x_1 = 0.15\ m$ and $x_2 = 0.73\ m$ respectively, corresponding to the backbone used in the prior model experiments. Figure B-1 shows an impression of the theoretical beam and applied loads. Since the deflections are considered

small, the superposition principle can be used. By substituting the load of Eq. (B-2), the equation becomes:

$$EI\frac{\mathrm{d}^4 w}{\mathrm{d}x^4} = F_1\delta(x - x_1) + F_1\delta(x - x_2) \tag{B-12}$$

B-6 Boundary conditions

When assembled in the segmented ship, the beam is considered as a free-free beam. This implies that there are no forces and moments present in at the tips of the beam. For the current calculation, the beam's boundary conditions comply with a cantilever beam. For a beam of length L [m] clamped at $x = 0$, the boundary conditions are formulated in (B-13). Figure B-1 depicts the boundary conditions and acting forces.

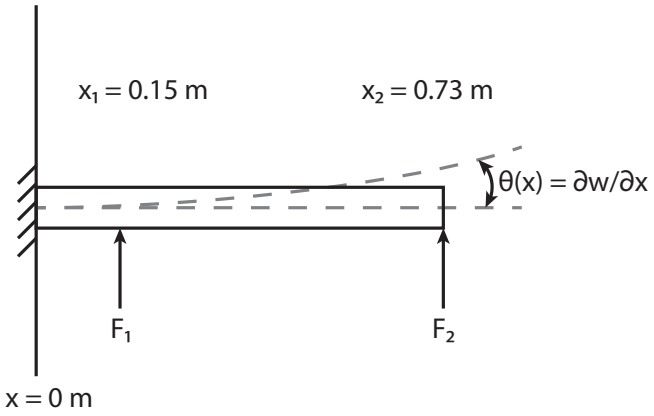

Figure B-1: Conditions for analytic strain calculation.

$$\begin{aligned} w|_{x=0} &= 0 & \left.\frac{\partial^2 w}{\partial x^2}\right|_{x=L} &= 0 \\ \left.\frac{\partial w}{\partial x}\right|_{x=0} &= 0 & \left.\frac{\partial^3 w}{\partial x^3}\right|_{x=L} &= F_2 \end{aligned} \tag{B-13}$$

B-7 Solution

B-7-1 Displacement

For a beam with invariant bending stiffness EI, the general expression for the transverse displacement becomes:

$$w(x) = -\frac{1}{EI}\left(-\frac{1}{24}q_1\ x^4 + \frac{1}{6}C_1\ x^3 + \frac{1}{2}C_2\ x^2 + C_3\ x + C_4\right) \tag{B-14}$$

Since no distributed force is applied to the beam, the constants C_1 and C_2 can be found from the boundary conditions at the beam's end to give

$$C_1 = F_2 \tag{B-15}$$
$$C_2 = -F_2 \cdot L \tag{B-16}$$

To find the displacement, (B-14) is substituted into the boundary conditions for $x = 0$. This results in $C_3 = C_4 = 0$. Consequently, the expression for beam displacement is:

$$w_2(x) = -\frac{1}{EI}\left(\frac{1}{6}C_1\ x^3 + \frac{1}{2}C_2\ x^2\right) \tag{B-17}$$
$$= -\frac{x^2}{2EI}\left(\frac{1}{3}F_2(x - 3L)\right) \tag{B-18}$$

For the second load, the displacement is differently expressed for two intervals. For the part of the beam located at $x \geq x_1$, the slope is constant when only the second load is considered. This is formally expressed as:

$$w_1(x) = \begin{cases} -\frac{x^2}{2EI}\left(\frac{1}{3}F_1(x - 3x_1)\right) & \text{for } \ 0 \leq x \leq x_1 \\ -\frac{x_1^2}{2EI}\left(\frac{1}{3}F_1(x_1 - 3x)\right) & \text{for } \ x_1 \leq x \leq L \end{cases} \tag{B-19}$$

From the superposition principle, the total displacement is the summation of the individual displacement expressions:

$$w(x) = w_1(x) + w_2(x) \tag{B-20}$$

B-7-2 Strain

As discussed in Section B-4 the relation between strain and displacement becomes apparent by differentiating Eq.(B-20) twice to x. One differentiation results in an expression for the angle of the neutral surface with respect to the x-axis, mathematically shown in (B-9). Substituting (B-20) into that equation yields:

$$\theta(x) = \begin{cases} \frac{F_1 x}{2EI}(2x_1 - x) + \frac{F_2 x}{2EI}(2L - x) & \text{for } \ 0 \leq x \leq x_1 \\ \frac{-F_1 x_1^2}{2EI} + \frac{F_2 x}{2EI}(2L - x) & \text{for } \ x_1 \leq x \leq L \end{cases} \tag{B-21}$$

Substituting this equation into (B-10) results in the following expression:

$$\kappa(x) = \begin{cases} \frac{F_1}{EI}(x_1 - x) + \frac{F_2}{EI}(L - x) & \text{for } \ 0 \leq x \leq x_1 \\ \frac{F_2}{EI}(L - x) & \text{for } \ x_1 \leq x \leq L \end{cases} \tag{B-22}$$

Substituting this into (B-11) with z equal to the beam's outer radius yields:

$$\varepsilon_x = \pm\ z \cdot \kappa(x) = \begin{cases} \pm\ z \cdot \left(\frac{F_1}{EI}(x_1 - x) + \frac{F_2}{EI}(L - x) \right) & \text{for } \ 0 \leq x \leq x_1 \\ \pm\ z \cdot \frac{F_2}{EI}(L - x) & \text{for } \ x_1 \leq x \leq L \end{cases} \tag{B-23}$$

The bending stiffness is the product of the outcomes of the calculations stated in Sections B-2 and B-3, $EI = 4.21 \cdot 10^5\ [Nm^2]$. A typical value of $F_1 = -40N$ and $F_2 = 50N$ are taken from experimental outcome. For the maximum strain at midship, $x = 0, z = 0.03\ m$.

$$\varepsilon_x = \pm\ 0.03 \cdot \left(\frac{F1}{4.21 \cdot 10^5} \cdot 0.15 + \frac{F2}{4.21 \cdot 10^5} \cdot 0.73 \right)$$

$$\mu\varepsilon_x = \pm 2.17 \tag{B-24}$$

By placing the strain gauges at the top and bottom, this value can be considered double.

B-7-3 Natural frequencies of a free-free beam

As check for possible influence of excitation that results in resonance of the beam, the theoretical natural frequencies are determined below. The bending vibrations of a beam is described by the following equation:

$$EI \frac{\partial^4 w}{\partial x^4} + \rho A \frac{\partial^2 w}{\partial t^2} = 0 \tag{B-25}$$

New components here are the beam's sectional area A and material density ρ. No damping term is present, any internal loss is neglected. The solution of this equation can be written as a standing wave $y(x,t) = w(x) \cdot u(t)$. This results in the characteristic equation, relating the circular frequency ω to the wavenumber k.

$$\omega_n = \sqrt{\frac{EI}{\rho A}} \cdot \frac{(k_n L)^2}{L^2} \tag{B-26}$$

The spatial part is defined as:

$$w(x) = C_1 sin(kx) + C_2 cos(kx) + C_3 sinh(kx) + C_4 cosh(kx) \tag{B-27}$$

From the boundary conditions as stated in Chapter 2's Eq. (2-24), the derivatives for a beam with length L are:

$$\begin{aligned} -C_2 + C_4 &= 0 \\ -C_1 sin(kL) - C_2 cos(kL) + C_3 sinh(kL) + C_4 cosh(kL) &= 0 \\ -C_1 + C_3 &= 0 \\ -C_1 cos(kL) + C_2 sin(kL) + C_3 cosh(kL) + C_4 sinh(kL) &= 0 \end{aligned} \tag{B-28}$$

Using lines 1 and 3 to rearrange lines 2 and 4, the following matrix is obtained:

$$\begin{bmatrix} sinh(kL) - sin(kL) & cosh(kL) - cos(kL) \\ cosh(kL) - cos(kL) & sin(kL) + sinh(kL) \end{bmatrix} \begin{bmatrix} C_1 \\ C_2 \end{bmatrix} = \begin{bmatrix} 0 \\ 0 \end{bmatrix} \tag{B-29}$$

The non trivial solution of this system of equations is:

$$cosh(kL)cos(kL) = 1 \tag{B-30}$$

Eq.(B-30) has infinite solutions and can be solved numerically. The first three are outlined in Table B-1.

Table B-1: Numerical solutions to $cosh(kL) \cdot cos(kL) = 1$.

Mode order n	k_nL
0	0
1	4.73
2	7.85
3	11.00

Substituting the first order value k_1L in equation (B-26) yields the first natural frequency of the beam. From Sections Section B-2 and Section B-3 $EI = 4.21 \cdot 10^5$ $[Nm^2]$. The density of carbon fiber tube material is $\rho_{cf} = 1550\ kg/m^3$ and the cross sectional area $A_{tube} = 4.52 \cdot 10^{-4}\ m^2$.

From (B-26), $\omega_1 = 7711\ rad/s\ \simeq\ 1227\ Hz$. This value is for just the carbon fiber tube. To get a sense of the natural frequency in case of a tube with the weight of the total model (approx. 29 kg), the first mode natural frequency is approximately 232 Hz.

Appendix C

Data processing

The method used to calculate presented results of Chapter 5 is outlined in this Appendix. The Appendix is subdivided in outlining the methods used for calm water runs and runs in regular waves. Part of the measurement data was initially processed using Microsoft Excel in order to quickly gain an understanding of the phenomena and trends. Eventually Matlab was used to read, order, calculate and plot the data. Only the calculation part is explained below. First multiple aspects of the zero run are explained.

C-1 Zero runs

Prior to all runs a zero-run was recorded. For 60 seconds, the data for all 29 channels was recorded and saved. The mean of this run is subtracted from the subsequent measurement run. During the zero run the water was calm and the model was non-moving. As a result of this subtraction, a number of acting forces is removed from the measurement data. The forces are listed in the top Table C-1. Figure C-1 shows a schematic overview of the system and acting forces during a zero run. For a more detailed description of the measurement set-up, please refer to Section 3-6. The two bold arrows at LCG represent the buoyancy and gravitational forces for the entire system. Since the model is stationary, the gravitational force F_g, acting at the Center of Gravity (CG) and the resultant buoyancy force acting at Center of Buoyancy (CB) are located at the same lengthwise location. This equilibrium is not necessarily true when one looks at the resulting force balance at a segment. The force times the potential resulting arm initiates a moment of magnitude $F_{g,[segment]} \cdot 0.5L_{[segment]} + F_{b,[segment]} \cdot 0.5L_{[segment]}$. The moments will be transferred through the (vertical) force transducers connecting the backbone with the segments. The zero run values of the vertically oriented force transducers therefore include the gravitational force of the backbone construction and potentially the moment created by inequality in mass and bouyancy distribution at the segment. If this inequality exists, eventually an initially measured VBM at midship results.

If the model scale mass distribution matches the full scale mass distribution and the force transducers were properly zeroed (ideally in a zero gravity environment) the still water bend-

Table C-1: Model mass and inertial properties.

	Symbol in Figure C-1.
Resulting buoyancy force on front segment.	$F_{b,front}$
Resulting gravitational force on front segment.	$F_{g,front}$
Resulting buoyancy force on rear segment.	$F_{b,rear}$
Resulting gravitational force on rear segment.	$F_{g,rear}$
Resulting gravitational force on backbone construction.	$F_{g,backbone}$
Vertical forces at force transducers	$F_{ff,v}, F_{fm,v}, F_{rm,v}, F_{rr,v}$

ing moment is registered during a zero run. Both cases are not applicable here, therefore the model's still water bending moment cannot be determined experimentally.

The Still Water Bending Moment (SWBM) was determined numerically. For this calculation, the ship was divided into 54 strips. The mass distribution as provided by Damen Shipyards was used. Buoyancy is the only hydromechanic force acting on the model. Via the wetted cross section this force was calculated for each strip. The area was assumed a triangle between the keel and the chines (or waterline) and a trapezium between the chines and the waterline. The buoyancy force and weight were summed, yielding the load distribution. The resulting VSF and finally SWBM at midship was determined 10.7 Nm.

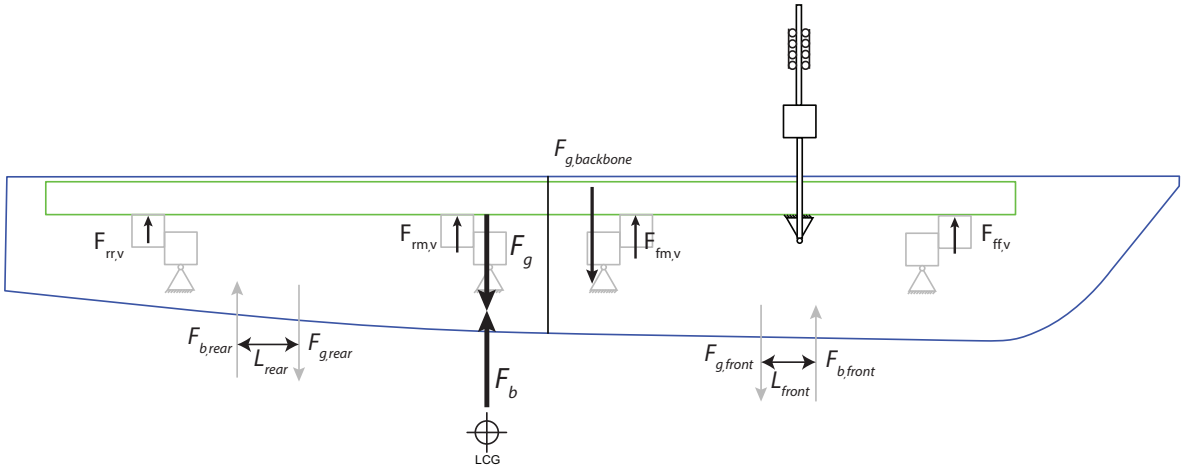

Figure C-1: Acting forces during zero run.

All Vertical Bending Moment (VBM) values presented in this thesis are in fact the additional moment as result of forward velocity and/or encountering waves.

C-2 Calm water

Horizontal and vertical force balance

The measurement data of the all runs was trimmed such that the forward velocity is constant. In calm water this causes the model to behave quasi static. For quasi static behavior, the sum of all horizontal and vertical forces should be zero. In case of an existing pitch angle θ,

the force tranducers' values must be decomposed into a vertical and horizontal component to obtain the earthbound force equilibrium equations. Figure C-2 shows the free body diagram of the backbone. A positive pitch angle indicates bow up.

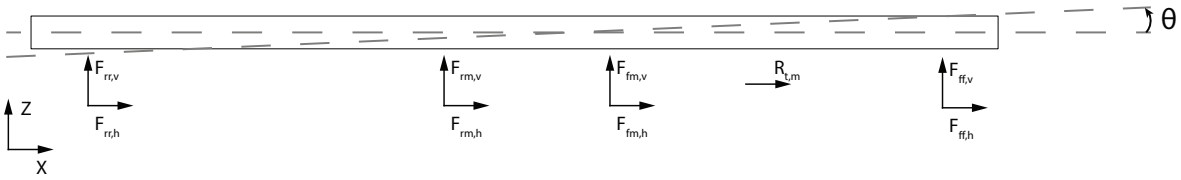

Figure C-2: Backbone free body diagram.

The combination of indexes i j, k indicate the force transducer.

- i: section [front rear]
- j: nearest location on section [front midships rear]
- k: orientation [vertical horizontal]

$$
\begin{aligned}
(\overset{+}{\rightarrow}) \sum F_{h,earth} = &+ \{F_{ff,h} + F_{fm,h} + F_{rm,h} + F_{rr,h} - F_{g,backbone} \cdot sin(\theta)\} \cdot cos(\theta) \\
&- \{F_{ff,v} + F_{fm,v} + F_{rm,v} + F_{rr,v} - F_{g,backbone} \cdot (1 - cos(\theta))\} \cdot sin(\theta) \\
&+ R_{t,m}
\end{aligned}
\tag{C-1}
$$

The first two lines in (C-1) represent the decomposed forces measured at the 8 force transducers. The term consisting of $F_{g,backbone}$ is a correction for the backbone construction's zeroed gravitational force. Pitch causes engagement with the horizontal transducers and a slight overestimation of the vertical transducers values. The third row of the equation represents the earthbound towing force.

Equivalently for the earthbound vertical sum of forces the sum of forces yields:

$$
\begin{aligned}
(+\uparrow) \sum F_{v,earth} = &+ \{F_{ff,h} + F_{fm,h} + F_{rm,h} + F_{rr,h}\} \cdot sin(\theta) \\
&+ \{F_{ff,v} + F_{fm,v} + F_{rm,v} + F_{rr,v} - F_{g,backbone} \cdot (1 - cos(\theta))\} \cdot cos(\theta)
\end{aligned}
\tag{C-2}
$$

Vertical shear force

The boundary conditions for a free-free beam state that the VSF at the tips of the beam should be zero at all times. In the numerical calculation, the VSF is calculated over the length of the beam by using the Heaviside step function. In continuous form this function is defined as:

$$
H(x) = \begin{cases} 0, & x < 0, \\ 1, & x \geq 0 \end{cases}
\tag{C-3}
$$

The equation for the shear force distribution is outlined below:

$$\begin{aligned} VSF(x) &= F_{rr,v} \cdot H(x - x_{rr}) + F_{rm,v} \cdot H(x - x_{rm}) \\ &+ F_{fm,v} \cdot H(x - x_{fm}) + F_{ff,v} \cdot H(x - x_{ff}) \end{aligned} \tag{C-4}$$

(C-5)

Vertical bending moment

For a (theoretical) beam, the vertical bending moment can be constructed directly from differentiation of the VSF function line. In the current case of the ship model, acting horizontal forces contribute to the VBM as well. In the diagram this results in an jump in the bending moment line, located at the longitudinal positions of the horizontal force transducers.

The moment curve is constructed by force integration from the rear to midship and from the front to midship. Omitting potential measurement inaccuracies, no discontinuity should be present. I.e. equally valued and equally derivatives at midship. Eq. (C-6) describes these conditions.

$$\begin{aligned} M_{bf}\Big|_{x=0} &= M_{fb}\Big|_{x=0} \\ \frac{dM_{bf}}{dx}\Big|_{x=0} &= \frac{dM_{fb}}{dx}\Big|_{x=0} \end{aligned} \tag{C-6}$$

$(\curvearrowright +)$

$$\begin{aligned} VBM_{rear}(x) &= \{F_{rr,v} \cdot (x - x_{rr}) - F_{rr,h} \cdot y_{Frr,h}\} \cdot H(x - x_{rr}) \\ &+ \{F_{rm,v} \cdot (x - x_{rm}) - F_{rm,h} \cdot y_{Frm,h}\} \cdot H(x - x_{rm}) \end{aligned} \tag{C-7}$$

$(\curvearrowleft +)$

$$\begin{aligned} VBM_{front}(x) = &\{F_{ff,v} \cdot (x_{ff} - x) - F_{ff,h} \cdot y_{Fff,h}\} \cdot (1 - H(x - x_{ff})) \\ &+ \{F_{fm,v} \cdot (x_{fm} - x) - F_{fm,h} \cdot y_{Ffm,h}\} \cdot (1 - H(x - x_{fm})) \\ &+ \{R_{t,m} \cdot cos(\theta) \cdot y_{Rt,m} \cdot (x_{Rt,m} - x)\} \cdot (1 - H(x - x_{Rt,m})) \end{aligned} \tag{C-8}$$

Directly measured vertical bending moment

The VBM measurement via the applied strain gauges can be used directly using the calibration factor [Nm/dV]. This factor is thoroughly determined using a series of static tests.

C-3 Regular waves

In regular waves, the frequencies ship's first order motions are equal to the wave encountering frequencies. Since the hydromechanic forces are the only excitation forces, the internal loads occur at the wave encountering frequencies. In case of impact loads (slamming) a nuance is to be applied. The slamming can cause springing behavior, vibrant motion at frequencies significantly higher than the wave frequency excitation.

First, the (angular) frequency of encounter was calculated for each combination of forward velocity and generated wave. This theoretical value is compared with the value measured by the wave probe.

Filtering and fitting

As expected, wave height, motions and forces show harmonic behavior. The signals ($f_s = 1000Hz$) were processed using a low pass filter, removing frequencies higher than 5 Hz. This value was selected by first checking the maximum frequency of encounter. This was calculated as 4.4 Hz. The low pass filter removes most of the signal's noise.

A sine fit is applied to the signals to provide data such as amplitude and phase.

Accelerometers The accelerometer signals were compared with the derivatives of the motion signal. The sensor data located at the CG was directly compared with the heave signal according to:

$$\frac{d^2Z}{dt^2} = A_{z,CoG} \tag{C-9}$$

The accelerometer sensor data at the bow was compared with the pitch signal according to the equation below:

$$\frac{d^2\theta_{rad}}{dt^2} = \frac{(A_{z,Bow} - A_{z,CoG})}{x_{Az,Bow} - x_{Az,CoG}} \tag{C-10}$$

Besides small discrepancies due to noise, the processed signals correlated well.

The accelerometers signal must be corrected for rotation with $(1 - cos(\theta))$, however with $\theta_{max} = 6.2\,^\circ$, the value that must be subtracted (0.6 % of the initial value) is significantly lower than the measurement accuracy of the sensor. This makes a correction actually superfluous.

C-3-1 Inertia correction

Since the (vertical) force transducers are in fact placed below the structural element, a inertia correction must be applied to obtain the proper forces and VBM at the midship cross section. The uncorrected values generally show an overestimation of the front segment forces and an underestimation of the rear segment forces. The correction can be divided into a correction for vertical acceleration and for rotational acceleration

Vertical acceleration The correction is based on Newton's second law ($F_z = m\ddot{z}$). Where $\ddot{z}$ is the vertical acceleration, and m the mass of the backbone construction in this particular case.

The correction term is built up in the following form:

$$F_{corr,z} = m_{frac} \cdot (m_{beam} \cdot A_{z,CoG}) \tag{C-11}$$

Here m_{fact} is the fraction of beam mass that is 'carried' by that particular vertical force transducer.

Rotational acceleration The correction for rotational acceleration of the backbone is according to an equivalent formula ($M_{yy} = I\ddot{\theta}$) I is in this case the rotational inertia.

$$F_{corr,\theta} = m_{frac} \cdot \frac{I_{beam} \cdot \frac{(A_{z,Bow} - A_{z,CoG})}{x_{Az,Bow} - x_{Az,CoG}}}{x_{trans} - x_{CoG}} \tag{C-12}$$

The rotational acceleration is determined from data of two accelerometers according to Eq. (C-10). The inertial moment is divided by the moment arm from the transducer to the CG to obtain the corresponding inertial force.

The two correction terms are subtracted from the force signal as shown in (C-13). This signal is further processed according to equations (C-7) and (C-8).

$$F_{corr} = F_{initial} - F_{corr,z} - F_{corr,\theta} \tag{C-13}$$

Appendix D

Uncertainty analysis

The measurements' uncertainty intervals were calculated according to ITTC Recommended Procedure 7.5-02-01-01 [44] and de Jong (2011) [43]. The aim of this analysis was to obtain the experiments' 95% confidence values. The experiments can be considered repeatable if the following conditions apply:

1. Identical measurement procedure.
2. Identical measuring instrument under the same environmental conditions.
3. The same location.
4. Repetition over a short period of time (roughly meaning same day).

If one or more conditions are not met, the term reproducibility is used. For the current case, all conditions were met during the repeated measurements.

The analysis focuses on the uncertainty of force and moment measurement. Other parameters being wave height and frequency, ship motions, resistance have uncertainty bounds as well. For the comparison of the two methods, these levels are not directly required. The dimensionless values are generated by dividing the absolute values by such parameters and therefore do eventually require analysis.

D-1 Approach

The measured quantity Y is often defined from other measured quantities $X_1, X_2, ...X_n$. I.e:

$$Y = f(X_1, X_2, X_3, ...X_N) \tag{D-1}$$

This function includes all quantities that can contribute to the uncertainty of the measurand Y. This includes corrections and instrument calibrations. The combined uncertainty can be computed via the law of propagation, which will be described later.

The total uncertainty interval $\pm U_i$ about the variable X_i is defined as the band around X_i with a 95 % confidence level within which the true value lies. This interval is determined by a summation of the bias error B_i and the precision error P_i. Briefly formulated:

$$U_i = \sqrt{B_i^2 + P_i^2} \tag{D-2}$$

D-2 Bias error

Bias errors are built up from separate contributions as a result of calibration errors, test set-up errors, data acquisition errors etc. The focus here is on the calibration values. Additionally, errors in the used weights and A/D conversion can increase the bias error. Let the bias error B_i exist of M elemental sources, then the total bias is formulated as:

$$B_i = \sqrt{\sum_{j=1}^{M} B_{ij}^2} \tag{D-3}$$

The amount of elemental sources is different for the direct and indirect methods obviously. The following two subsections outline the two approaches.

D-2-1 Indirectly measured VBM

Regarding the indirectly measured VBM, the quantity is a a function of the forces and the distances.

$$\begin{aligned} VBM_{indirect} = f(&F_{ffv},\ F_{ffh},\ F_{fmv},\ F_{fmh},\ F_{rmv},\ F_{rmh},\ F_{rrv},\ F_{rrh},\ F_{Rtm} \\ &x_{ffv},\ z_{ffh},\ x_{fmv},\ z_{fmh},\ x_{rmv},\ z_{rmh},\ x_{rrv},\ z_{rrh}) \end{aligned} \tag{D-4}$$

The uncertainty of distances is a type B uncertainty, meaning that the uncertainty component is obtained by other means than statistical analysis of a series of observations. The uncertainty is set at $\pm 1mm$.

The uncertainty in measured force was determined from the calibration process, i.e. a Type A uncertainty. The force calibration was carried out with masses hung to the force transducers. The force is related to mass by the following equation:

$$F = mg(1 - \rho_a/\rho_w) \tag{D-5}$$

This definition is stated in the ASTM E74-02 guideline. Here, m is the mass, g the local acceleration of gravity, ρ_a the air density and ρ_w the density of the weight. The last term, representing the buoyancy correction is typically 0.017%. Since no data regarding the densities was recorded, an uncertainty of the used mass quantity is neglected. The bias uncertainty was determined from a linear regression of the calibration values.

The error between the value of the linear regression and the obtained value during calibration that can be used is named the Standard Error Estimate (SEE) and given by Coleman And Steele (2009) [45] as:

$$SEE = \sqrt{\frac{\sum_{i=1}^{N}(Y_i - (aX_i + b))^2}{N - 2}} \tag{D-6}$$

N is the number of calibration measurements, Y_i the actual value at point i with value X_i and a and b the coefficients of the fitted linear curve. ± 2 SEE holds approximately 95% of the data points and is used in this calculation.

Table D-1: Indirectly measured VBM calibration parameters.

Name	no. of samples	Mean [Nm/V]	SEE [Nm/V]	SEE/Mean [-]	t95 bounds [Nm/V]
F_{ffv}	16	8.78	1.22 E-3	1.39 E-4	8.786 - 8.788
F_{ffh}	16	4.13	2.85 E-2	6.91 E-3	4.103 - 4.160
F_{fmv}	16	8.64	5.24 E-3	7.45 E-4	8.637 - 8.648
F_{fmh}	16	4.18	3.11 E-3	6.06 E-4	4.176 - 4.182
F_{rmv}	16	8.61	8.78 E-3	1.01 E-3	8.609 - 8.627
F_{rmh}	16	4.09	1.14 E-3	2.79 E-4	4.091 - 4.093
F_{rrv}	16	9.39	1.19 E-2	1.27 E-3	9.383 - 9.406
F_{rrh}	16	4.25	2.38 E-3	5.59 E-4	4.245 - 4.250
F_{Rtm}	16	9.44	1.42 E-2	1.50 E-3	9.429 - 9.458

Error propagation

Error propagation results from aggregation of measured variables. From Eqs. (D-4) and (C-7), (C-8) the total bias limit can be determined. The aggregated (or reduced) limits are defined as:

$$B_A = \sqrt{\sum_{i=1}^{M}(\vartheta_i B_i)^2} \tag{D-7}$$

Here ϑ_i is the partial derivative of the aggregated variable A with respect to the elemental variable X_i. It is assumed that the bias errors of the elemental sources are not interdependent, if this would be the case, cross-terms need to be included.

Regarding the VSF, the elemental variables are the vertical forces (5) whereas for the VBM calculation the elemental variables are all acting forces and the positions on which the forces act for the front to back case (10) and the back to front case (8). Summation of variables as stated in Eq. (D-7) results in a summation of the error bounds.

D-2-2 Directly measured VBM

The moment calibration was carried out directly on the backbone after the strain gauges were placed. Half of the backbone was rigidly connected to a steel table, while weights are hung to

the free hanging part. The weights acted at several positions and in two opposite directions due to turning of the backbone. The theoretical moment was divided by the change in voltage to obtain the calibration factor. This factor was directly used to determine the acting bending moment.

$$VBM_{direct} = f(VBM) \tag{D-8}$$

The calibration factor and accompanying parameters are listed in Table D-2.

Table D-2: Directly measured VBM calibration parameters.

Name	no. of samples	Mean [Nm/V]	SEE [Nm/V]	SEE/Mean [-]	t95 bounds [Nm/V]
VBM	55	16.53	1.35 E0	8.17 E-2	15.18 - 17.88

From the mean and confidence bounds, 95 percent certainty bounds due to calibration bias errors are $VBM \pm 8.2\%$.

D-2-3 Other

Plotting data at dimensionless axes introduces extra uncertainty components from the variables that make up the dimensionless variable. Where practical, the uncertainty limits were derived from statistical data. In other cases the limits as used in de Jong (2011) were used.

Table D-3: Bias limits

Quantity	Symbol	Unit	Bias limit
Gravitational acceleration	g	m/s^2	0.025
Model length	L_{pp}	m	0.002
Model forward speed	V_m	m/s	0.006
Wave elevation	ζ_a	mm	3.570
Wave frequency	ω	rad/s	0.015

Uncertainty of the dimensionless velocity, expressed by the Froude number is not included. Any uncertainty in this variable would yield horizontal error bars for plots having the Froude number plotted at the horizontal axis. This is valid for the dimensionless frequency as well. The dimensionless bending moment values are generated by dividing the bending moment by the gravitational acceleration, model length and width, wave elevation and water density.

D-3 Precision error

The precision error is determined using the end-to-end approach. The standard deviation of N readings is defined as

$$S_i = \sqrt{\sum_{k=1}^{N_i} \frac{((X_i) - \overline{X}_i)^2}{N_i - 1}} \tag{D-9}$$

For the calm water runs, 3 pairs of equal measurement conditions were analyzed to estimate the precision limits. The precision limit as fraction of the measured value was computed using

$$P_{i,j} = K \cdot S_{i,j} \tag{D-10}$$

With K the coverage factor, being 3.2 in case of sets of two samples, converging to 2 for large sample sizes. The standard uncertainty for the three sets was estimated with

$$P_i = \frac{\overline{P}_{i,j}}{\sqrt{M}} \tag{D-11}$$

Here M is the number of samples over which the mean value is determined. In the case of calm water experiments $M = 3$, in the case of regular head waves experiments $M = 4$.

D-3-1 Indirectly measured VBM

The precision error of the indirectly measured bending moment is dependent on the forces only. From the assumption that the construction is rigidly connected and no plastic deformation is occurring, it can be concluded that no precision error exists for the distances.

Error propagation

Equal to error propagation for the bias error, the precision error is calculated by the square root of the sum of squared element contributions.

$$P_A = \sqrt{\sum_{i=1}^{M} (\vartheta_i P_i)^2} \tag{D-12}$$

Again it is assumed that the errors of the elemental sources are not interdependent, if this would be the case, cross-terms need to be included.

For the Vertical Shear Force (VSF), the elemental variables are the vertical forces (5) whereas for the Vertical Bending Moment (VBM) calculation the elemental variables are all acting forces (5 for F-B and 4 for B-F calculation).

D-3-2 Directly measured VBM

The 95 % certainty bounds for precision errors of the directly measured vertical bending moment are constructed from data of 3 double runs regarding the calm water tests and 4 double runs regarding the regular wave tests. The procedure is equal to the procedure described at the start of the current section.

D-4 Total uncertainty limits

The total uncertainty results from the (aggregated) bias and precision errors. As outlined earlier, this value is calculated according to equation (D-2). This value describes one bound.

Appendix E

Paper Article

Please refer to the following page for the 8 page paper article.

Internal Load Measurement on High Speed Ship Models

Joost de Haan*

Delft University of Technology
The Netherlands
joostdeh@gmail.com

Abstract

A series of experiments was carried out on a partly reproduced measurement set-up of a 1/20 scale two segmented High Speed Craft model. The formerly used set-up proved unreliable during towing tank experiments with the purpose to measure the midship vertical bending moment. After determination of the former set-up flaws, two alternative configurations were applied. The direct method proved more universally usable, especially during the regular wave experiments. At low velocity calm water experiments the indirect method delivers more accurate results.

I. Introduction

Ship model tests have supported in ship design for over a century. Before computers became widely available, model tests were the single option to obtain both quantitative and qualitative results. From the 1970's developments in electronics and likewise numerical simulation ended this monopoly. Nevertheless, today model tank tests still are a viable and essential tool for the design of floating structures. Results can be used to (1) validate theory to apply numerical simulations in the design and (2) for design by testing, directly using the (upscaled) results in the design.

Recently, at the Ship Hydromechanics and Structures (SHS) lab of the TU Delft, a series of experiments was carried out with a 1/20 scale segmented Damen Stan Patrol 4207 high speed craft (Figure 1). The aim of the segmentation was to deliver a set of internal loads, eventually allowing calculation of the model's vertical bending moment at the cut. With this data a new routine of the numerical FASTSHIP can eventually be validated. Unfortunately the experiments outcomes were unsatisfactory due to errors in the measurement set-up. This demanded a review of the set-up and experimental procedures.

*MSc. student Offshore and Dredging Engineering

Literature indicates four main options for internal load measurement at scale model ships:

1. Model with scaled elasticity (hull)
2. Model with scaled elasticity (backbone) connecting multiple rigid segments
3. Model with rigid backbone representation connecting multiple rigid segments
4. Model with force transducer(s) connecting the rigid segments' bulkheads

The scaled elastic backbone is the most widely applied concept at present. In addition to ship motions and the vertical bending moment, a scaled elastic model can deliver a fairly correct representation of the ship's global hydroelastic response. In particular springing response is often critical for large cargo/bulk carriers and FPSO's.

Regarding the prior tested Stan Patrol model, option 3 applies. An example of application of the rigid backbone representation is conducted by Rousset (2010). The prove of concept is outlined in his research, although no forward speed was included.

Figure 1: *Damen Stan Patrol 4207 render.*

For a high speed craft model, encounter frequencies in the range of $1.5 - 8.5\ Hz$ can be expected. To consider the used backbone rigid, the frequency of its first mode must be an order of 6-8 times higher than the excitation frequency, say 70 Hz. From analytic calculations the expected natural frequencies of the bare beam were found sufficiently high. The bare beam's first natural frequency is above 700 Hz, when connected to the segments the decrease is limited to finally yield natural frequencies above 200 Hz.

Capturing the beam's modes and response from transient loads is not part of the current scope of research, leaving the rigid beam representation the concept of choice. The process of set-up design and problem identification at the formerly used set-up is outlined in the subsequent section.

II. Methods

I. Experimental problem identification

A broad range of experiments was conducted to gain a deeper understanding of the load path at the prior used set-up. Additionally, the force transducers that were used are examined for sensitivity to cross talk. The maximum values of the applied loads were higher than the loads during towing tank experiments to increase the visibility of errors in the configuration.

In the test setup, the backbone was partly fixed to a steel table, displayed by the left part of Figure 2. The free hanging part is a replication of one segment connected to the beam via force transducers.

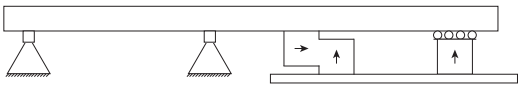

Figure 2: *Replicated prior set-up – side view.*

Three transducers can be distinguished in the figure. The vertical arrows indicate a transducer fitted to measure vertical forces, a horizontal arrow indicates a transducer to measure the horizontal loads. The right vertical transducer is connected via a sliding element, drawn by a roller support. On the lower ends of the vertical transducers a hardwood shelf was connected. At this shelf dead-weight was placed at specified places to mimic vertical load at the segment.

When applying load exactly in between (or at equal distances of) the connections, the results yielded a non equal division of the applied load. A slightly altered set-up (Figure 3) shows that by adding hinges, vertically directed forces can be measured accurately. Any potential bending moment at the connection point was uncoupled by the hinges. As a result, the bending moment at the beam can be determined from the forces and moment arms.

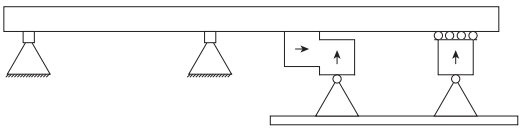

Figure 3: *Prior set-up (added hinges) – side view.*

Potential cross-talk of a bending moment or 'parallel' oriented force at the force transducers was investigated hereafter. Experiments showed that the transducers are insensitive to parallel loads, in contrast to an applied bending moment. Fortunately this component is marginal and by adding the hinges, the bending moment present is expected to be small.

During towing tank experiments a significant horizontal component is present. In the prior experiments, mainly the horizontal transducers yielded unreliable results. Tests with static horizontal and combined load were con-

ducted to gain a better understanding of the set-up. The horizontal force was created by a cable, tensioned by deadweight, running over a pulley. Potential friction at the pulley was investigated and found negligible. A series of tests with varying vertical and horizontal loads yielded results of 35 conditions. In practically all conditions, a amount of horizontal force is unregistered by the transducer. This indicated the presence of friction at the roller support. The amount of friction showed a dependency of the vertical force transferred through the support and a moment created by the horizontal load, acting on the roller support.

II. Requirements

For successful validation of full scale ships, a various prime requirements of the design are essential. In addition to applying correct geometric and dynamic scaling, the main structural scaling factor is similarity of the mass distribution. In practice scaled mass distribution is unfeasible. Instead correct scaling of the location of the center of gravity and moment(s) of inertia is conducted. As mentioned in the introduction, natural frequencies of the system must be above 70 Hz to minimize high frequent response. The cut at midship must be properly sealed to prevent water invading the model. With the full set of requirements as preconditions, the set-up concept was developed.

III. Set-up configuration

Two force measurement options were fitted to the segmented model. At 9 positions the force was measured. In addition, the vertical bending moment was measured directly at the rigid backbone.

The backbone was connected via 4 force transducers to each segment. The rigid connection formally yields a statically undetermined system, however for two reasons this is not regarded as a problem. First, since the backbone and segments are rigid, deformation is expected to play a marginal role. Small deformations can cause measurement inaccuracies at the two horizontal transducers. Fortunately one can level this factor out when looking at the connected system.

Applying strain gauges directly on the backbone is a method that is widely used at flexible backbone concepts. Since *rigid* is only a theoretical notion, deformation of the rigid backbone is possibly useful to measure the vertical bending moment directly at the backbone. After analytically determining the strain at midship under perpendicular load, it was decided to place strain gauges on the outer fibers of the backbone. The strain under load is at the bottom of the range of the strain gauges. However, placing and calibration is not considered much work and allows to directly compare the direct and indirect methods.

IV. Data acquisition

In total 9 forces and 1 moment is measured at a sampling rate of 1000 Hz. The ship's motions are measured using a set of stationary cameras, able to capture all 6 DOF at 100 Hz. The set-up and head waves only allow movement in the x-z plane. The vertical acceleration is captured via two accelerometers at a frequency of 1000 Hz. One sensor was located at the CoG and one at the bow. From the two signals the heave and pitch accelerations can be determined. The wave height was measured at the LCG by a wave rake. Finally, three accelerometers were placed on the backbone to capture any vibrations if present. In total 30 signals were stored for each run.

V. Test program

The test program was determined after identifying boundary conditions originating from the towing carriage, wave maker and the full scale and numerical code parameters. To investigate the influence of resistance (internally: the horizontal force component) the hull roughness was increased after finishing the first series of experiments. As a result the calm water tests are carried out for both hull conditions. The test program can be classified into:

1. Dry testing
2. Calm water at constant velocity

3. Regular head waves at constant velocity
4. Irregular head waves at constant velocity

It can be seen that the level of disturbance increases with the progressing test program. Please note that for the purpose of this research, irregular wave experiments have not been post-processed.

Table 1: *Rounded calm water velocities.*

V_m	$[m/s]$	0.5	1.5	2.5	3.5	4.5	5.0	5.5
Fn_∇	$[-]$	0.3	0.9	1.5	2.0	2.6	2.9	3.2
Fn_L	$[-]$	0.1	0.3	0.6	0.8	1.0	1.1	1.2

The towing velocities for the calm water experiments are outlined in Table 1. In regular head waves the model was constrained, 'moored' and towed at 3.0 and 4.5 m/s. At 3.0 m/s, the model was towed through head waves with steepness 1/30 and 1/60. Table 2 shows the key wave parameters.

Table 2: *Regular head waves parameters.*

ω_s $[rad/s]$	ω_m $[rad/s]$	$\omega(L/g)^{1/2}$ $[-]$	λ/L $[-]$	$\zeta_a(\kappa = 60^{-1})$ $[m \cdot 10^{-2}]$
0.80	3.58	1.61	2.43	8.0
0.90	4.02	1.81	1.93	6.3
1.00	4.47	2.01	1.56	5.1
1.10	4.92	2.21	1.29	4.2
1.20	5.37	2.41	1.08	3.6
1.30	5.81	2.61	0.92	3.0
1.40	6.26	2.81	0.79	2.6
1.50	6.71	3.01	0.69	2.3

III. Results

I. Dry testing

First, the force transducers were calibrated individually for force in two directions. The backbone was calibrated by applying a series of loads at the points of connection with the segments. The theoretical moment was used to determine the calibration factor $[dNm/dV]$.

The first validation part consists of a reproduction of the earlier mentioned set-up (Figure 3). The load cases with vertical load, horizontal load and combined load yielded promising results. The portion of leaking forces was reduced to maximally $\pm 1\%$ of the applied force.

The second part of dry testing considered validation of the assembled set-up. Although described in the dry testing section, the experiments were held in still water for pragmatic reasons. A set of two 2 kg weights was shifted inside the two segments. The change in mass distribution results in a change of bending moment and was measured at midship. The change in bending moment is compared for the directly and indirectly measured values. All indirectly measured bending moment values were approx. 3 % higher than the directly measured values. The discrepancy was sufficiently small to consider the assembly of the two halves successful.

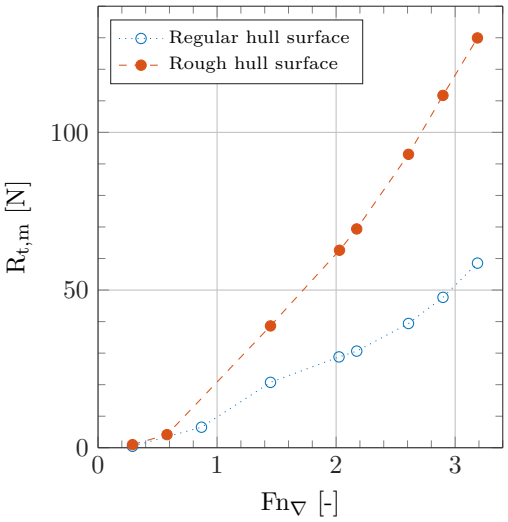

Figure 4: *Model total resistance.*

II. Calm water

The carried out calm water experiments can be considered quasi-static. A check was performed regarding the sum of (earthbound) horizontal and vertical forces. The sum of horizontal forces is close to zero for all measurements, with the median $dF = 0.6\ N$. The sum of vertical forces was non-zero for all measurements. Isolated measurements show that friction is present at the guidance pole that connects the model to the carriage. With this friction term added (as-

sumed linear), the median $dF = 0.1\ N$ for the regular hull and $dF = 1.3\ N$ for the rough hull. The resistance was approximately doubled at the increased hull roughness experiments for all towing velocities. The total resistances are presented by the blue open and red solid dots in Figure 4.

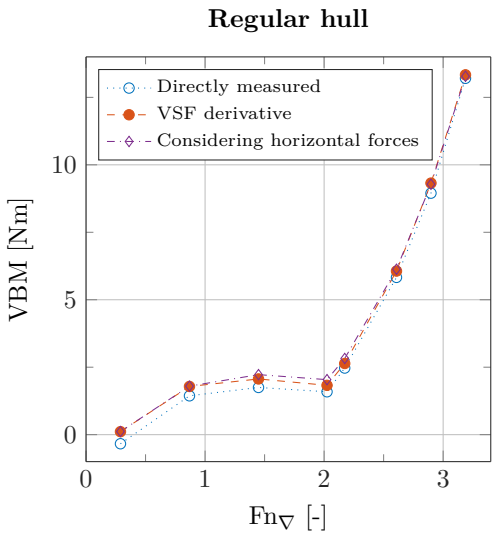

Figure 5: *Model VBM, regular hull.*

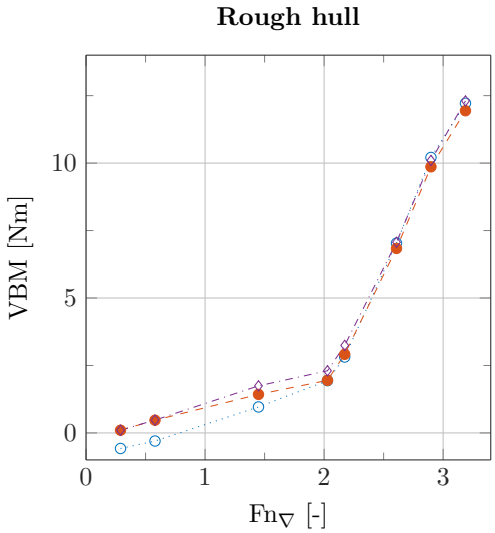

Figure 6: *Model VBM, rough hull.*

The vertical bending moment (VBM) was determined using three methods:

1. Directly, at the backbone
2. Indirect, using 9 force transducers
3. Indirect, using 4 force transducers

The increase in resistance does not reflect in the vertical bending moment. The three methods are plotted in Figures 5 and 6. The displayed values must be interpreted as added VBM. The ship model's still water bending moment ($\approx 12\ Nm$) is not included in the plots.

III. Regular head waves

The constrained model delivered data of the the wave forces at a range of wave frequencies. The moored model was free in heave and pitch only. A correction to the measured forces was required to obtain the actual bending moment at the backbone. The force transducers are located in between the masses of the segment and backbone configuration. From accelerometer data the heave and pitch accelerations were derived. Using these accelerations and the inertial properties of the beam construction the correction terms are constructed. Figure 7 shows the result of this method. The clearly visible high frequent component is further interpreted in the discussion chapter.

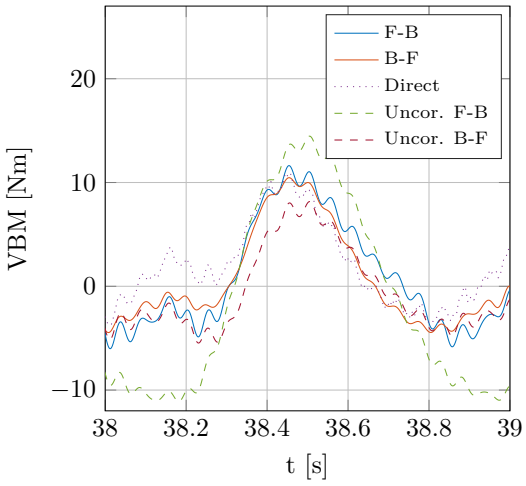

Figure 7: *VBM timetrace, $\omega_m = 3.58$ rad/s.*

The 95% confidence limits were determined

according to ITTC (2014) and de Jong (2011). The amplitudes and dimensionless amplitudes of the model towed at 3.0 m/s and encountering waves having a constant 1/30 steepness are plotted in Figure 8.

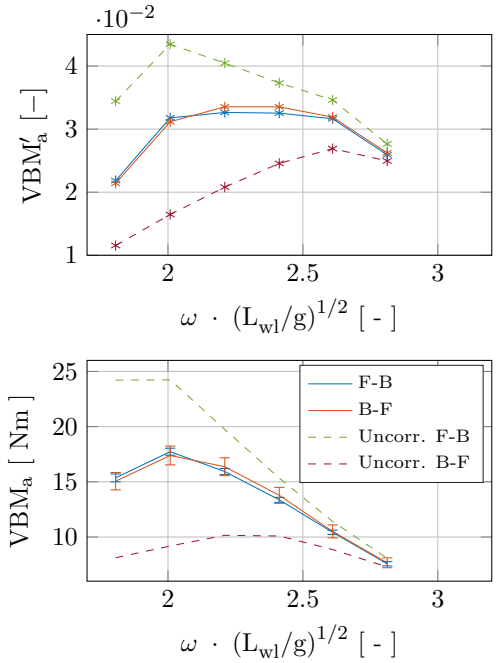

Figure 8: *VBM amplitudes, $V_m = 3.0$ m/s.*

IV. Discussion

I. Concept

The ship model was outfitted to deliver two options to determine the midship VBM. Both options contained insecurities regarding their practical use. Direct measurement of the bending moment is proven for (scaled) flexible backbones in numerous experimental studies, in contrast to direct measurement via strain gauges at a stiff material like carbon fiber. Moreover placing strain gauges on a anisotropic tube may question the feasibility of measuring the acting VBM. After calculating the (order of magnitude) of the backbone strain under bending force, the strain gauge configuration was thoroughly calibrated. Calibration showed a linear elastic behavior of the beam. In contrast to the 'temple' force transducers that altogether make up the indirect measurement method, the calibration showed a small amount of hysteresis in the low load regions.

The indirect measurement method is built up using the force transducers as rigid connection between the backbone and segments. In for example the theory of statics and in practice at bridges, this connection type is considered statically undetermined and therefore unwanted. Extraordinary high forces can occur when a typical construction deforms under load. Regarding the model, this can negatively influence the measurement accuracy and ultimately break the sensors and segment connections.

II. Calm water experiments

Two series of calm water experiments were conducted to verify the set-up at quasi static behavior and compare the end values of the regular hull and a hull generating increased towing resistance. The end-values of the processed indirect data correspond well with the direct values. Due to the high stiffness of the backbone, the uncertainty bounds of the indirect method showed favorable over the direct method.

The experiments show that the resistance component is marginally influencing the midship vertical bending moment, with alternating higher and lower valued outcomes. A third option, calculating the bending moment from merely the vertical shear forces delivers satisfying results when the average of front and rear segment values is taken. This outcome argues for the possibility to measure the VBM by using four force transducers measuring the vertical (i.e. perpendicular to the beam's longitudinal axis) loads.

III. Regular head waves experiments

Measurement data of the carried out regular wave experiments required more intensive processing, in particular regarding the indirectly measured bending moment. Since the forces are measured in between the moving masses of the segments and backbone, an inertia correction must be applied. The direct measurement

method is more direct regarding data processing as well. The correction method cannot be seen as versatile or universal. The terms and their parts must be constructed for each experimental set-up and ideally, the corrections are verified from controlled oscillation experiments.

Applying the correction at the four[1] cases could not deliver uniform results. The correction resulted in matching amplitude values regarding the two integration directions at the moored and 3.0 m/s experiments. The measurement signals of the experiments at 4.5 m/s forward speed did not properly correct for inertia forces. The established correction method takes insufficient account of the high level of noise present and the increased non sinusoidal force response.

This makes the direct measurement option favorable in case of dynamic load. On the other hand, the confidence bounds of the indirect method are favorable over the direct method. The chapter's final section further discusses the confidence bound levels. First, the confounding effects at the 4.5 m/s runs are argued.

IV. Confounding effects

The resonance levels at the 3.0 m/s runs were acceptable in the sense that the undisturbed force/moment signals could be extracted from the raw signals successfully. Likewise, the vertical acceleration and (determined) rotational acceleration signals at most runs are harmonic at a frequency equal to the wave encountering frequency.

Apart from this observation, a frequency analysis of the raw signals showed apart from the excitation frequency, a ≈ 18 Hz component is present in the signals. This component is clearly visible in time-trace plots as was illustrated in Figure 7. Distinct experiments showed that an impact load in surge (x) direction results in resonant vibrations at ≈ 18 Hz. Impact in heave direction did not result in any significant resonance. Although conclusive evidence is missing, it is likely that the origin of this resonance frequency can be found at the guidance pole connection. The 18 Hz component was absent at earlier tests in which a significant part of the set-up was assembled.

At higher speed, the effect of this component increases. Especially at the higher wave frequencies (equally: lower wave amplitudes due to the constant steepness) the share of resonance increases up to levels equal to the excitation frequency. The acceleration signals are equally susceptible to this effect, thereby decreasing effectiveness of the correction.

Slamming is another phenomenon that was present at many 4.5 m/s runs. A slam results in a non harmonic vertical acceleration signal. Likewise, the event is reflected in the directly measured bending moment signal and the force transducers. The non harmonic character of the signals make the earlier used sine fits less usable and more prone to errors.

V. Confidence bounds

A number of plots show an error bar at the plotted values. The bar is built up from bias and precision errors. From the calibration of the force transducers and the strain gauges at the backbone a 95% confidence level of the calibration factor was determined. Together with factors as inaccuracies of moment arms, total confidence level was generated for each measurement.

Although aggregated from a large number of inaccuracies, the confidence bounds of the indirect method show a smaller bandwidth than the direct method. This is due to the fact that the level of strain at the backbone is in the lower regions of the measurement band of the strain gauges. This led to a relatively large inaccuracy in the used calibration factor. This inaccuracy reflects in the total inaccuracy by multiplying the relative inaccuracy with the measured value. As a result it is proportional to the measured VBM value.

To minimize this error it is advisable to beforehand choose the force/moment sensor ranges according to the expected force values. Hereafter one can calculate the natural frequencies of individual components and the system and reflect

[1] moored, towed 3.0 m/s at two wave steepnesses and towed at 4.5 m/s

the values to expected excitation frequencies, reconsider the set-up if resonance is expected.

The current confidence bounds show that although the direct method values are close to the indirect values, the accuracy seems insufficient to validate numerical code. By increasing the measurement resolution as briefly described in the enumeration, it is expected that a significant gain in accuracy may be obtained.

V. Conclusions

A thorough series of calm water and regular wave experiments was conducted. The experiments were aimed to validate a designed measurement set-up for internal load measurement on a two segment high speed craft.

From the quasi static calm water experiments the fundamental force equations could be verified. The results showed a global equilibrium in both vertical and horizontal direction. From this finding, the shear force and bending moment was determined from the individual components. The second method, directly measuring the VBM acting on the backbone, required significantly less processing to obtain usable results. The two methods delivered similar results for especially the semi-planing regime velocities. At lower velocities, the direct method VBM results were in most cases marginally lower.

At the quasi static towing experiments in particular, four force transducers are sufficient to determine the midship VBM. When only vertical shear force is measured, the bending moment may be calculated by taking the mean of the front and rear segment values. This method requires the backbone and towing arm positioned practically at the vertical location of the net acting resistance force to minimize the contribution of horizontal load. A second option is to use transducers at one segment only. In case of the used model meaning 4 force transducers for the rear segment or 5 force transducers for the front segment. Two downsides to this method are that the vertical shear force along the backbone cannot be determined properly and that one cannot verify the boundary conditions by comparing the front and rear segment contributions.

The regular wave experiments' sensor data required more thorough processing, especially the indirect method. With inertia correction terms included, the bending moment was fairly similar at most conditions for calculations using front segment forces and rear segment forces. At increasing forward speeds, the amount of resonance increases considerably. At the 3.0 m/s experiments, the filtering and fitting proved effective. In contrast, at 4.5 m/s the results were less satisfactory due to significant noise levels and nonlinearities of the force response. The guidance pole construction seems the cause of the high levels of resonance at high velocities. The use of this construction at high velocities should be reconsidered. More extensive signal processing, taking the impact load into account, may further improve the results.

The current set of confidence bounds are beneficial for the indirect method. The increasing uncertainty for the direct method at increasing bending moments makes sense according to the uncertainty calculation foundation, however physically it is contradictory. A higher bending moment results in higher strain levels. Since the strain levels are on the lower boundary of the measurement range of the strain gauges, higher strain will physically result in more accurate measurements.

References

[Rousset (2010)] Rousset, J., Ferrant, P. and Allesandrini, B. "Experiments on a segmented ship model in directional irregular waves." *Proc. of the 21th IWWWFB*, 2010.

[ITTC (2014)] International Towing Tank Conference "Recommended Procedures and Guidelines. Guide to the Expression of Uncertainty in Experimental Hydrodynamics rev. 02." *ITTC*, 2014.

[de Jong (2011)] de Jong, P. "Seakeeping Behaviour of High Speed Ships: An Experimental and Numerical Study." *Delft University of Technology, Dissertation*, 2011.

Bibliography

[1] E. Smith, *A short history of naval and marine engineering*. The University Press, 1937.

[2] H. Maeda, J. F. Williams, and A. Silverleaf, "Modelling techniques for dynamics of ships [and discussion]," *Philosophical Transactions of the Royal Society of London. Series A: Physical and Engineering Sciences*, vol. 334, no. 1634, pp. 307–317, 1991.

[3] A. Cleine and I. van Deyzen, "Calculation of shear forces and bending moments of a planing monohull sailing in head seas." Unpublished Tech. Rep., 2010.

[4] Y. Wu, R. Chen, and J. Lin, "Experimental technique of hydro-elastic ship model," *Hydro-elasticity in Marine Technology*, 2003.

[5] S. Du, D. A. Hudson, G. W. Price, P. Temarel, R. Chen, and Y. Wu, "Wavelet analysis of loads on a flexible ship model traveling in large-amplitude waves," *Journal of Ship Research*, vol. 52, no. 4, pp. 249–262, 2008.

[6] O. Okland, R. Zhao, and T. Moan, "Numerical assessment of segmented test model approach for measurement of whipping responses," in *Proceedings of the 7th International Conference on Fast Sea Transportation, FAST'2003*, pp. 87–94, 2003.

[7] J. Rousset, P. Ferrant, and B. Alessandrini, "Experiments on a segmented ship model in directional irregular waves," *Proc. of the 21th IWWWFB*, 2010.

[8] N. Fonseca and S. C. Guedes, "Experimental investigation of the nonlinear effects on the vertical motions and loads of a containership in regular waves," *Journal of Ship Research*, vol. 48, no. 2, pp. 118–147, 2004.

[9] N. Fonseca and S. C. Guedes, "Experimental investigation of the nonlinear effects on the statistics of vertical motions and loads of a containership in irregular waves," *Journal of Ship Research*, vol. 48, no. 2, pp. 148–167, 2004.

[10] G. F. Clauss, A. Kauffeldt, and K. Jacobsen, "Longitudinal forces and bending moments of a fpso," in *ASME 2007 26th International Conference on Offshore Mechanics and Arctic Engineering*, pp. 89–98, American Society of Mechanical Engineers, 2007.

[11] S. P. Kim, H.-C. Yu, S. Y. Hong, *et al.*, "Segmented model testing and numerical analysis of wave-induced extreme and springing loads on large container carriers," in *Proceedings of the 20th international offshore and polar engineering conference, Beijing, China*, pp. 385–392, 2010.

[12] J. Gerritsma, R. E. Taylor, M. Greenhow, D. Robinson, and H. Maeda, "Forced oscillation experiments [and discussion]," *Philosophical Transactions of the Royal Society of London. Series A: Physical and Engineering Sciences*, vol. 334, no. 1634, pp. 199–211, 1991.

[13] E. Dudson, H. J. Rambech, and M. Wu, "Determination of wave bending loads on a 40 knot, long slender open topped containership through model tests and hydrodynamic calculations with particular reference to the effects of hull flexibility on fatigue life," in *6th International Conference on Fast Sea Transportation*, 2001.

[14] T. E. Schellin, C. Beiersdorf, X.-B. Chen, N. Fonseca, C. Guedes Soares, A. Maron Loureiro, A. D. Papanikolaou, A. Perez de Lucas, and J. M. Ponce Gomez, "Numerical and experimental investigation to evaluate wave-induced global design loads for fast ships," *Transactions-Society of Naval Architects and Marine Engineers*, vol. 111, pp. 437–461, 2003.

[15] D. Dessi, R. Mariani, F. La Gala, and L. Benedetti, "Experimental analysis of the wave induced response of a fast monohull via a segmented hull model," in *Proc. 7th Int. Conf. on Fast Sea Transportation (FAST), Ischia, Italy, 7–10 October 2003*, 2003.

[16] D. Dessi and R. Mariani, "Structure and load identification using wave excitation in sea-keeping tests," *20th IWWWFB, Spitsbergen, Norway*, 2005.

[17] D. Dessi and R. Mariani, "Analysis and prediction of slamming-induced loads of a high-speed monohull in regular waves," *Journal of Ship Research*, vol. 52, no. 1, pp. 71–86, 2008.

[18] D. Dessi and E. Ciappi, "Slamming clustering on fast ships: From impact dynamics to global response analysis," *Ocean Engineering*, vol. 62, pp. 110–122, 2013.

[19] A. Marón, J. Ponce, N. Fonseca, and C. G. Soares, "Experimental investigation of a fast monohull in forced harmonic motions," *Applied Ocean Research*, vol. 26, no. 6, pp. 241–255, 2004.

[20] N. Fonseca and C. Guedes Soares, "Validation of a time-domain strip method to calculate the motions and loads on a fast monohull," *Applied Ocean Research*, vol. 26, no. 6, pp. 256–273, 2004.

[21] G. F. Clauss, C. E. Schmittner, J. Hennig, C. G. Soares, N. Fonseca, and R. Pascoal, "Bending moments of an fpso in rogue waves," in *ASME 2004 23rd International Conference on Offshore Mechanics and Arctic Engineering*, pp. 455–462, American Society of Mechanical Engineers, 2004.

[22] C. G. Soares, N. Fonseca, R. Pascoal, G. F. Clauss, C. E. Schmittner, and J. Hennig, "Analysis of design wave loads on an fpso accounting for abnormal waves," *Journal of Offshore Mechanics and Arctic Engineering*, vol. 128, no. 3, pp. 241–247, 2006.

[23] G. F. Clauss, A. Kauffeldt, and M. Klein, "Systematic investigation of loads and motions of a bulk carrier in extreme seas," in *ASME 2009 28th International Conference on Ocean, Offshore and Arctic Engineering*, pp. 277–287, American Society of Mechanical Engineers, 2009.

[24] G. Clauss, M. Klein, and A. Kauffeldt, "Limiting loads and motions of ships in extreme sea states," in *IMAM 2009âĂŤ13th Congress of International Maritime Association of Mediterranean, Istanbul, Turkey*, 2009.

[25] M. Wu and T. Moan, "Efficient calculation of wave-induced ship responses considering structural dynamic effects," *Applied Ocean Research*, vol. 27, no. 2, pp. 81–96, 2005.

[26] E. Begovic, A. Day, and A. Incecik, "Experimental ship motion and load measurements in head and beam seas," in *9th Symposium in High Speed Marine Vehicles, Naples, Italy.*, 2011.

[27] S. Zhu, M. Wu, and T. Moan, "Experimental and numerical study of wave-induced load effects of open ships in oblique seas," *Journal of Ship Research*, vol. 55, no. 2, pp. 100–123, 2011.

[28] S. Zhu, M. Wu, and T. Moan, "Experimental investigation of hull girder vibrations of a flexible backbone model in bending and torsion," *Applied Ocean Research*, vol. 33, no. 4, pp. 252–274, 2011.

[29] J. A. Keuning, *Nonlinear behaviour of fast monohulls in head waves*. TU Delft, Delft University of Technology, 1994.

[30] R. Wereldsma, "Normal mode approach for ship strength experiments, a proposal," in *Proceedings of the International Symposium on the Dynamics of Marine Vehicles and Structures in Waves, London*, 1974.

[31] I. T. T. Conference, "Ittc – recommended procedures and guidelines. global loads seakeeping procedure.," tech. rep., ITTC, 2011.

[32] L. Holthuijsen, *Waves in Oceanic and Coastal Waters*. Cambridge University Press, 2007.

[33] R. Dallinga and I. Drummen, "Presentation: Wave loads - marine structural failures." MARIN, 2011.

[34] J. A. Keuning and J. Pinkster, "Optimisation of the seakeeping behaviour of a fast monohull," in *FAST Conference Proceedings*, 1995.

[35] H. Sun, "A boundary element method applied to strongly nonlinear wave-body interaction problems," *Fakultet for ingeniørvitenskap og teknologi*, 2007.

[36] Y. Yamamoto, K. Iida, T. Fukasawa, T. Murakami, M. Arai, and A. Ando, "Structural damage analysis of a fast ship due to bow flare slamming," *International shipbuilding progress*, vol. 32, no. 369, pp. 124–136, 1985.

[37] O. F. Rognebakke and O. M. Faltinsen, "Effect of sloshing on ship motions," *16th I-WWWFB, Hiroshima*, 2001.

[38] X. Gu and T. Moan, "Long-term fatigue damage of ship structures under nonlinear wave loads," *Marine Technology*, vol. 39, no. 2, pp. 95–104, 2002.

[39] S. Hirdaris, W. Bai, D. Dessi, A. Ergin, X. Gu, O. Hermundstad, R. Huijsmans, K. Iijima, U. Nielsen, J. Parunov, *et al.*, "Loads for use in the design of ships and offshore structures," *Ocean engineering*, vol. 78, pp. 131–174, 2014.

[40] T. Von Kármán, *The impact on seaplane floats during landing*. National Advisory Committee for Aeronautics, 1929.

[41] E. E. Zarnick, "A nonlinear mathematical model of motions of a planing boat in regular waves," tech. rep., DTIC Document, 1978.

[42] J. M. Journée and W. W. Massie, "Offshore hydromechanics," *Delft University of Technology*, vol. 4, p. 38, 2001.

[43] P. De Jong, "Seakeeping behaviour of high speed ships: An experimental and numerical study," *TU Delft*, 2011.

[44] I. T. T. Conference, "Ittc – recommended procedures and guidelines. guide to the expression of uncertainty in experimental hydrodynamics rev. 02.," tech. rep., ITTC, 2014.

[45] H. W. Coleman and W. G. Steele, *Experimentation, validation, and uncertainty analysis for engineers*. John Wiley & Sons, 2009.

Glossary

List of Acronyms

3mE	Mechanical, Maritime and Materials Engineering
CFD	Computational Fluid Dynamics
CG	Center of Gravity
CB	Center of Buoyancy
DOF	Degrees of Freedom
ESC	Enlarged Ship Concept
HBM	Horizontal Bending Moment
HSC	High Speed Craft
HSF	Horizontal Shear Force
ITTC	International Towing Tank Conference
LCG	Longitudinal Center of Gravity
MARIN	Maritime Research Institute Netherlands
RANS	Reynolds-Averaged-Navier-Stokes
RAO	Response Amplitude Operator
SG	Strain Gauge
SHS	Ship Hydromechanics and Structures
SEE	Standard Error Estimate
SWBM	Still Water Bending Moment
TEU	Twenty feet Equivalent Unit

TM	Torsional Moment
TU Delft	Delft University of Technology
VCG	Vertical Center of Gravity
VBM	Vertical Bending Moment
VSF	Vertical Shear Force

List of Symbols

α	Angle of encounter
$\delta(x)$	Dirac delta function
ϵ	Strain (mechanics)
κ	Curvature
λ	Wave length
Λ_L	Geometric scaling factor
Λ_ρ	Density scaling factor
μ	Dynamic viscosity
μ	Mass per unit length
∇	Displacement
ω	(Wave) frequency
ω_e	Wave encounter frequency
ρ	Density
σ	Stress (mechanics)
θ	(Pitch) angle
υ	Kinematic viscosity
a	Amplitude
d	Depth
E	Young's or elastic modulus
EI	Bending stifness
g	Gravitational acceleration (9.81 m/s^2)
I	Second moment of area
k	Wave number
k_0	Deep water wave number
L	(Characteristic) length
L_{pp}	Length between perpendiculars
q	Distributed load
r	Radius
t	Time
U	Characteristic velocity

V	Velocity
w	Defection in z direction
F	Force
Re	Reynolds number
$_g$	Gravitational
$_i$	Inertial
$_m$	Model size ship
$_{pp}$	Between perpendiculars
$_s$	Full size ship

Acknowledgements

First of all I would like to thank my supervisors Pepijn de Jong and René Huijsmans for their guidance during the writing of this thesis. Also at moments when I thought I was exactly on track, they managed to point me in a more relevant and improved direction. Prof. Huijsmans' support at the start of my graduation project is highly appreciated. I thank Pepijn for the pleasantly open attitude towards me, always willing to take a moment with me to discuss the many topics. I would like to thank all committee members for their time and effort during reading, listening and providing feedback.

I would like to thank Lex Keuning for sharing his knowledge and experience of experimental research and for reviewing my thesis. I am grateful that my sailing-vocabulary has significantly increased. I want to thank Albert Rijkens for his support, especially regarding the sometimes puzzling Latex related issues.

Many thanks to the support staff of the Ship Hydromechanics laboratory, Peter Poot, Jasper den Ouden, Wick Hillege, Hans van der Hek and Frits Sterk for their support with the model preparation and -tests. Thanks to Piet de Heer with helping me collect literature that was otherwise rather difficult to obtain. I would like to thank all staff members and students for the interesting and pleasant coffee breaks. I would like to take this opportunity to thank Damen Shipyards for the financial support during the graduation period and providing me a fine impression of the Gorinchem office and shipyard.

I wish to thank my parents Wim and Marike for their continuous and unconditional believe in me throughout the graduation and in all the years before. Their support was and is truly invaluable.

Delft, University of Technology — J.R. de Haan
March 18, 2015